

Application of Supercontinuum to Spectroscopy

Diplomarbeit



seit 1558

FRIEDRICH-SCHILLER-UNIVERSITÄT JENA
PHYSIKALISCH-ASTRONOMISCHE FAKULTÄT

eingereicht von Damian Nikolaus Schimpf
geboren am 6. März 1980 in Halle (Saale)

Betreuer: Dr. rer. nat. J. Limpert

1. Gutachter: Prof. Dr. rer. nat. habil. A. Tünnermann

2. Gutachter: Prof. Dr. rer. nat. habil. H. Bartelt

Bearbeitungszeitraum: November 2004 - September 2005

Tag der Verleihung des Diploms:.....

Acknowledgements

I gratefully acknowledge the help of many people during the course of this project. I would like to thank Prof. Andreas Tünnermann for choosing the interesting topic of this thesis, for giving me the chance to work on this project, for supervising the work and for supporting the stay at Imperial College London during the diploma. Equally, I thank Prof. Paul French for his hospitality, supervision and invitation to join Brad Amos' workshop in Plymouth.

I thank to all past and present members of Prof. Paul French's photonics group. In particular, the presented application of supercontinuum to fluorescence lifetime imaging would not have been possible without Dr. Daniel Elson and Dr. Jose Requejo-Isidro. I would like to say a special thanks to Dr. Christopher Dunsby, for his efforts on my behalf. I would also like to thank Dr. Neil for his advice.

Thank you to all the members of the group - Peter Lanigan, James McGinty, Bosanta Boruah, Vincent Poher, Egidijus Auksorius, Pieter De Beule, Richard Benninger, Clifford Talbot, Ian Munro, Sunil Kumar, and Bebhinn Treanor. Further thanks must go to Dylan Owen and David Grant for the 'confocal session' and the samples.

Equally, I thank all members of the Fiber & Waveguide Lasers group at the Institute of Applied Physics at Friedrich Schiller University Jena: Dr. Andreas Liem, Dr. Mathias Reich, Max Stumpf, Thomas Schreiber, Heike Schultz, Fabian Röser, Oliver Schmidt, Steffen Hädrich, Thomas Andersen and Dr. Bülend Ortaç.

I would like to say a special thanks to Dr. Jens Limpert, for his assistance, both in setting up experiments in the lab, and answering the questions I had throughout the project.

The primary support for this work was provided by the Friedrich Ebert Foundation. I am grateful for the studentship without which the stay at Imperial College London would not have been possible.

Contents

1	Introduction	1
2	Basics of Continuum Generation	3
2.1	Dispersion	3
2.2	Nonlinearity	4
2.3	Supercontinuum Generation via Microstructured Fibre	5
2.3.1	Microstructured Fibre	5
2.3.2	Higher-order Soliton Fission Mechanism	6
2.3.3	Modelling	9
3	Fluorescence Lifetime Imaging	11
3.1	Fluorescence	12
3.1.1	Phenomenon of Fluorescence	12
3.1.2	Fluorescence Lifetime	13
3.2	Imaging	13
3.2.1	Overview	13
3.2.2	Conventional Wide-Field Fluorescence Microscopy	14
3.2.3	Confocal Microscopy	15
3.2.4	Wide-Field Optically-Sectioned Imaging using a Nipkow Disk	16
3.2.5	Imaging using a Slit Aperture	19
3.3	Fluorescence Lifetime Measurements	20
3.3.1	Time-Gated Fluorescence Lifetime Measurements	20
3.3.2	FLIM Data Analysis	22
3.3.3	Rapid Lifetime Determination	24
3.3.4	Time-Correlated Single Photon Counting	26
4	Requirements of Fluorescence Imaging to Source Properties	28
4.1	Spectrum	28
4.2	Diffraction-Limited Beam Quality, High Brightness	28
4.3	Power	29
4.4	Pulse Duration, Repetition Rate	29
4.5	Polarisation	30
5	Optical Properties of the used Microstructured Fibre	31
5.1	Dispersion, Phasematching	31

5.1.1	Measurement of the Fibre Dispersion	31
5.1.2	Calculation of the Fibre Dispersion and Phase-Matching	32
5.2	Single-Mode Operation	33
5.3	Experimental Setup	34
5.4	Spectrum	35
5.4.1	Spectrum vs. Pump-Wavelength	35
5.4.2	Determination of the Short-Wavelength Side of the Spectrum	36
5.5	Relative Intensity Noise	38
6	FLIM using the Tunable Continuum Source	43
6.1	Wide-field Optically-Sectioned FLIM using a Nipkow disk	43
6.1.1	Experimental Setup	44
6.1.2	Spectrum of the Tunable Continuum Source	44
6.1.3	Specifications of the Nipkow Disk Unit	47
6.1.4	Time-Gated FLIM Unit	48
6.1.5	Acquired Lifetime Maps	49
6.2	Time-Correlated Single Photon Counting	51
6.2.1	Experimental Setup	51
6.2.2	Specifications of the Counting Card	51
6.2.3	Application	53
6.3	Spectrally and Temporally Resolved Imaging	58
6.3.1	Experimental Setup	58
6.3.2	Application	60
6.4	Wide-field FLIM	65
6.4.1	Experimental Setup	65
6.4.2	Application	67
6.5	Compression	69
7	Conclusion	72
7.1	Summary	72
7.2	Outlook	73
	References	77
A	Selection of Wavelengths from the Continuum Source	86
A.1	Prism-Monochromator	86
A.2	Interference Filters	87

1 Introduction

The present availability of excitation wavelengths imposes limitations on fluorescence imaging. While this biomedical research technique [1] can utilize intrinsic autofluorescence from a sample, its major use is to image the fluorescence from various exogenous fluorophore labels that are attached to specific constituents of the sample. As the different types of fluorophores exhibit different characteristic absorption spectra, a critical component for any fluorescence imaging system is the excitation source.

Traditionally, light sources that are used for wide-field fluorescence microscopy (i.e., camera-based systems) include, most commonly, mercury and xenon arc lamps as well as incandescent halogen lamps [2]. Spectral tuning is usually achieved with interference and absorption filters. Because of the poor spatial coherence of these sources, they are not suitable for confocal imaging [3,4]. Thus, point-scanning confocal microscopy is restricted in the wavelength of the source to the lines from available lasers. In particular, there are a limited number of (tunable) lasers covering the visible spectrum.

Conventionally, fluorescence microscopes only have access to a few excitation wavelengths (e.g., from the Argon ion, Krypton ion, HeNe and HeCd laser). In general, this places an arbitrary constraint on the design and selection of fluorescence probes for biological experiments, which must be excitable by the standard laser excitation lines, and thus, limits the science that can be undertaken in many laboratories.

Dye lasers can provide tunable visible radiation for fluorescence imaging, but this is usually limited to tuning ranges of $\sim 100nm$ and their experimental complexity precludes them from real-world applications [4]. Mode-locked solid-state lasers (e.g., Ti:sapphire laser) produce tunable ($\sim 0.7 - 1\mu m$) ultrashort pulses with hundreds of milliwatts of average power and can be employed in multiphoton microscopy [5,6]. This type of imaging can alleviate the problem to some extent, however, the available spectral range of the Ti:sapphire laser fails to efficiently excite fluorophores above $\sim 500nm$ via two-photon absorption. In addition, multiphoton imaging is not always desirable. For single photon excitation, second-harmonic generation and optical parametric amplification allows to obtain tunable radiation in the visible. However, a hands-off system covering the ultraviolet, visible and infrared spectral range is complicated to realise and prohibitively expensive.

This diploma thesis concerns the application of novel fibre-based tunable continuum sources to multidimensional fluorescence microscopy. These sources can provide broad spectral coverage ($\sim 0.4 - 1.5\mu m$) and are spatially coherent so they are suitable for

confocal microscopy. They are inherently pulsed on ultra-fast timescales and so are also suitable for fluorescence lifetime imaging (FLIM) and related time-resolved imaging modalities. A fully automated spatially coherent source, electronically tunable across the visible spectrum, would be invaluable for fluorescence imaging and provides new opportunities, e.g. automated excitation fingerprinting. Compared to frequency-doubling and optical parametric amplification using the tunable Ti:sapphire laser, this approach is less complex, less expensive, and more compact.

The underlying physical principle of the novel tunable continuum source is the generation of a supercontinuum [7–9] followed by spectral selection. The visible continuum is produced by injecting (infrared) femtosecond pulses into a microstructured fibre. Recently, Prof. Paul M. W. French’s Photonics group at Imperial College London has demonstrated such a versatile tunable continuum source for fluorescence imaging applications [10].

This diploma thesis is organised as follows. Section 2 provides a brief introduction to supercontinuum generation. Section 3 summarises the basics of fluorescence, the approaches to map the fluorescence lifetimes and the involved imaging modalities. Section 4 builds on the previous section to provide characteristics of a tunable continuum source suitable for fluorescence imaging. Section 5 presents the optical properties of the microstructured fibre, which is used in the FLIM experiments. Section 6 deals with the application of the tunable continuum source to FLIM. The experiments took place in Prof. Paul French’s Photonics group at Imperial College London. Finally, section 7 concludes with a summary and an outlook to future developments of fibre-based sources for biomedical optics and presents other potential applications within this field.

2 Basics of Continuum Generation

Supercontinuum generation is a nonlinear phenomenon, which exhibits dramatic spectral broadening of (pulsed) laser light passing through a nonlinear material. Thereby, the interplay between dispersion and nonlinearity is essential for efficient frequency conversion. In particular, the possible generation and the spectral bandwidth of the supercontinuum are affected sensitively by dispersive properties.

2.1 Dispersion

Temporal pulses comprise a spectrum of sinusoidal waves spread over a finite band in frequency-domain. Thereby, the time T and the angular frequency ω are conjugated variables. The product of the root-mean-square widths of the temporal pulse profile and its corresponding spectrum obeys an uncertainty-principle [11]: $\Delta T_{\text{RMS}} \Delta \omega_{\text{RMS}} \geq \frac{1}{2}$. In the experiments, short pulses ($\sim 100 \text{ fs}$) are used to generate the supercontinuum. According to the uncertainty-principle they have broad spectral profiles, which make them sensitive to spectrally selective processes such as dispersion.

One observable consequence of dispersion is that different frequency components of an optical pulse will propagate at different 'group' velocities v_G through a dispersive medium of physical length L resulting in different propagation times $t(\omega) = L/v_G = L\beta^{(1)}(\omega)$, whereby $\beta^{(1)}(\omega)$ is the first derivative of the propagation constant $\beta(\omega) = n_{\text{eff}}(\omega)\omega/c$. The effective index n_{eff} describes the physical property of the optical medium. For a pulse of bandwidth $\Delta\omega$, the spread in propagation times for the different frequency components is given by $(dt/d\omega)\Delta\omega$. Dispersion is often defined as pulse broadening per bandwidth:

$$\frac{dt}{d\omega} = L \frac{d}{d\omega} \frac{1}{v_G} = L\beta^{(2)}(\omega). \quad (1)$$

The dispersion parameter $D(\lambda)$ and the 2nd derivative of the propagation constant $\beta^{(2)}(\omega)$ represent dispersion as a function of vacuum wavelength λ and frequency, respectively,

$$D(\lambda) = \frac{1}{L} \frac{dt}{d\lambda} = \frac{d}{d\lambda} \frac{1}{v_G} = -\frac{2\pi c}{\lambda^2} \frac{d}{d\omega} \frac{1}{v_G} = -\frac{2\pi c}{\lambda^2} \beta^{(2)}(\omega), \quad (2)$$

where c is the speed of light in vacuum.

Dispersion also gives rise to a frequency chirp $\delta\omega(T)$ of a pulse, which can be interpreted as a shift of the instantaneous frequency $\omega(T)$ from the nominal oscillation at a carrier

frequency ω_0 [12]. A positive frequency chirp (up-chirp) can be observed as an increase in frequency with time and a negative frequency chirp (down-chirp) corresponds to a decrease in frequency with time. This can be expressed via the temporal derivative of the phase ϕ ,

$$\delta\omega(T) = -\frac{\partial\phi}{\partial T}. \quad (3)$$

In the anomalous dispersion region ($D(\lambda) > 0$), lower frequencies propagate more slowly than higher frequencies producing a negative frequency chirp. A positive chirp occurs in the normalous dispersion region ($D(\lambda) < 0$) where the lower frequencies are faster.

When dealing with pulse propagation in fibres, material dispersion as well as waveguide dispersion need to be considered [12]. The frequency dependent behaviour of the refractive index $n(\omega)$ causes material dispersion. It is directly connected to absorption via the Kramers-Kronig relations [13–15]. In a lossless, uniform (with respect to z) wave-guiding structure - given by a refractive index cross-section $n(x, y, \omega)$ - an eigenvalue equation for the transverse electric field in the m th mode, $\hat{\mathbf{E}}_{t m}(x, y, \omega)$ - with the square of the mode-propagation constant $\beta_m^2(\omega)$ as an eigenvalue - can be derived from Maxwell equations [16, 17]. Numerical simulations (e.g., finite element method, plane-wave method [18], multipole method [19, 20]) are required (particularly, for multi-mode fibres) in order to obtain dispersion, and thus, to characterise dispersive pulse propagation. Several configurations have been used to measure dispersion in optical fibres, for instance, Fourier transform spectroscopy [21–23], pulse-delay techniques [24, 25], and a method using spectral modulation [26–29].

2.2 Nonlinearity

A feature widely observed at almost all pulses of energy is that they disperse as they propagate. In contrast, optical solitons are self-localised pulses of light with the effect of temporal dispersion balanced by the nonlinearity of the medium in which they propagate. Hasegawa suggested soliton appearance in optical fibres [30], and Mollenauer went to report the first experimental observation [31].

Solitons exist because of the nonlinear effect called self-phase modulation. Generally, the phase of an optical signal can be modulated when the refractive index of a medium is modified. The change may be obtained via the intensity-dependency of the refractive index, $\tilde{n}(T) = n + n_2 I$, which describes the optical Kerr-effect. Where n_2 is the nonlinear refractive index (fused silica: $n_2 \sim 3 \times 10^{-20} \text{ m}^2 \text{ W}^{-1}$) and I is the intensity.

To acquire a change in the temporal phase profile, the timescale of the refractive index modification must be comparable to or faster than the timescale of the optical signal [32]. Self-action happens, if the refractive index is modified by the optical signal which experiences the phase modulation. This phenomenon is called self-phase modulation (SPM). If the refractive index is modified by a signal different to the one which is modulated, the effect is called cross-phase modulation (XPM).

While a consequence of dispersion is to produce a linear frequency chirp by redistributing in time-domain the frequency components of the optical signal, SPM produces a nonlinear frequency chirp by shifting some frequency components to new frequencies. In the anomalous dispersion region, the SPM-induced chirp can exactly balance the negative dispersion-induced frequency chirp. Therefore, the interplay results in maintaining a chirp-free pulse shape upon propagation. This picture is, however, vastly oversimplified and conceals a wealth of structure that can be seen in the mathematical solutions of the nonlinear Schrödinger equation [12, 33] (see also section 2.3.3).

The amount of fibre-nonlinearity is represented by the nonlinear parameter, which is given by

$$\gamma = \frac{\omega}{c} \frac{n_2}{A_{\text{eff}}}. \quad (4)$$

Although γ can be increased to some degree via a decrease of the effective cross-sectional area of the guided mode A_{eff} , however, it turns out that the shape and size of the core determines strongly dispersion, too. Thus, control of the dispersion profile $D(\lambda)$ is the key to engineering soliton dynamics [34].

2.3 Supercontinuum Generation via Microstructured Fibre

Widely broadened continua - extending from the violet to the infrared - can be conveniently generated with a (ultrafast) laser and a microstructured optical fibre (MF) [35].

2.3.1 Microstructured Fibre

A microstructured fibre is a strand of glass with an array of microscopic air-channels running along its length. A core can be created by filling one channel with glass; and the structured cladding provides wavelength-dependent index-guiding [36]. Because of their low loss and small mode-field areas A_{eff} , microstructured fibres are a means of gaining nonlinearity. In addition, the design of the microstructured fibre cross-section allows dispersion profiles to be tailored [34]. For instance, the zero-dispersion wavelengths (ZDWs) of these fibres can be shifted into the visible optical range [35],

whereas dispersion of conventional step-index fibers dispersion is usually governed by the dispersion of fused silica (ZDW at about $1.3\mu m$). In particular, this allows presence of anomalous dispersion, and thus, soliton dynamics in the visible spectral region. The dispersion profile can be also flattened [37]. Moreover, endlessly single-mode operation is obtainable [38–41]. Particularly, this is important for applications where a well-defined beam profile is required, e.g. microscopy. A more detailed discussion of microstructured fibres would be desirable but is beyond the scope of this report (Ref. [42] and references cited therein).

2.3.2 Higher-order Soliton Fission Mechanism

Through appropriate choice of dispersion, nonlinearities can be efficiently utilized to generate light at new wavelengths [43,44]. Nonlinearity includes the Kerr effect (which gives rise to self-phase modulation and self-steepening), and stimulated Raman scattering (e.g., see Ref. [12–14]).

Spectral broadening typical for self-phase modulation (SPM) can be found, when the pump frequencies of the short and intense pulses are located in the normal dispersion region. For an initially unchirped Gaussian pulse $|U(T)|^2 = \exp(-4 \ln 2 \frac{T^2}{(\Delta T_{FWHM})^2})$ of full-width at half maximum (FWHM) pulse-duration ΔT_{FWHM} , spectral broadening due to pure SPM is found to be given by

$$\Delta\omega_{SPM} = 2\sqrt{\frac{2}{e}} \frac{\gamma P_0 L}{\Delta T_{FWHM}} 2\sqrt{\ln 2}. \quad (5)$$

Where P_0 is the peak-power of the pulse and L is the length of the fibre. Usually, the obtainable spectral broadening due to self-phase modulation is an order of magnitude smaller than that observed with pumping in the anomalous dispersion region (however, there are exceptions, namely, when the soliton number is very small).

Supercontinuum generation using pulses with durations from femtoseconds to picoseconds is spectral broadening owing to evolution and fission of higher-order solitons [7, 43, 45, 46]. This is illustrated in Fig. 1. Initially, the interplay of SPM and anomalous dispersion results in formation of a N th order soliton, in addition, this stage is characterised by compression of the input pulse as well as expansion of the spectrum into the normal dispersion region of the fibre [47]. The spectral overlap of the pulse and a phase-matched dispersive wave results in the generation of the non-solitonic radiation [48]. The combined effect of higher-order dispersion, self-steepening and Raman scattering on a higher-order soliton is to split it into its constituents (with different

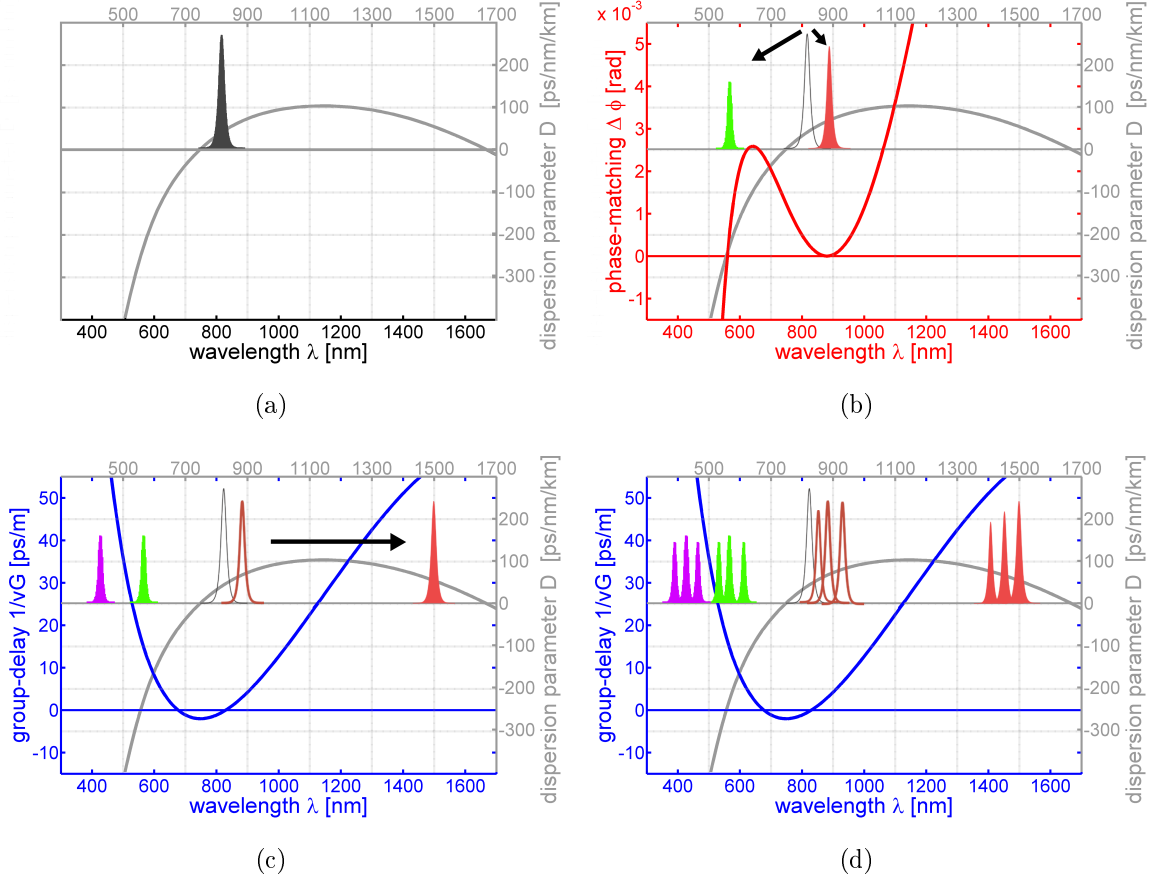


Figure 1: Schematic illustrating supercontinuum generation. (a): pump spectrum located in the anomalous dispersion region, formation of a higher-order soliton, (b): fission of the higher-order soliton by creation of fundamental solitons and emission of phase-matched dispersive waves, (c): Raman-induced soliton-self frequency shift to lower frequencies, and thus, lower group-velocities. Catching up of the dispersive waves in time-domain. Consequently, XPM-induced blue-shifts of the dispersive waves in the visible. (d): supercontinuum spectrum as a result of overlapping of multiple solitons and corresponding dispersive waves.

amplitudes and temporal widths) which propagate at different velocities [49, 50]. The onset of soliton fission can be identified by the appearance of multiple spikes in the temporal pulse profile and the appearance of non-solitonic radiation at higher frequencies. The separated short spikes are phase locked and satisfy the relation for a fundamental soliton [7]. In order to monitor the pulse evolution (in terms of both intensity and phase) experimentally, frequency-resolved optical gating is a technique [59, 134].

The phases of a soliton at angular frequency ω_s and that of the nonsolitonic radiation at ω are given by $\phi_s(\omega_s) = \beta(\omega_s)L - \omega_s L/v_{G_s} + \gamma P$ and $\phi_{\text{NSR}}(\omega) = \beta(\omega)L - \omega L/v_{G_s}$, correspondingly [43]. Thus, the phase-matching condition can be written as $\Delta\phi = \phi_s - \phi_{\text{NSR}} \stackrel{!}{=} 0$. Neglecting the nonlinear contribution γP and Taylor-expanding β until the n th polynomial order in the deviation $(\omega - \omega_0)$ from an arbitrary frequency ω_0 , the phase-matching condition is found to be given by

$$\Delta\phi = \sum_{r \geq 2}^n \beta^{(r)}(\omega_0) \left(\frac{1}{r!} [(\omega_s - \omega_0)^r - (\omega - \omega_0)^r] - \frac{1}{(r-1)!} (\omega_s - \omega) (\omega_s - \omega_0)^{(r-1)} \right) \stackrel{!}{=} 0. \quad (6)$$

It must be stressed that only the fibre-dispersion profile must be known in order to calculate phase-matching (and thus, ω_0 is the frequency where the dispersion is expanded from).

The spectral overlapping of several solitons at different frequencies as well as the different phase-matched spectral components in the visible results in an observable continuum.

As the solitons are shifted to longer wavelengths owing to Raman-induced soliton self-frequency shift ($d\omega_0/dz \sim (\Delta T_s)^{-4}$) [51–53], the phase-matched non-solitonic radiation usually occurs at shorter wavelengths, too. The soliton self-frequency shift may be limited by a second zero-dispersion point [53, 54] or OH absorption peaks.

An additional point to note is that the spectral distribution of the components in the visible can not be fully predicted by the phase-matched dispersive-wave generation. Often, the spectrum extends further into the blue than expected from the phase-matching condition. The Raman-induced soliton-self frequency shift, cross-phase modulation and dispersion are found to be the dominant effects which produce new blue-shifted spectral components on the short-wavelength side [55]. Cross-phase modulation also offers the opportunity of generating widely broadened blue spectral components by co-propagating a pump and signal pulse into a microstructured fibre [56].

A central point for the applicability of a fibre source to fluorescence microscopy is the

generation of blue spectral components. In a first approximation the location of the blue is given by the spectral position of the phase-matched dispersive wave, which in turn is described by Eq. (6). Keeping dispersion coefficients up to ($r = 4$) in this equation and choosing the soliton frequency as the expansion centre (i.e., $\omega_0 \equiv \omega_s$), the phase-matched components are given by [57]

$$\omega_{1,2} \approx \omega_s - \frac{2}{|\beta^{(4)}|} \left(\text{sgn}(\beta^{(4)})\beta^{(3)} \mp \sqrt{(\beta^{(3)})^2 - 3\beta^{(2)}\beta^{(4)}} \right). \quad (7)$$

Where the signs of the dispersion coefficients are usually given as $\text{sgn}(\beta^{(2)}) < 0$, $\text{sgn}(\beta^{(3)}) > 0$ and $\text{sgn}(\beta^{(4)}) < 0$, and the order of magnitudes are about $10^{-2}ps^{(2)}/m$, $10^{-5}ps^{(3)}/m$ and $10^{-8}ps^{(4)}/m$, respectively. When the initial wavelength is in the anomalous region, but in the range of dominating third-order and a small fourth-order dispersion coefficient, a strong peak on the blue side is expected. The observation of intense blue components, e.g., shown in Ref. [58] and [47], must be seen in consideration of this result.

For pulses with longer pulse durations (several ps , and $\sim ns$), for which the effects of SPM and self-steepening are negligible, stimulated Raman scattering and four-wave mixing play an important role [44, 135].

2.3.3 Modelling

The equation used to model the experiment is the so-called generalised nonlinear Schrödinger equation. Particularly, it provides a tool in order to grasp the complex soliton dynamics. The generalised nonlinear Schrödinger equation reliably describes the evolution of the slowly varying envelope of a pulse $U(Z, \tau)$ in a nonlinear optical waveguide. A split-step Fourier method can be employed to solve this fundamental equation [12]. The generalised nonlinear Schrödinger equation can be derived using coupled mode theory [16, 60]. The resultant equation is found to be given by

$$\left(i \frac{\partial}{\partial Z} + \sum_{r \geq 2} \frac{i^r}{r!} \frac{L_{D2}}{L_{Dr}} \text{sgn}(\beta^{(r)}) \frac{\partial^r}{\partial \tau^r} \right) U(Z, \tau) = -N^2 \left(1 + \frac{i}{\omega_0 \Delta T_0} \frac{\partial}{\partial \tau} \right) U(Z, \tau) \int_0^\infty d\tau' R(\tau') |U(Z, \tau - \tau')|^2. \quad (8)$$

In this equation ΔT_0 is usually set to the FWHM pulse duration, ω_0 is the pump frequency, $\beta^{(r)} = \partial^r (1/v_G)/\partial \omega^r$ (evaluated at $\omega = \omega_0$) is the r th dispersion coefficient, $L_{Dr} = \Delta T_0^r / |\beta^{(r)}|$ is the r th dispersion length, and

$$R(t) = (1 - f_R)\delta(t) + f_R \frac{\tau_1^2 + \tau_2^2}{\tau_1 \tau_2} e^{-\frac{t}{\tau_2}} \sin\left(\frac{t}{\tau_1}\right) \Theta(t) \quad (9)$$

is the (nonlinear) response function, which includes instantaneous electronic and delayed Raman contributions, the causality condition being taken into account through the Heaviside function $\Theta(t)$ (unity for $t > 0$ and zero for $t < 0$). The fractional contribution of the delayed Raman response is f_R . The parameters of the response function are taken from Ref. [12]: $f_R = 0.18$, $\tau_1 = 12.2\text{fs}$ and $\tau_2 = 32\text{fs}$. In Eq. (8) the time is in a reference frame co-moving at the group-velocity (evaluated at $\omega = \omega_0$). The propagation distance along the fibre is measured in units of the second-order dispersion length L_{D2} (i.e., $Z = z/L_{D2}$) and the amplitude of the electric field is measured in units of $\sqrt{P_0}$. The square of the soliton number N^2 is the ratio between the peak-power of the pump (P_0) and the peak power $(\gamma L_{D2})^{-1}$ necessary to create a single soliton in the ideal Schrödinger equation (that is, Eq. (8), neglecting the delayed Raman contribution and dispersion terms of order $r > 2$).

The left hand side of Eq. (8) describes dispersion, and the right hand side attributes to nonlinearity. One important parameter of the evolution is the soliton number N . The width of the continuum is increasing with soliton number N due to the fission mechanism during supercontinuum generation. In particular, higher-order solitons are only formed if $N > 1.5$. A favourable large value is associated with a high peak-power of the pump P_0 , a high fibre-nonlinearity (γ), low second-order dispersion $|\beta^{(2)}|$, and long initial pulse-durations ΔT_0 . The latter is in direct contrast to the behaviour of SPM-induced broadening where a shorter pulse yields a larger spectral bandwidth (Eq. (5)).

3 Fluorescence Lifetime Imaging

Fluorescence lifetime imaging (FLIM) is a technique in which the temporal profile of the fluorescence decay is measured at each spatially resolvable element of an imaging system. Here the optical resolution is limited, at best, to that of the image-forming devices. FLIM is a part of the broad field of biomedical optical diagnostics. In general, biomedical optical diagnostics may be considered as a synthesis of two main subjects, namely, spectroscopy and imaging [61]. The task of the spectroscopy is to detect and quantify variations in (biological) tissue properties, and can be chemically specific. The use of an imaging detector allows local heterogeneity to be monitored. In other words, it concerns the physical structure. The combination of imaging and spectroscopy allows a functional image to be obtained. Processes such as fluorescence link both subjects together, as it is electromagnetic radiation at optical frequencies, and its characteristics (intensity, lifetime, polarisation, absorption and emission spectrum, etc.) that allow spectroscopy to be undertaken.

Consequently, this chapter is made up as follows. Section 3.1 presents a brief introduction to the underlying principle of fluorescence so as to provide the basics for the spectroscopic part. Following this, section 3.2 discusses the different imaging modalities. Section 3.3 builds on the previous section to provide the techniques for FLIM.

FLIM may be important for fundamental biology research as it offers the opportunity to monitor experiments with cells. Lifetime measurements, in particular, can help to turn the spatial location of biochemical content with high degree of sensitivity and signal specificity into visible contrast [62–66]. In addition to the whereabouts of the fluorophore, the advantage of measuring the fluorescence lifetimes is that information about the molecular environment of labelled macromolecules and biochemical reactions in cells can be obtained [63]. This is due to the independence of the excited-state lifetime on local fluorophore concentration, excitation intensity (including uneven illumination or intervening absorption and scattering), photobleaching, light path length, fluorescence intensity, and nonuniform fluorescence collection efficiency but dependence upon excited-state reactions such as quenching and Förster resonance energy transfer.

FLIM is also a practical tool for drug discovery, and fluorescence techniques are being used as an aid in medicine, for instance, in photodynamic therapy of tumours [67]. FLIM could also be used for *in vivo* diagnostics to differentiate between normal and cancerous tissue, since malignant tissue can have a different fluorescence lifetime signature compared to that of benign biopsies [66].

3.1 Fluorescence

3.1.1 Phenomenon of Fluorescence

Because of radiative transitions from excited states, there is luminescence. This emission of light may be categorized into fluorescence and phosphorescence, depending whether the excited state is a singlet or triplet state, respectively. For excited singlet states the return to the ground state is spin allowed and occurs rapidly by emission of a photon. Typically, fluorescence lifetimes are on the order of nanoseconds. For excited triplet states transitions to the ground state are forbidden. Thus, the phosphorescence lifetimes of these metastable states are typically milliseconds to a few seconds. Phosphorescence is usually not seen in fluid solutions at room temperature. This is because there are competing deactivation processes, such as nonradiative decay and quenching processes [68]. When dealing with fluorescence it is common to illustrate the processes involved between absorption and emission of light via a Jablonski diagram [68]. Fig. 2 shows such a schematic.

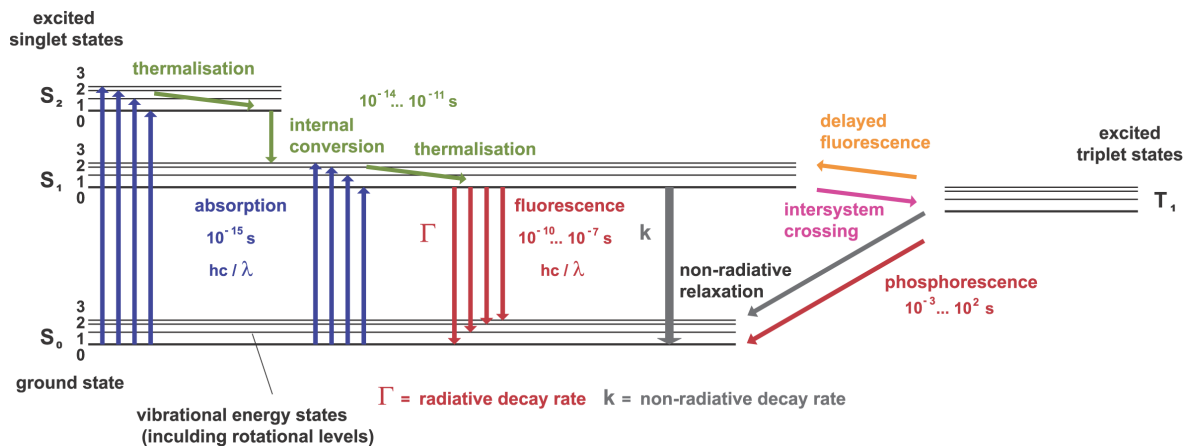


Figure 2: Jablonski energy level diagram. The singlet ground, first, second electronic states and first triplet state are represented by S_0 , S_1 , S_2 and T_1 , respectively. Numerous vibrational levels, denoted by 0,1,2, etc., exist at each of these electronic energy levels.

One observable property of fluorescence is that emission is shifted to longer wavelengths (Stokes' shift). Another quite general property of fluorescence is that the same fluorescence emission spectrum is generally observed irrespective of the excitation wavelength in a certain range (Kasha's rule).

3.1.2 Fluorescence Lifetime

Beside spectral properties of fluorescence, lifetime and quantum yield are perhaps the most important characteristics of a fluorophore [68]. For (single) exponential decays, the lifetime of the excited state may be defined as the average time the molecule spends in the excited state prior to return to the ground state. In other words, the lifetime determines the time available for the fluorophore to interact with or diffuse in its surrounding, and hence, information about the fluorophore surrounding (pH, viscosity, etc.) is obtainable. The lifetime of a fluorophore is given as

$$\tau = \frac{1}{\Gamma + k}. \quad (10)$$

Where Γ and k are the radiative and non-radiative decay rate, respectively.

It must be emphasised that the photon emission of fluorescence is a stochastic process. This forms the basis for a FLIM technique called time-correlated single photon counting (TCSPC). In this method a temporal histogram, characterising the fluorescence decay profile, is obtained.

3.2 Imaging

3.2.1 Overview

There are different fluorescence imaging instruments for different applications. The types of microscopes may be categorised into wide-field and scanning instruments [2]. The wide-field class includes conventional fluorescence and total internal reflection fluorescence microscopy. A camera is used to detect the fluorescence. The scanning category includes confocal, multiphoton microscopes and near-field scanning optical microscopes. Confocal and multiphoton microscopes work by scanning a single spot of light over the specimen. A unitary detector (photomultiplier tube or avalanche photodiode) may be used for detecting the fluorescence signal emanating from the sample. There are also parallel microscopes which involve the use of many confocal or multiphoton optical paths simultaneously and in parallel. At high speed an apparently continuous image is obtainable. That is why they are also referred to as wide-field optically-sectioned techniques.

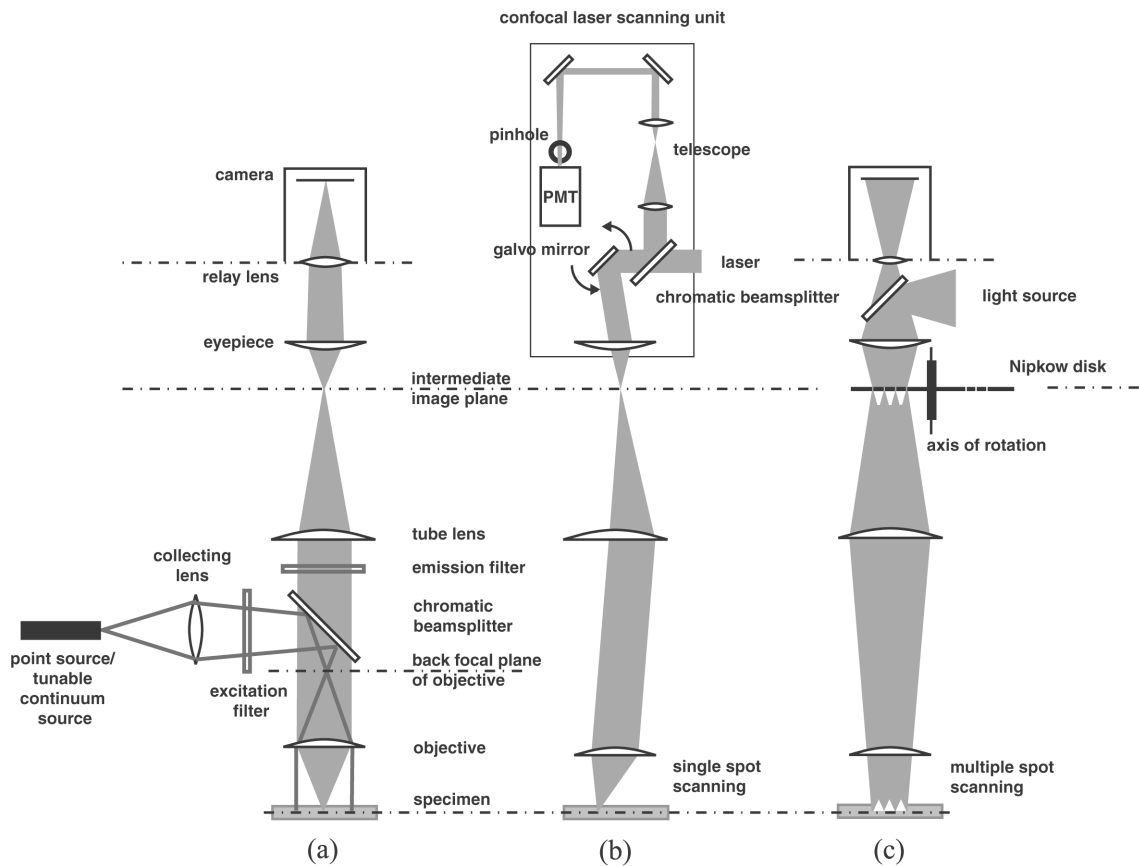


Figure 3: Three types of imaging instruments: conventional wide-field microscope, confocal laser scanning microscope, parallel microscope based on the Nipkow disk (after Ref. [2]).

3.2.2 Conventional Wide-Field Fluorescence Microscopy

A set-up for intensity imaging using a conventional wide-field fluorescence microscope in the epi-illumination mode is shown in Fig. 3(a). Köhler illumination is drawn for the illuminating light path, and the image-forming light path illustrates how fluorescence emitting from the sample is captured by the optics [69]. Due to the Stokes' shift of fluorescence, a chromatic beamsplitter can separate fluorescence emission from the excitation light. When dealing with broad-band sources, an excitation filter ensures that the sample is excited by a narrow spectral band. In addition, a neutral density filter may be used to attenuate the intensity. In order to further discriminate the fluorescence emission, a long pass emission filter is introduced into the detection path. Generally, the capability to differentiate between fluorescence and background light provides a high signal to noise ratio making fluorescence microscopy a highly sensitive method.

3.2.3 Confocal Microscopy

In a conventional wide-field microscope light emanating from features outside the focal plane is also detected. As a consequence, details in the image are blurred, and it is not possible to discriminate only the focal plane. In particular, this is a problem when imaging thick biological samples with depth of a few μm .

Fig. 4 illustrates the principle underlying confocal microscopy [4]. A complete image can be built up by scanning the specimen relative to a spot of light.

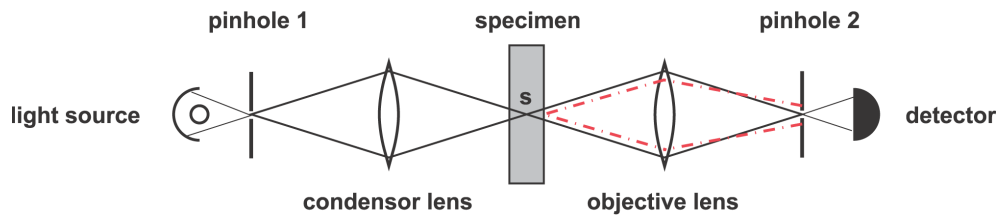


Figure 4: Principle of confocal microscopy. In this configuration, the specimen is stage-scanned.

In a confocal microscope the condenser of the conventional microscope is replaced by a lens identical to the objective lens. The field of illumination is limited by a pinhole, positioned on the optical axis. The condenser forms an image of the first pinhole onto a confocal spot (s) in the specimen. The exit pinhole, placed confocally to the illuminated spot in the specimen and to the first pinhole, prevents out-of-focus light reaching the detector. Consequently, out-of-focus points in the specimen are illuminated less by the first pinhole, and light emanating from this regions would not exit through the second pinhole.

Instead of trans-illuminating the specimen with a condenser and objective lens, separately, the confocal microscope is usually used in the epi-illuminating mode, making a single objective lens serve as both the condenser and the objective lens. Fig. 3(b) shows such a configuration. Instead of stage-scanning (x,y), a single spot of light is scanned over the specimen as speed matters in practice. Usually, a confocal microscope is implemented by attaching a commercially available confocal laser scanning unit to a standard microscope frame. In addition, when using a diffraction limited spatially coherent light source (e.g., laser, supercontinuum generation based on microstructured fibre) the first pinhole can be omitted. To build up an image, the detector response during scanning is used. By using a confocal laser scanning unit, it takes approxi-

mately a few seconds to produce a complete image at acceptably high resolution.

Beside reduced blurring of the image and increased resolution, there are several additional advantages of such a system: improved signal-to-noise ratio, the possibility to examine thick light-scattering objects, and the inclusion of z-scan allows three-dimensional quantitative studies of optical properties of the specimen. Furthermore, an infinite number of aperture planes are potentially available for modulating the aperture with phase plates, etc. Moreover, fluorescence lifetime measurements can be simply applied to this imaging method via time-correlated single-photon counting. The main drawbacks are the scanning process, which makes confocal microscopy slower compared with conventional wide-field microscopy. In addition, a spatially coherent light source is needed due to the confocal pinhole. Tunable spatially coherent sources are currently in their infancy. It is clear that a low cost all-fibre supercontinuum source would relax this limitation. Section 3.3.4 will deal with the application of supercontinuum (pumped with an Ti:sapphire laser) to biological confocal fluorescence microscopy [70].

A continuum source can also offer new options in confocal imaging, e.g. the broad spectrum can be used to focus different spectral components at different depths via chromatic aberration allowing depth scanning [71].

3.2.4 Wide-Field Optically-Sectioned Imaging using a Nipkow Disk

Sectioning is usually implemented in confocal laser scanning microscopy [4] or multiphoton microscopy [5]; fluorescence lifetime measurements can be added to these methods via time-correlated single-photon counting (section 3.3.4). However, pixel by pixel scanning places limitations on the speed. The Nipkow disk scanning system can overcome the speed limitations associated with single spot scanning while having optical sectioning. Fast time-gated fluorescence lifetime measurements (section 3.3.1) can be directly applied to Nipkow disk microscopy.

Fig. 5 shows a comparison between unsectioned wide-field intensity images and Nipkow disk images of a stained pollen grain. It can be seen that details of the specimen are revealed and out-of-focus light is suppressed by employing the Nipkow disk.

Although the confocality is somewhat diminished compared to confocal microscopy, the speed of image acquisition provides on-the-fly observation. This is of importance as numerous biological processes occur at a sub-second timescale. Wide-field real-time (up to 29Hz frame rate) fluorescence lifetime imaging has been demonstrated

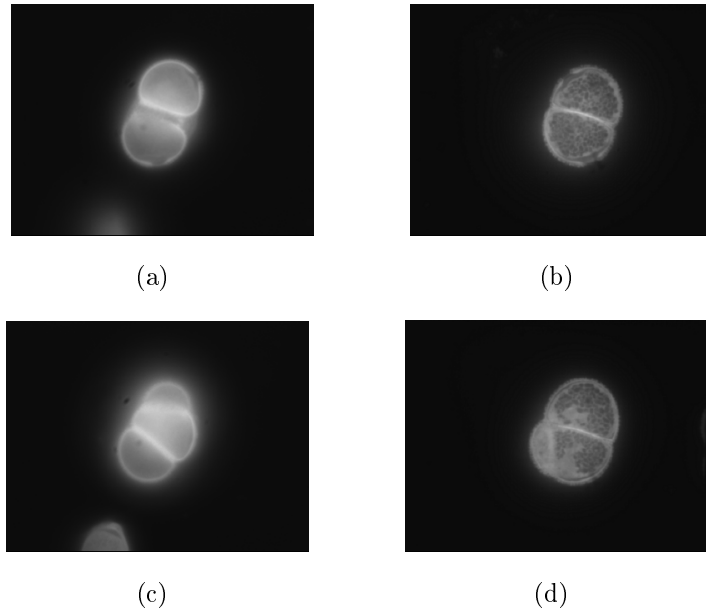


Figure 5: (a) and (c) show conventional images of the same pollen grain at two depths, and (b) and (d) show images recorded with the Nipkow disk unit. The axial separation between (a) and (c), and also (b) and (d) is $6 \mu m$ [72].

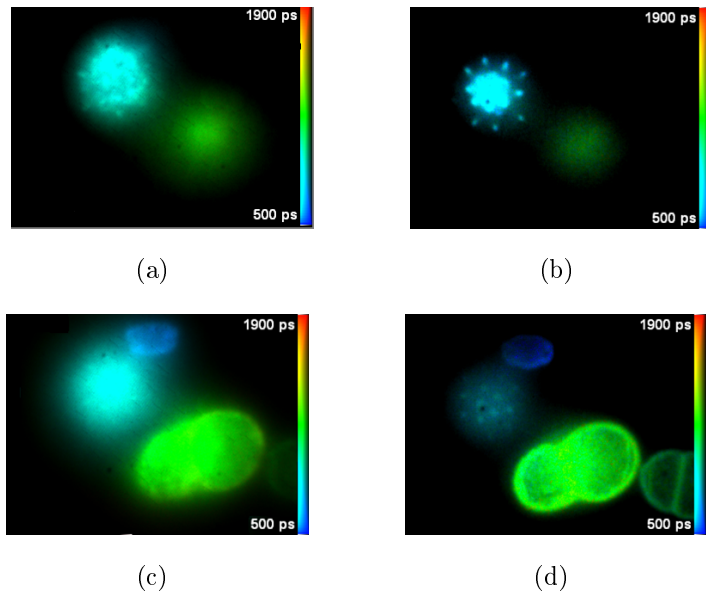


Figure 6: (a) and (c) show conventional merged fluorescence lifetime maps of pollen grains at two depths, and (b) and (d) show merged fluorescence lifetime maps recorded with the Nipkow disk unit. The axial separation between (a) and (c), and also (b) and (d) is $10 \mu m$ [72].

in conventional microscope, endoscope and plate reader configurations [73, 74], and frame-rates of up to 100 frames per second from a single-shot FLIM system were applied to image calcium signals in cells [75]. It is, however, desirable to acquire optically sectioned images so as to remove out-of-focus light and also to improve the accuracy of the calculated lifetimes. Fig. 6 shows a comparison between conventional and Nipkow disk wide-field FLIM. In these images the standard fluorescence intensity images are merged with the map of fluorescence lifetimes in order to form a weighted functional image. Not only has the sectioning increased the spatial information in the FLIM maps; it has also enhanced the fluorescence lifetime contrast between the different pollen grains.

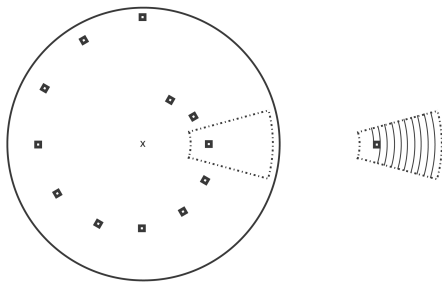


Figure 7: Schematic of a simple one frame per round Nipkow disk scanner

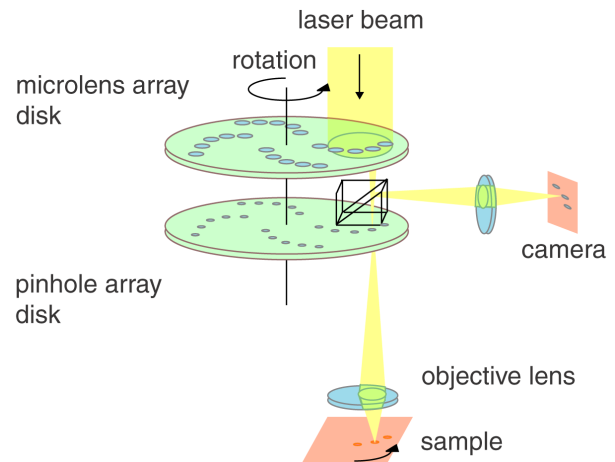


Figure 8: The basic idea how to enhance the light throughput by using a lenslet array

In Nipkow disk microscopes the arrangement of multiple apertures, which perforate a opaque disk, and spinning of the disk (Nipkow disk) generates a scanning in a raster pattern [76]. Fig. 7 illustrates how a simple one frame per round scanner works. In general, the design of the pinhole pattern allows the excitation light beams to uniformly scan a whole plane of the specimen by arranging the pinholes so that the pinhole pitch is the same in the radial and the angular directions [77]. The disk is placed in the intermediate image plane of the microscope and a large number of spots of light are focussed on the specimen plane. A schematic of the arrangement is shown in Fig. 3(c). The light emanating from each spot passes through the particular aperture from which it came. Thus, the opaque areas of the disk block out-of-focus light in the illumination and emission light path. When the disk is spun at high speed and its surface is viewed by means of an eyepiece or camera [78], an apparently continuous image is obtained.

Early forms of the Nipkow disk instrument were seldom used for low-light level fluores-

cence imaging, because only a few percent of the light generated by an arc lamp could pass through the disk. By incorporating a second disk, equipped with a microlens array focussing collimated laser light on corresponding pinholes in the lower disk, the light transmission can be significantly improved. A schematic of such a configuration is shown in Fig. 8. However, a major problem of Nipkow disk microscopes is still their poor light efficiency for fluorescence imaging. For this reason, powerful spatially coherent light sources need to be applied. On the other hand, the low instantaneous photon-flux per pixel of Nipkow disk scanning results in reduced photobleaching and photodamage compared to confocal microscopy.

Another drawback is the fixed pinhole size; patterned excitation microscopy concerns this issue by using spatial light modulators [79]. In addition, performance is also limited by a lack of synchronisation between the spinning disk and the CCD camera, particularly, for short CCD exposure times. Swept-field microscopy - combining stationary multiple apertures with scanning mirrors - addresses many drawbacks inherent in scanning-disk technology and allows higher frame rates [80].

Wide-field optically sectioned FLIM can also be achieved by combining structured illumination with time-gated FLIM [81–83]. Unfortunately, this technique exhibits a reduced signal to noise ratio in the sectioned images compared to directly acquired images, and does not work if the sample (e.g., living cells) moves during acquisition.

3.2.5 Imaging using a Slit Aperture

An alternative to Nipkow disk scanning in terms of optically-sectioned imaging at high speed is to use a slit as the aperture. It seems reasonable to assume that a slit-scanning system is again not quite as good as a confocal system at obtaining optical sections of thick specimen. However, the slit-scanning is fast and it provides substantial improvement over a conventional wide-field system. The confocal effect is given only on one axis. Because it is a wide-field technique, fluorescence lifetime imaging using a time-gated image intensifier can be directly applied.

To set up a slit scanner properly, an illumination line should be focussed in the aperture plane of the objective. This line is imaged onto the specimen plane as a line rotated 90° to the first owing to the Fourier transform taking place. In the experimental apparatus stage-scanning took place. When imaging biological samples, scanning an illuminating line over a resting specimen may be favourable (such systems are given in Ref. [4]). To record the image, a CCD camera is attached to the microscope.

One major advantage of slit-scanning imaging systems is that, unlike Nipkow disk scanning systems, they can efficiently utilize spatially coherent incident light. With the combination of a cylindrical and a standard imaging lens the incident beam can be fanned out and focused to a line. Thereby, there is little or no blocking. The uniaxial diverging lens has to be placed in the conjugate plane to the back aperture of the objective. High brightness, spatial coherence, ability to obtain diffraction-limited lines of illumination without the need of slit apertures make the tunable continuum source directly applicable for this method.

3.3 Fluorescence Lifetime Measurements

Fluorescence measurements can be broadly classified into two types of measurements, steady state and time-resolved [68]. The steady-state type is performed with a continuous beam of light illumination, and observation of emission intensity. Time-resolved measurements concern the acquisition of temporal intensity profiles. In general, there are two approaches, the time-domain and frequency-domain methods [64,68]. In this report, the time-domain method (or pulse fluorometry) is of interest. The sample is excited with a pulse of light which exhibits a duration much shorter than the decay time τ to be measured ($\sim ns$). Upon excitation, the temporal intensity profile is measured. Then, the fluorescence lifetime can be calculated from the slope of the curve. It is regarded to be a distinctive feature of the chemical compound and can be used for its identification. In particular, it provides an effective means to differentiate between fluorophores because spectrally overlapped signals may have distinct time behaviours. Two different time-domain methods will be discussed in the following, namely, a time-gated image intensifier technique and time-correlated single photon counting.

3.3.1 Time-Gated Fluorescence Lifetime Measurements

Time-gated fluorescence detection is the most direct method for measuring the lifetime. Fig. 9 illustrated the principle of the method. The sample is excited by a train of pulses at a repetition rate which allows the fluorescence to decay completely. Fluorescence emanating from the sample is detected in intervals during its temporal decay. In order to scan the temporal fluorescence profile, the delay of the time interval (gate) is varied with respect to the excitation pulse. At each delayed time gate, images of the sample are taken. This allows simultaneous acquisition of the temporal profiles of all resolvable elements. For the gating a certain width of the interval is chosen. Numerous

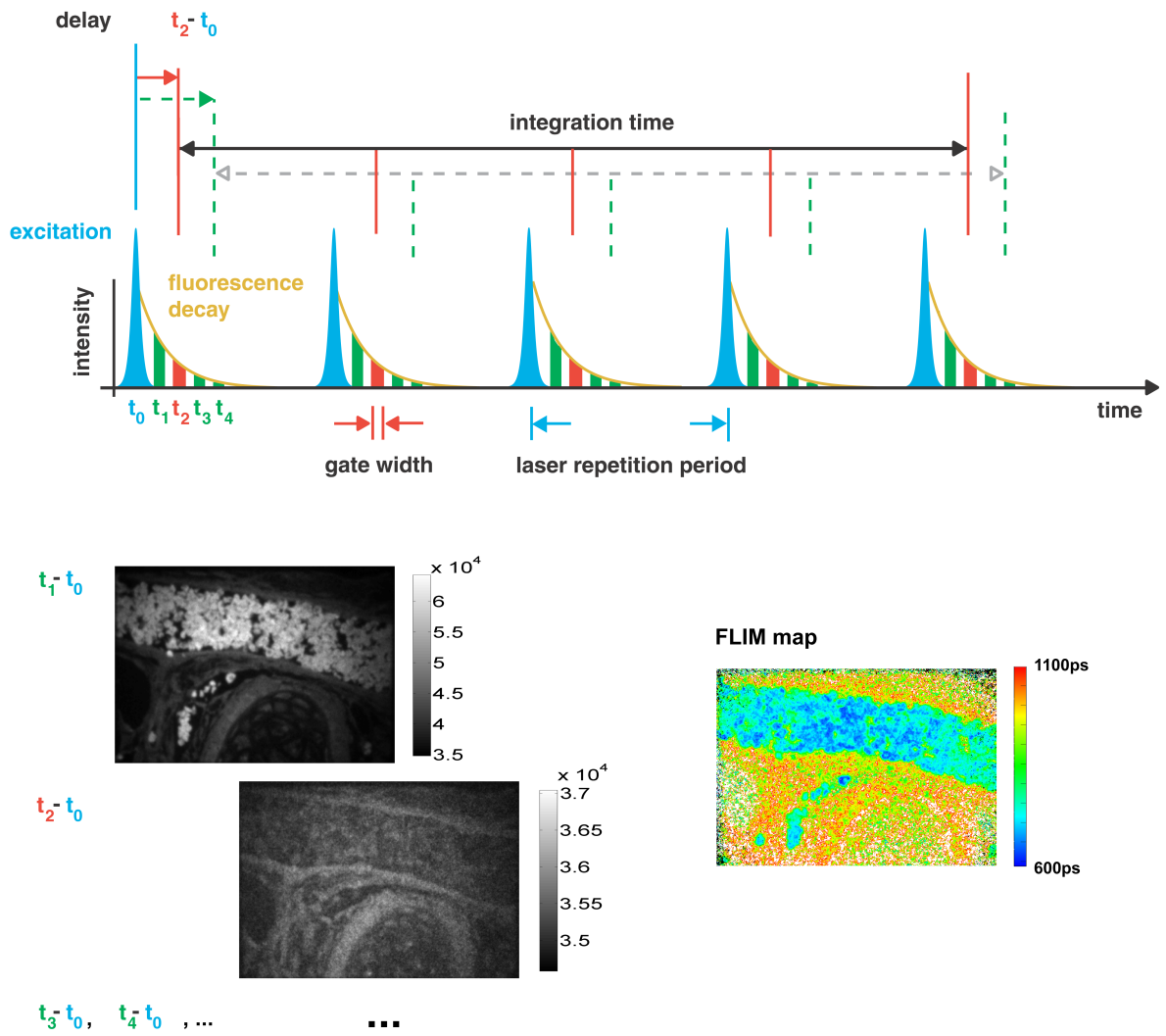


Figure 9: Time-gated fluorescence lifetime measurement

excitation-decay-cycles at the same delay are averaged so as to reduce the noise of the sensitive imaging system. The magnitude of signal can be raised by increasing the integration time of the detector camera. The set of acquired images corresponding to different delay times is then used for fitting an exponential decay-model at each image pixel, and as a consequence, the FLIM map builds up.

Gated detection can be accomplished by turning on or gating the gain of the detector for a short period during the intensity decay. This can be undertaken on a timescale adequate for resolving the lifetimes. The detector of choice is a gated optical intensifier connected to a CCD camera via relay optics. Gating is achieved by driving the photocathode of the intensifier (multichannel plate) with short voltage pulses, while the gain is kept constant (Fig. 10). A schematic of the FLIM unit applied to a conventional

wide-field fluorescence microscope is shown in Fig. 38 (section 6.4).

The main advantage of time-gated FLIM is that it is a fast wide-field technique. However, the main drawback of gated detection is the noise introduced on the signal by the light intensifier, and it is not so easy to directly estimate the uncertainties with the stroboscopic measurement for each data point.

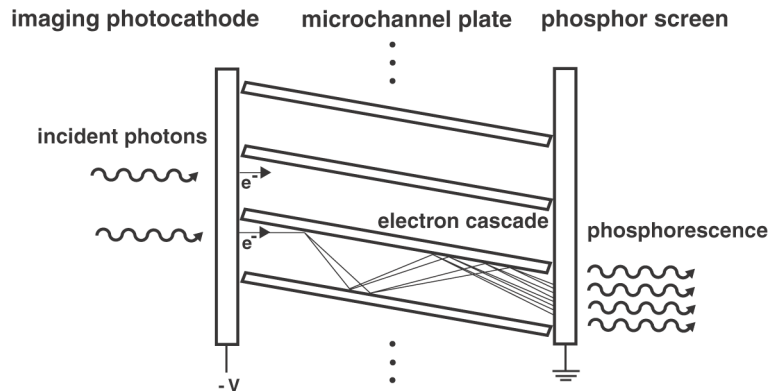


Figure 10: Schematic of the gated optical intensifier. The photodetector is based on the external photoeffect.

3.3.2 FLIM Data Analysis

Data of time-resolved fluorescence measurements are moderately complex and, generally, require numerical methods, such as nonlinear least-squares analysis. The main goal is to obtain the parameters for the assumed fluorescence decay I_{decay} from the experimental data (set of images).

The physical processes involved in FLIM can be differentiated into the generation of fluorescence via excitation pulses, and detection of the generated fluorescence via an instrument with a response function.

In general, FLIM requires short pulses. If the excitation pulses have durations which are not negligible compared to the time-scale of the fluorescence decay (I_{decay}), the generated fluorescence is a convolution of the pulses with the fluorescence decay profile. However, for short pulses with durations which are very small compared to the time-scale of the decay, it is usually a good approximation to assume the excitation pulse to be a δ -function. In this case, the generated fluorescence is actually equivalent to the shape of the fluorescence decay profile. The second step concerns the detection of the generated fluorescence. Here, the time-dependent instrument response function

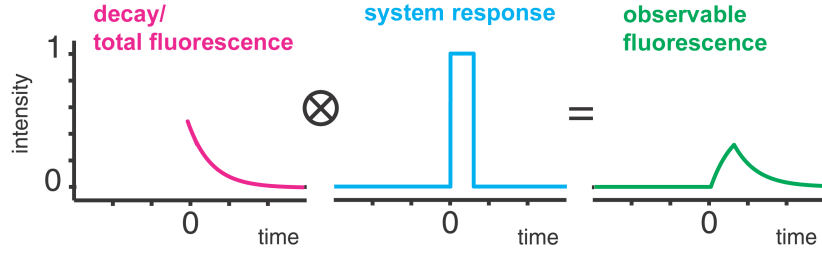


Figure 11: Detection of the generated fluorescence with the approximation of δ -function excitation (response-function of the instrument is normalised in the convolution).

$R_{detector}$ of the detector plays a role. The resulting observable fluorescence is a convolution of the generated fluorescence with the instrument response function. It goes without writing that the convolution theorem could be applied. However, with the approximation of δ -pulses, the observable fluorescence is given by

$$I_{\text{obs. fl}}(t) \sim \int_{-\infty}^{\infty} ds R_{\text{detector}}(t-s) I_{\text{decay}}(s). \quad (11)$$

The analysis is relatively simple, if the decays are single exponential:

$$I_{\text{decay}}(t) = A \exp\left(-\frac{t}{\tau}\right). \quad (12)$$

In the case of a rectangular gate, the instrument response function (IRF) is 1 between the k th delay-time (t_k) and the end of the gate of width w ($t_k + w$), and it is zero otherwise. In this case, the measured values at each image pixel (D_k , $k=1,2,3,\dots,N$, whereby N is the number of images) are represented by the integrated fluorescence intensity decay while the gate is open. According to (11) they are given by

$$I_{\text{obs. fl}}(t_k) = D_k = \int_{t_k}^{t_k+w} dt 1 \cdot A \exp\left(-\frac{t}{\tau}\right) \Theta(t). \quad (13)$$

where the Heaviside-function $\Theta(t)$ attributes to the fact that no fluorescence is emitted before the excitation while the gate could be opened before the emission of fluorescence (i.e., $t_k < 0$ possible). A continuous description for this relationship is shown in Fig. 11, whereby the delay times t_k take on all real values. A discrete set of profile points is expected as the result of the experiment because only a few delay times t_k are chosen. A nonlinear least-square method (e.g., Levenberg-Marquardt) can be applied to find accord - with respect to A and τ - between the experimental values and the simulated D_k -values. The deviation of the experimental values from the assumed profile is a quantifier for the quality of the fit.

If the fluorescence decay is only measured after the excitation pulse, i.e. the rising edge of the observable fluorescence can be neglected, then, the lifetime can easily be determined from the slope of $\ln(I(t))$ versus t by using linear regression methods. To consider a real instrument response function (i.e., drop the rectangular shape), the integral of Eq. (11) needs to be calculated for a set of time points (at which the IRF was measured). The idea of this data analysis is the same but the integrals need to be calculated numerically in general. However, it may be convenient to approximate the instrument response function via a super-shape composed of rectangular shapes with centres spaced at the distance of the experimental values (of the IRF measurement) in order to use an analytical integration, to speed up computation, and to proceed in a similar way as above.

In addition to single exponential decays, multiple exponential decays, continuous lifetime distributions, and stretched exponential functions are important in practice [68,84,85]. Particularly, when imaging biological samples there are many situations in which one does not expect a limited number of discrete lifetimes. For instance, a fluorophore in a mixture of solvents, such that there exists a range of fluorophore environments [64]. Then, one can also assume a continuous lifetime distribution. To model the fluorescence emission of biological samples, an equivalent expression is the stretched exponential function [86] given by

$$I_{decay}(t) = A \exp\left(-\left(\frac{t}{\tau}\right)^{\frac{1}{h}}\right), \quad h \geq 1. \quad (14)$$

Where τ is a characteristic time constant and h is the heterogeneity parameter. Again, the nonlinear least-squares method can be used to analyse the data.

3.3.3 Rapid Lifetime Determination

Acquisition of only a few images for the FLIM map allows increasing the speed of FLIM- measurements. Rapid lifetime determination concerns this matter. In particular, this is important for time-gated FLIM using image intensifiers. It is common to consider just single exponential decays for image processing even if a wide range of fluorophores and subenvironments are present in a sample, and hence, a stretched exponential function would be more appropriate [84]. In particular, the speed of data analysis favours the single exponential model, which still provides useful contrast. Particularly, in biological tissue imaging one is interested in reproducible lifetime contrast acquired, processed and displayed in the shortest possible time. In addition, Förster resonance energy transfer (FRET) - being important in modern biological research -

can be detected by their means.

For rapid FLIM the acquisition of only two images [87] would be the fastest option possible. However, instabilities originating from the laser and the light intensifier are likely to affect the measured lifetimes significantly (terms for the uncertainties of τ and A are given in Ref. [87]). It can be shown that there exists an optimal temporal region for the estimate of the lifetime. The two-gate rapide lifetime determination approach is effective for samples exhibiting only a narrow range of fluorescence lifetimes; it becomes problematic for samples exhibiting a range of lifetimes. Thus, it is better to acquire more than two images [64].

In the experiment three time-gates were used. And, instead of applying nonlinear fitting methods, a rapide lifetime determination method is employed [87,88]. Although the precision can be worse, it is much faster than iterative nonlinear schemes. As a consequence, this method should be useful in a variety of real-time applications, such as endoscopic FLIM and multi-well readers [74]. A graphical description of the quantities involved is shown in Fig. 12.

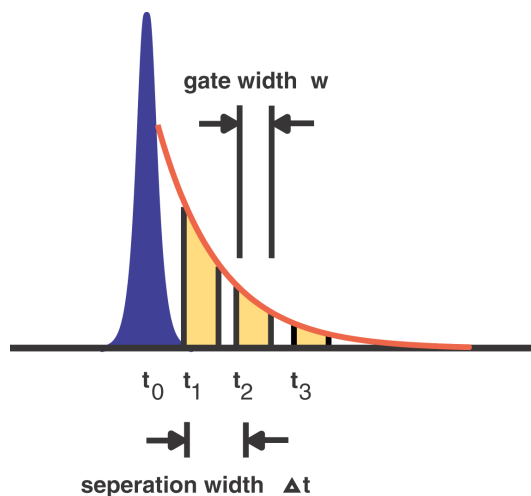


Figure 12: Rapide lifetime determination method.

In the three-gate case, a decay with non-zero baseline of the form

$$I(t) = A \exp\left(-\left(\frac{t - t_0}{\tau}\right)\right) + B \quad (15)$$

is assumed. Where τ is the lifetime, A is the preexponential factor and B is the baseline. The baseline accounts for a situations where a weak signal is on a slowly varying decaying background (e.g., a fluorescence on a phosphorescence signal) [88].

In the experiment the decay is sampled by three consecutive gates. The areas of the integrated decay are

$$D_k = \int_{t_k}^{t_k+w} dt I(t), \quad (16)$$

where $k = 1, 2, 3$. Explicit integration using the decay model, Eq. (15), results in expressions for the parameters of the model:

$$\begin{aligned} \tau &= \frac{\Delta t}{\ln\left(\frac{D_1 - D_2}{D_2 - D_3}\right)} \\ A &= \frac{D_1 - D_2}{\tau} \frac{1}{(1 - \exp(-\frac{w}{\tau})) (1 - \exp(-\frac{\Delta t}{\tau})) \exp(-\frac{t_1 - t_0}{\tau})}, \\ B &= \frac{1}{w} \left(D_2 - \frac{D_2 - D_3}{1 - \exp(-\frac{\Delta t}{\tau})} \right). \end{aligned} \quad (17)$$

The uncertainty in τ can be derived by using the Gaussian error propagation method [88]. A comparison of methods for rapid evaluation of exponential decays (rapide lifetime determination, maximum likelihood estimator method, phase plane method) is given in Ref. [89]. The different techniques are compared with respect to precision, accuracy, sensitivity to binning range, and the effect of baseline interference.

3.3.4 Time-Correlated Single Photon Counting

An alternative to time-gated FLIM is time-correlated single photon counting (TCSPC) using a confocal microscope [90–93]. It is a widespread time-domain technique for counting photons which are time-correlated in relation to the excitation pulse. The apparatus for TCSPC consists basically of a pulsed laser with a high repetition-rate and a time-to-amplitude converter [68]. The role of the time-to-amplitude converter is to measure the time between the excitation pulse and the first arriving emitted fluorescence photon. This is accomplished by charging a capacitor. The voltage ramp is stopped when the first fluorescence photon emanating from the sample is detected by a photomultiplier tube. For triggering the voltage ramp of the time-to-amplitude converter, a high-speed photodiode monitors the excitation pulses of the laser-output. An electrical pulse is provided at the output of the time-to-amplitude converter. Then, the multichannel analyser converts the received voltage into a time channel using an analog to digital converter. Finally, the multichannel analyser builds up a probability histogram of counts versus time representing the fluorescence decay.

In general, the time-to-amplitude converter is a rate-limiting component. It takes several microseconds to discharge the capacitor and reset the time-to-amplitude converter.

To solve this problem reverse mode operation is used, thereby, the detected photon serves as a start pulse and the next excitation pulse is the stop signal. Once a photon is detected, the dead time of the electronics prevents detection of another photon. For older TCSPC systems this used to result in a time consuming measurement when scanning a whole image pixel by pixel. However, advanced TCSPC devices (e.g., 'Becker& Hickl') achieve useful count rates of the order of several $\sim 10^6$ photons/s and effective recording times of less than 1 ms per decay curve [94]. The overall dead time is about 125 ns per detected photon. The acquisition time for TCSPC lifetime measurements can vary between a few seconds up to half a hour depending on the photostability of the sample, the number of spatial pixels, and the accuracy (number of counts) needed for answering the particular question of the experiment. The maximum count rate is limited rather by the photostability of biological samples than by the counting capability [94]. A main advantage of TCSPC is its high accuracy, i.e., the apparatus is in principle shot-noise limited.

The data obtained via TCSPC can be analysed analogous to the time-gated technique. Whereas the time-channels of the TCSPC method for each pixel are equivalent to the set of images of time-gated FLIM.

4 Requirements of Fluorescence Imaging to Source Properties

4.1 Spectrum

Ideally, a flat high-power spectrum covering the ultraviolet, visible and infrared part of the electromagnetic spectrum is needed for fluorescence microscopy. This is because the numerous available fluorophores have each a different absorption spectrum.

The ultraviolet and visible part of the spectrum are important for single photon excitation. In particular, in fundamental molecular biology research fluorescently labelled marker molecules - which usually absorb in the visible spectral range - are in use. These extrinsic fluorophores are added to the sample to provide fluorescence when none exists or to change the spectral properties of the sample. To investigate biological tissue via autofluorescence *in vivo* and *in situ* ultraviolet excitation is necessary. This is important for the direct observation of living cells using FLIM, e.g., application in medical surgery (using endoscopy). The infrared spectral range is important for multiphoton microscopy.

In general, the spectrum needs to be flat on a linear (not logarithmic) intensity scale since some techniques (e.g., spectral imaging) require a number of excitation wavelengths in the same experiment. Thereby, the fluorescent tissue may be excited with multiple wavelength at a constant intensity level simultaneously or sequentially.

4.2 Diffraction-Limited Beam Quality, High Brightness

Microscopy applications of fibre-based light sources require single-mode operation (\sim Gaussian [16]) since this mode produces the smallest beam divergence, the highest power density, and, hence, the highest brightness [95]. Focusing a single-mode beam by an optical system will produce a diffraction-limited spot of maximum power per unit area. Furthermore, the radial profile of the fundamental mode is smooth, whereas multimode operation leads to the random occurrence of local maxima in intensity. Precise imaging systems (e.g., pointspread-function-engineered superresolution instruments) rely on excellent beam quality. For certain fibre cross-sections [39], endlessly single-mode operation can be easily obtained.

In many applications, particularly for confocal imaging, it is a high brightness (power/area/solid-angle divergence of the beam) rather than large total emitted power that is

desired from the source. The use of fibre amplifiers is of great interest in the design of high-energy, high brightness fibre-sources. In an amplifier the combined action of self-phase modulation, normal dispersion and gain may result in linearly chirped parabolic pulses at high power levels [96–100]. In particular, the linear chirp of these optical wave breaking-free pulses allows efficient pulse compression via a dispersion-induced negative chirp [101]. For a given fibre dispersion $\beta^{(2)}$ and nonlinearity parameter γ , Ref. [96] gives design criteria for efficient parabolic amplification in terms of initial pulse duration and energy, and propagation length. In combination with a master fibre-oscillator to generate the seed and a microstructured fibre to produce the continuum, this approach allows the design of a versatile high average power all-fibre source being applicable in linear and nonlinear spectroscopy.

4.3 Power

The estimation of Ref. [4] results in an incident spectral power of $1 - 2mW$ the source must furnish to be usable for fluorescence detection in confocal microscopy. At first sight this seems quite low, however, this implies $1 - 2mW$ per nm within the continuum, if a highly discriminated spectrum ($\sim 1nm$) is required. The low damage threshold of the microstructured fibres because of the small core diameters, in particular for fibres with short zero-dispersion wavelengths, may be a limitation for a high spectral power. Fortunately, the spectral features of the absorption spectra of most fluorophores are hardly less than $\sim 5nm$, consequently, this alleviates the spectral power demand. On the other hand, spectral imaging using multiple labels and overlapping emission spectra may restrict spectral excitation bandwidths to less than $10nm$, thus, increasing the required spectral power. When sufficient power is provided by the light source, photochemical processes and the type of sample crucially determine the power level which can be used [4].

For a continuum source suitable for multiphoton microscopy, the flat spectrum should exhibit a spectral power of at least $3 - 5mW/nm$ while covering an optical range of $0.6 - 1\mu m$ at about picosecond pulse-duration and a repetition rate of 40MHz.

4.4 Pulse Duration, Repetition Rate

Pulsed lasers are useful in microscopy for two reasons: time-resolved measurements such as FLIM require pulsed sources, and they can be used to create the very high levels of peak power necessary to excite nonlinear phenomena (multi-photon excita-

tion) at a moderate level of average power [68]. In addition, if the source does not provide wavelengths in the ultraviolet, longer wavelengths can be converted to shorter ones by second-harmonic generation (SHG). This may be important for the excitation of intrinsic fluorophores (autofluorescence) to provide label-free molecular fluorescence lifetime contrast. It is clear that a continuum source inherently covering the excitation wavelengths for autofluorescence imaging would be the best option.

For most time-resolved measurements (time-domain) the pulses should be regarded as delta-functions (i.e., pulse durations $\sim \leq ps$) with respect to the fluorescence lifetime (usually $\sim ns$). In particular, this simplifies data analysis and avoids errors associated with de-convolution.

An additional point to note is that the width of the pulse provides also a basis for a promising superresolution technique called stimulated emission depletion (STED) [160]. Since superresolution techniques are increasingly being important for answering fundamental questions in biology, aspects like this should be kept in mind.

For fluorescence lifetime imaging, the right repetition rate is vitally important. For example, at a repetition rate of 100MHz, the pulses occur every $10ns$. One typically measures the intensity decay to about four times the mean decay time, so that fluorescence lifetimes times longer than $2.5ns$ are too long to be measurable at a repetition rate of 100MHz [68]. In practice a source at a repetition rate of about 40MHz would be appropriate.

4.5 Polarisation

The polarisation state of the output of the light source may be important for fluorescence polarisation anisotropy measurements which are commonly employed in biochemistry [68]. In order to obtain a well-defined polarisation state of the continuum output, polarisation-maintaining fibres must be used. Beside the significance of polarisation with regard to spectroscopy, it is also a means of increasing efficiency of polarisation-sensitive optical elements, e.g., compressor, stretcher, spatial light modulator, monochromator, etc.

5 Optical Properties of the used Microstructured Fibre

This section discusses the optical properties of the microstructured fibre 'crystal fibre NL-2.0-740', which was used in the subsequent fluorescence experiments. In particular, for the applicability of supercontinuum in fluorescence microscopy, the properties of the spectrum, namely, spectral range, flatness, bandwidth and power, are important criteria. Furthermore, the profile of the beam, i.e. single-mode operation, is of significance. In addition, pulse-to-pulse-noise of the continuum output may be relevant. In order to describe the location of the blue via the phase-matching condition, the dispersion of the fibre must be known. Consequently, this fibre characteristic has been measured.

5.1 Dispersion, Phasematching

5.1.1 Measurement of the Fibre Dispersion

A spectral white-light method – using the Mach-Zehnder interferometer – is employed so as to measure dispersion of a microstructured fibre. A schematic of the interferometer is shown in Fig. 13(a).

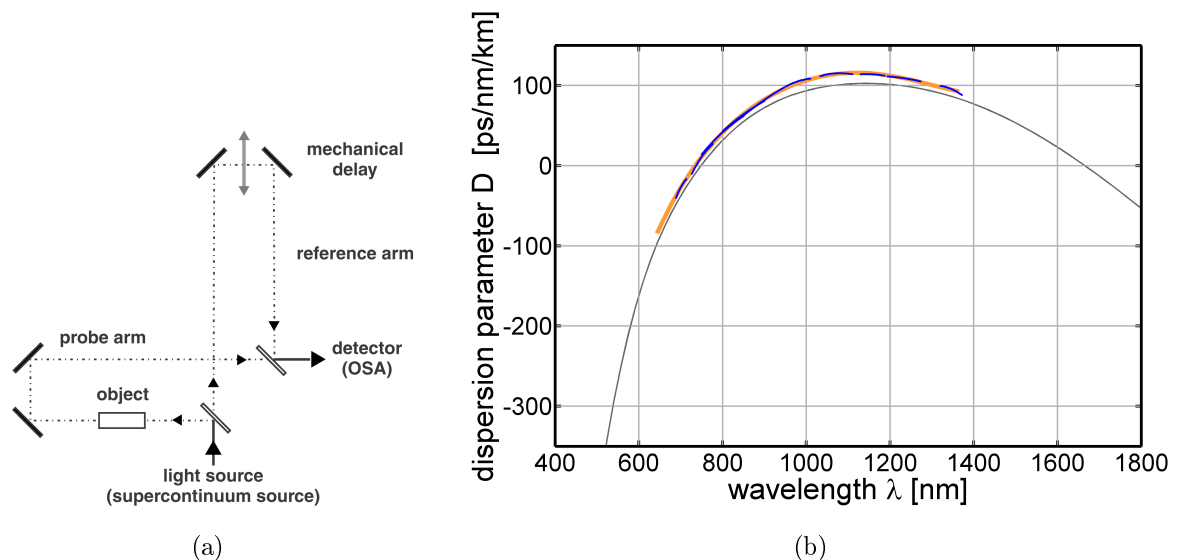


Figure 13: (a): Experimental apparatus for the dispersion measurement, OSA: optical spectrum analyser, (b): measured dispersion (blue), polynomial fit to the experimental data (orange) and theoretical estimation (grey)

The method is based on the fact that the intensity at the output is spectrally modulated by the interference term $2\sqrt{I_1 I_2} \cos(\delta)$. Where I_1 and I_2 are the intensities of the reference and the probe arm of the interferometer, respectively. The phase difference is $\delta(\omega) = \beta_{object}(\omega)L_{object} - \frac{\omega}{c}L_{air} + \theta$, where β_{object} is the propagation constant of the probe object (e.g., fibre), L_{object} is its length, L_{air} is the portion of the air path in the reference arm which compensates for the change in optical path owing to the insert of the object in the probe arm. The extra term θ accounts for any phase difference due to mismatch of both arms. From the equation for the phase difference δ follows that the second derivative of this equation in terms of frequency ω results in a quantity describing pulse broadening per bandwidth. The dispersion parameter $D(\lambda)$ can be calculated by means of Eq. (2).

A special feature of the experimental set-up is the use of a spatially coherent supercontinuum source for the dispersion measurement. In particular, this allows to measure dispersion over a wide spectral range ($\sim 800nm$ in the present case) while having a reasonable amount of brightness for a convenient data acquisition.

5.1.2 Calculation of the Fibre Dispersion and Phase-Matching

The dispersion profile of the fibre used in the experiments was calculated via symbolic trial-and-error expressions for the output of the finite-element method which are given in Ref. [102], and the result is shown in Fig. 14(a).

Phase-matching was calculated by using Eq. (6) and the resultant curve is shown in Fig. 14(b). Owing to the existence of two ZDWs, there are two dispersive waves for solitons at longer wavelengths. On the one hand, this allows generation of phase-matched dispersive waves in the infrared, and thus, an enhanced bandwidth of the supercontinuum on the long-wavelength side [53, 54]. On the other hand, this places a constraint on the energy transfer to the blue.

The choice of microstructured fibre (MF) and pump source naturally depends on the spectral range in which the light is to be generated. For the visible spectral range, the zero-dispersion wavelength of the fibre should not be far-off from the spectral region of interest. On the other hand, it should be close to the centre wavelength of the pump source so as to allow a 'continuous' spectrum on a linear intensity scale.

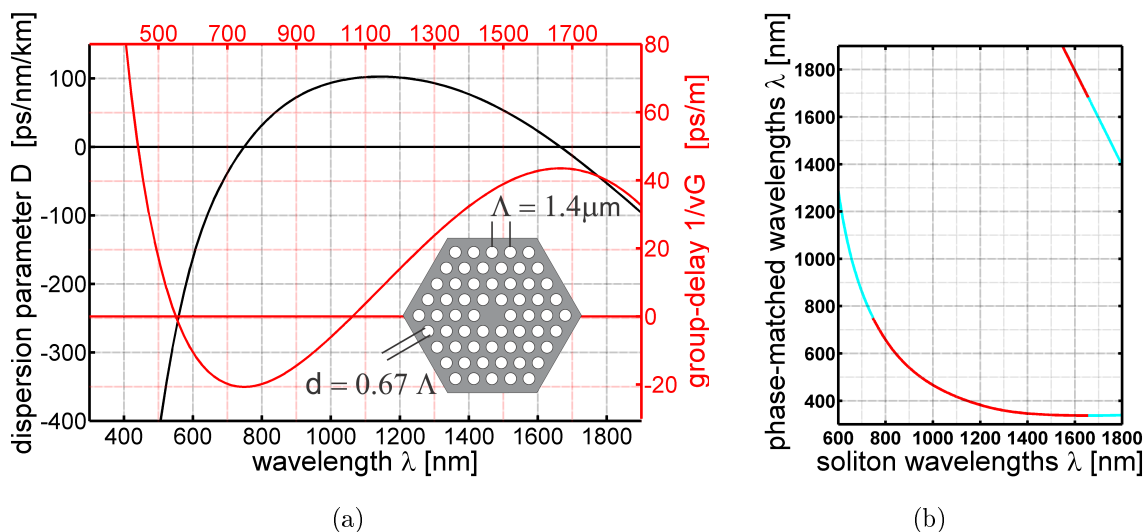


Figure 14: (a) Dispersion parameter D vs. wavelength (black line) and group-delay $1/v_G$ with respect to the group-delay at $\lambda = 550\text{nm}$ (red line) vs. wavelength for the air-silica microstructured fibre 'crystal fibre NL-2.0-740'. The inset shows the corresponding geometry of the cross-section for this fibre. (b) phase-matching between soliton and the nonsoliton radiation, where the red line corresponds to the relevant anomalous dispersion region

5.2 Single-Mode Operation

Another important fibre characteristic is single mode operation. The MF 'crystal fibre NL-2.0-740' has a hole-diameter to pitch ratio $d/\Lambda = 0.67$, consequently it is not endlessly single mode which requires $d/\Lambda < 0.45$ [40]. Fig. 15 illustrates the single-mode behaviour vs. wavelength which was calculated via a scalar approximation [103, 104].

The single-mode cut-off is found to be at a wavelength of 700nm , which agrees with the data given by the manufacturer [105, 106]. Whether single-mode cut-off is important or not is determined by the beam-profile of the pump source. In general, pumping with a single-mode source yields a single-mode continuum output, even in the range where the nonlinear fiber is multi-mode. If the fiber is also multimode at the pumping wavelength, it requires careful coupling to achieve single-mode operation. If strict single-mode operation is to be guaranteed or if the pump source is not single-mode, the fiber chosen should be single-mode at the pumping wavelength and ideally over the entire region in which one wishes to generate light [107].

As the present fibre is multimode in the visible, interferometric dispersion measurements are not so easy in this spectral range, i.e. requirement of long pieces of fibre for mode separation, temporal scanning, and a spatially coherent broadband single-mode

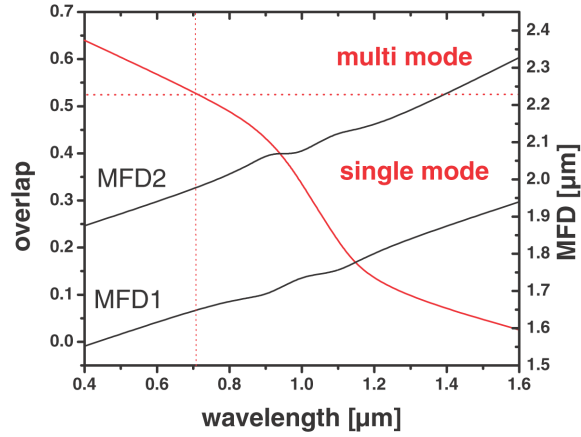


Figure 15: Relative overlap of the 2nd order mode (LP_{11}) with the effective core region (radius = $\Lambda/\sqrt{3}$). The single-mode cut-off is determined by the value of 0.52 which parallels to the conventional criterion $V < 2.405$. In addition, the mode-field diameters (MFDs) for the 1st and 2nd mode are shown.

light source across the visible and near infra-red region.

5.3 Experimental Setup

The following is concerned with the generation of blue and green components. For this purpose 0.75m length of air-silica MF 'crystal fibre NL-2.0-740' (mode-field diameter: $1.59\mu m$, ZDW at $740nm$) in combination with the Ti:sapphire laser 'spectra physics Mai Tai' (pulse width: $\Delta T_{FWHM} = 100fs$, repetition rate: 80MHz, tuning range: $710 - 990nm$) is used. In general, the required length of microstructured fibre depends on the pulse width of the pump source. Due to the nonlinear fibre-length $((\gamma P_0)^{-1})$, less than one metre of nonlinear fibre is generally sufficient for pump pulses on a timescale of a few hundreds of femtoseconds ($< 1ps$) whereas pump pulses on a nanosecond timescale need a fibre-length of a few metres.

A schematic of the experimental set-up for the tunable continuum source is shown in Fig. 16. The output of the pump Ti:sapphire laser is directed through an isolator and focussed by a 4.5mm focal length aspheric lens into the MF. A interference filter wheel was placed into the beampath so as to discriminate a part of the continuum for calibration and spectral intensity noise measurements.

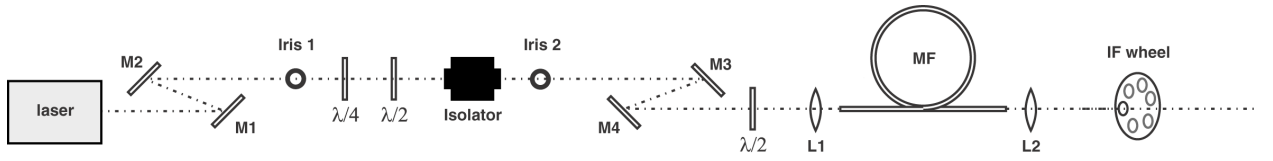


Figure 16: Experimental set-up for the tunable continuum source (TCS). M1-4, mirrors; L1-2, lenses; $\lambda/2$, half-wave plate; $\lambda/4$, quarter-wave plate; MF, microstructured fibre; IF wheel, interference filter wheel. The half-wave plate before the isolator serves as a variable attenuator. The quarter-wave plate compensates for ellipticity of the laser output.

5.4 Spectrum

5.4.1 Spectrum vs. Pump-Wavelength

The main limitation of continuum extension towards the blue is usually due to the relative location of the zero-dispersion point with respect to the pump-wavelength. The further the pump wavelength is tuned from the ZDW the deeper in the blue the short wavelength components are generated [54]. However, this occurs at the expense of increasing the width of the gap between the pump and the blue components, in addition, the amplitude of the blue components will reduce. For this reason the pump wavelength should not be tuned too far away from λ_{ZDW} so as to obtain a reasonable amount of blue. In particular, the tunability of the Ti:sapphire laser allows optimization of the supercontinuum with regard to fluorescence microscopy.

The short-wavelength sides of the supercontinuum spectra were recorded at different pump wavelengths (from 710nm to 890nm in 30nm steps). The obtained experimental data is shown in Fig. 17. It can be seen that the spectrum shifts towards the blue as the pump wavelength is increased. In general, this behaviour can be explained with the phase-matching curve for this fibre, Fig. 14(b).

A point to note is that the spectral power is shown on a linear scale. This is of particular importance as flatness of the spectrum can be only evaluated on this type of scale, whereas a logarithmic scale tends to emphasise values which are too small to be of use in practise. To label the ordinate with real units (e.g., mW/nm), a calibration is necessary. Provided the optical spectrometer detects the whole spectral range of the generated supercontinuum, the integration value of the spectrum is a quantity equivalent to the experimentally measured total output power. Thus, the raw spectrum can simply be calibrated via normalization and multiplication with the

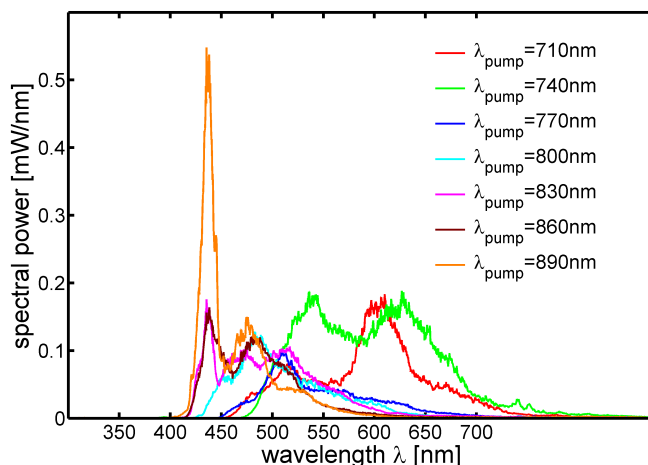


Figure 17: Short wavelength sections of the supercontinuum spectra of the MF 'crystal fibre NL-2.0-740' (length ca. $0.7m$) for different pump wavelengths (710nm, 740nm, 770nm, 800nm, 830nm, 860nm, 890nm). The input power was about 500mW and the (high) power transmission 0.20 at 710nm, 0.12 at 740nm, 0.14 at 770nm, 0.14 at 800nm, 0.15 at 830nm, 0.14 at 860nm, and 0.12 at 890nm.

total power. Generally, interference filters (with a known transmission function) can be applied. In the present case this method is inevitable as the optical spectrum analyser ('ocean optics') only covers a limited spectral section of the generated supercontinuum, in addition, it is not reliable for wavelengths longer than $700nm$. For the calibration of the spectra in Fig. 17 an interference filter ('comar 500 IU 25 T-DAB') at a centre wavelength of $500nm$ is used (compare Fig. 44). A reasonable overlap of the filter transmission function with all measured spectra is required for calibration.

For the fluorescence lifetime imaging experiments (section 6), the spectrum at a pump wavelength of $830nm$ was chosen from all the calibrated spectra. In particular, it exhibits a reasonable degree of flatness in the spectral range $425 - 525nm$.

5.4.2 Determination of the Short-Wavelength Side of the Spectrum

Nonsolitonic radiation is generated at a wavelength determined by the phase-matching condition (Fig. 14(b)). For a pump wavelength of $830nm$, the phase-matched nonsolitonic radiation is located at $\sim 550nm$. The generated dispersive waves in the visible propagate slower than the solitons in the infrared (Fig. 14(a)), which causes the both to separate in the subsequent evolution. Fig. 18 illustrates this stage of the supercontinuum generation process.

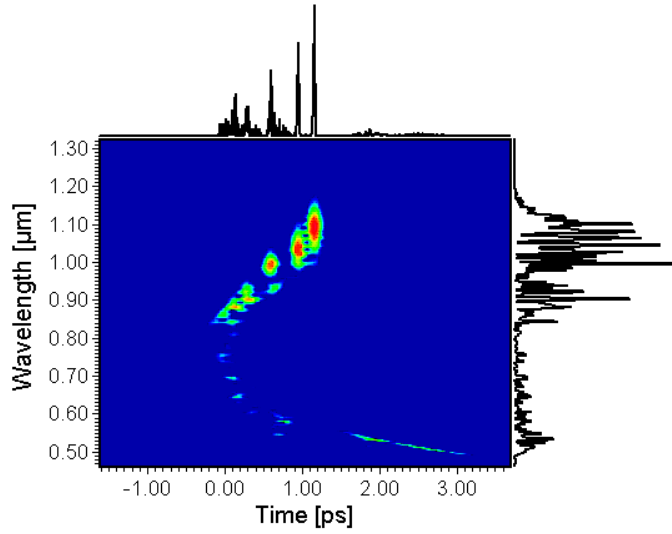


Figure 18: Simulated spectrogram of the initial stage of the process of supercontinuum generation ($z \sim 10\text{cm}$) using the MF 'crystal fibre NL-2.0-740'. The pump wavelength is at 830nm and the pulse energy is about 1nJ . The simulation uses T. Schreiber's implementation of the split-step Fourier method so as to solve Eq. (8).

With propagation the solitons experience the Raman-induced soliton self frequency shift. Consequently, the soliton group-velocity decreases. Fig. 14(a) shows the relative group-delay vs. wavelength ($\sim 40\text{ps/m}$ at $\lambda = 1500\text{nm}$). For the present fibre, the frequency shift due to the Raman effect is limited by the second zero-dispersion point in the infrared. Thus, the soliton is pinned to a certain wavelength ($\sim 1500\text{nm}$) and to a relative lower group-velocity with respect to the dispersive wave. Thus, in an terminal stage of supercontinuum generation this results in a progressive catching up of the soliton by the dispersive wave. When the soliton walks through the dispersive wave, the trailing edge of the soliton interacts with the leading edge of the dispersive wave and produces a positive chirp via cross-phase modulation. The interplay of XPM and normalous dispersion ('red faster than blue') causes blue-shifted components to be further transferred into the blue where the group-velocity is even lower than that of the Raman-shifted soliton. This allows the components to fall behind the soliton, i.e., they can escape even if the soliton completely walks through the dispersive wave [55,56].

Fig. 19 shows the XPM-induced blue shift in the process of supercontinuum generation using the MF 'crystal fibre NL-2.0-740'. The underlying model is a pump-probe

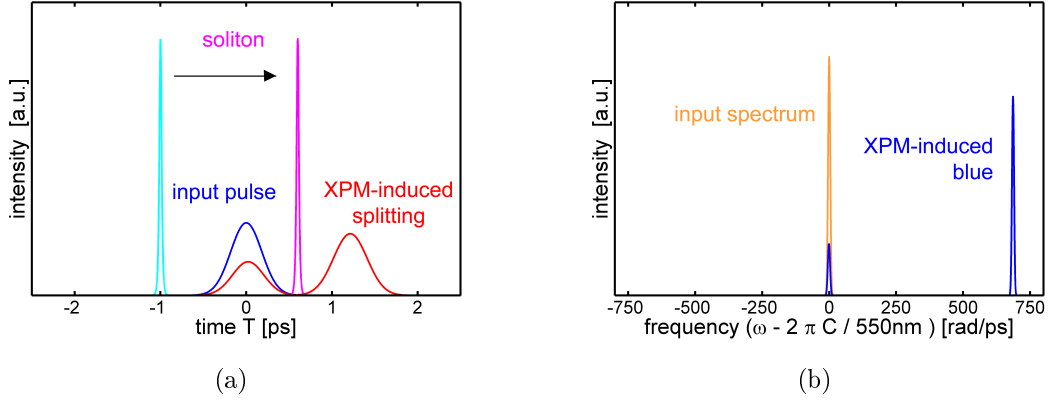


Figure 19: (a): Pulse vs. time (in a reference frame co-moving at the group-velocity of the dispersive wave). The cyan and magenta coloured peaks are the soliton before and after the interaction with the dispersive wave, respectively. (b): corresponding spectra of the probe

configuration [108] described by

$$\frac{\partial}{\partial z} A_1(z, T) + i \frac{\beta^{(2)}}{2} \frac{\partial^2}{\partial T^2} A_1(z, T) = i 2\gamma \left| A_2 \left(z, T - T_{\text{delay}} - \frac{z}{v_{G \text{ rel}}} \right) \right|^2 A_1(z, T). \quad (18)$$

Where A_1 is the probe (dispersive wave) and A_2 is the pump (soliton), T_{delay} is the initial delay, and $v_{G \text{ rel}}$ is the relative group-delay. The parameters for the simulation were extracted from the calculation shown in Fig. 18. My Matlab code is based on the split-step Fourier method in order to numerically solve Eq. (18). Such an approximated implementation is particularly useful as it allows to reveal the physics, and moreover, to localise the blue-shifted radiation on a second timescale whereas a complete simulation from the initial stage shown in Fig. 18 would take a few days while numerical instabilities are likely. The frequency shift shown in Fig. 19 is in accord with the experimental observation of wavelengths at $\sim 420\text{nm}$.

5.5 Relative Intensity Noise

To measure the intensity noise of the continuum, a silicium photodiode ('Thorlabs Inc. 201/579-7227') in combination with a fast oscilloscope was used. Fig. 20 illustrates qualitatively how an estimate for the noise can be extracted from the data. In particular, measurements have been undertaken for the input before the MF, the total output of the continuum after the MF, and the filtered output of the continuum after the MF. Integration over each pulse of a recorded pulse train (Fig. 20(a),(c),(e)) yields a distribution of the pulse areas. This can be visualised by histograms (Fig. 20(b),(d),(f)).

The ratio of standard deviation and mean value of the pulse areas results in a quantifier for the relative intensity noise. In the examples of Fig. 20, the MF 'crystal fibre NL-2.0-740' was pumped with pulsed light at $\lambda_{\text{pump}} = 830\text{nm}$. The average power before the fibre is 500mW . The corresponding supercontinuum spectrum is given in Fig. 17.

The broadening due to the response of the oscilloscope should not concern. In addition, the electronic noise is thought to be negligible compared to the impact of the fibre on the pulses.

The relative pulse-to-pulse noise was measured - according to the different spectra of Fig. 17 - at different pump wavelengths (from 710nm to 830nm in 30nm steps). The noise of the input is about $\sim 1\%$ and almost constant for the different wavelengths. This is in accord with the data provided from the laser manufacturer. Deviations from the given noise value may be attributed to non-polarisation-maintainance of the fibre which scrambles the initial linear polarisation state [109]. The pulse-to-pulse noise at the output including all spectral components (i.e., total output) is between 2% and 4% and increasing with pump wavelength. This tendency is shown in Fig. 21(a). In addition, the noise of the supercontinuum was measured behind bandpass filters. The result for a filter with a centre wavelength at 550nm is shown in Fig. 21(b).

In view of Fig. 17 and 21, it becomes apparent that the short wavelength side of the continuum can be extended to some degree by pumping further in the infrared but at the expense of rising noise levels. The increase in noise can be explained with the width of the frequency intervall between the pump and the blue components in the initial stage of the process of supercontinuum generation via soliton dynamics. In particular, the dispersive waves in the blue occur every time the soliton spectrum overlaps the resonant dispersive wave region [47]. Thus, a small variation in input pulse energy affects the extension as well as overlap in the blue. In addition, it translates to a considerable relative fluctuation in number of blue photons.

The scattering of the values shown in Fig. 21 may be due to insufficient warm up of the pump laser and stabilisation of the continuum (i.e., thermal settling down). In addition, the coupling had to be re-adjusted for each pump wavelength (at constant power level), and thus, conditions changed slightly. The noise level characterisation was also undertaken for another microstructured fibre ('crystal fibre NL-1.5-590') whereby attention was paid on avoidance of these errors, consequently, the results became more linear. The replacement of a dodgy coaxial cable - transferring the electric signal from

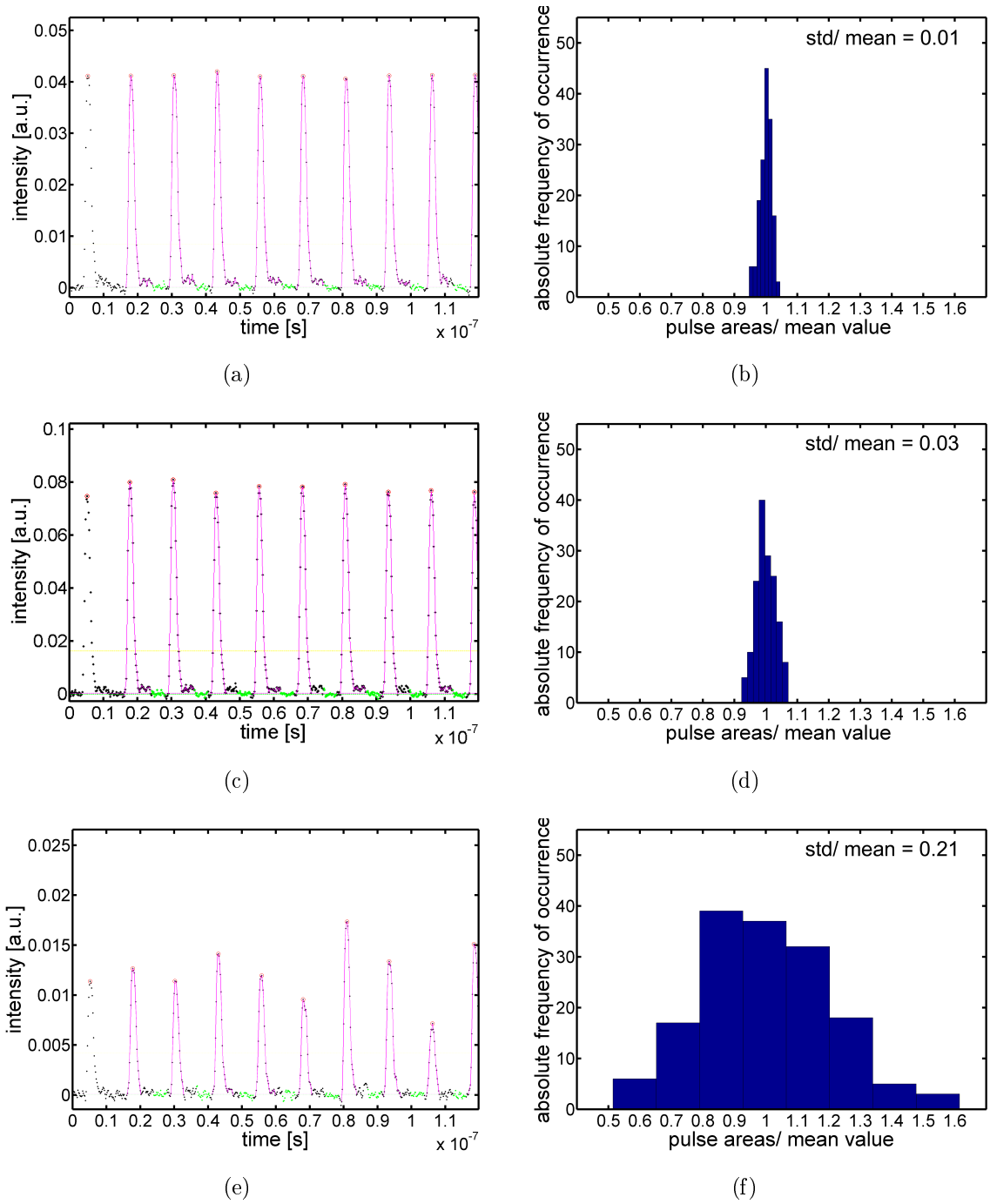


Figure 20: (a),(c), and (e) show sections from ca. 160 pulses recorded with a photodiode and an oscilloscope before the MF-input, behind the MF-output, and behind the filtered output ($\lambda = 500nm$, passband width $\sim 50nm$), respectively. (b),(d), and (f) show histograms for the pulse areas on the left. The ratio of standard deviation and mean of the pulse areas (std/mean) gives an estimate for the relative intensity noise.

the photodiode to the oscilloscope - improved the results significantly.

Although the 'crystal fibre NL·1.5·590' (ZDW at $590nm$) was not used in the following fluorescence microscopy, the spectrum allowed wavelength dependent noise measurements due to the possibility of scanning the supercontinuum with the the given set of interference filters (Fig. 22(b)). For this purpose the Ti:sapphire laser was set to $\lambda = 710nm$, which is the shortest wavelength available. Intensity noise vs. spectral range is shown in Fig. 22(a). In particular, this result states that the different spectral components contribute to noise differently. Research showed that a similar result can be found in Ref. [110].

Unfortunately, a similar spectral noise characterisation could not be undertaken for the continuum output of the MF 'crystal fibre NL·2.0·740' as the shape of the spectrum was not that suitable for scanning with the available set of interference filters.

While pulse-to-pulse fluctuations may be a problem for some applications, it is not an issue for steady state fluorescence intensity measurements or fluorescence lifetime imaging, due to the small number of fluorescence emission photons that are typically detected per pixel per excitation pulse. For instance, a standard confocal system (e.g., 'Leica TCS PS2' in combination with the inverted microscope frame 'Leica DMIRE 2') can scan at about 400 lines per second whereby a line consists of 256 pixels. This parallels to $\sim 10\mu s$ per point (which is equivalent to the pixel dwell time neglecting the dead time because of moving from one pixel to the next), in turn, this time interval corresponds to a number of 800 incident pulses at a laser repetition rate of $80MHz$. If one assumes about 20% fluctuation in pulse energy, 25 photons need to be detected per pulse per pixel in order to have an intensity noise contribution in excess of the shot noise (i.e., $20\% \times \text{photons} > \sqrt{\text{photons}} \Rightarrow \text{photons} > 25$). Consequently, 20% standard deviation in the source pulse energy would only be detectable above the shot noise for photon counts of greater than 2×10^4 photons per pixel [10]. In contrast, for fluorescence lifetime imaging using the combination of TCSPC and a confocal microscope the number of photons detected per pulse must be < 1 so as to avoid the pile-up effect. In addition to shot noise considerations, the intensity noise should not matter because of averaging during acquisition.

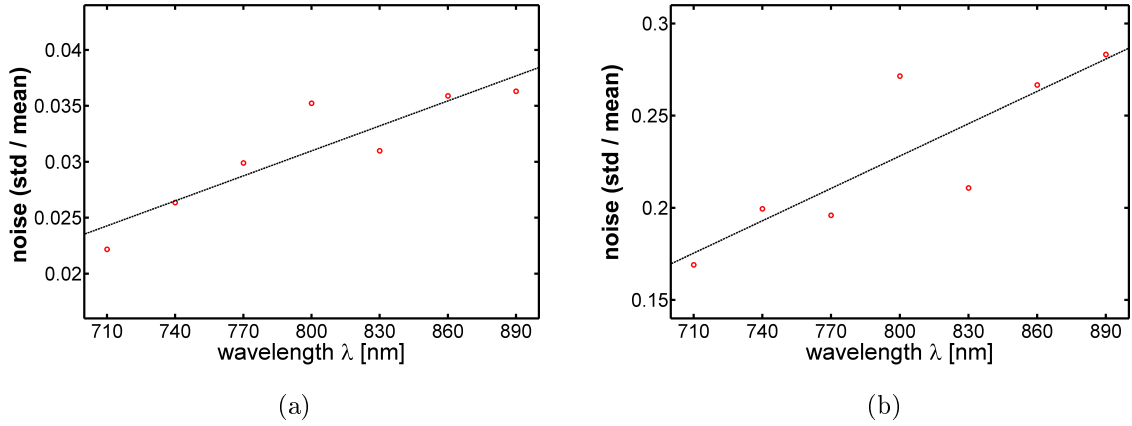


Figure 21: (a) noise of the total output vs. pump-wavelength (and linear least-squares-fit), (b) noise of the output behind an IF at 550nm vs. pump-wavelength (and linear least-squares-fit)

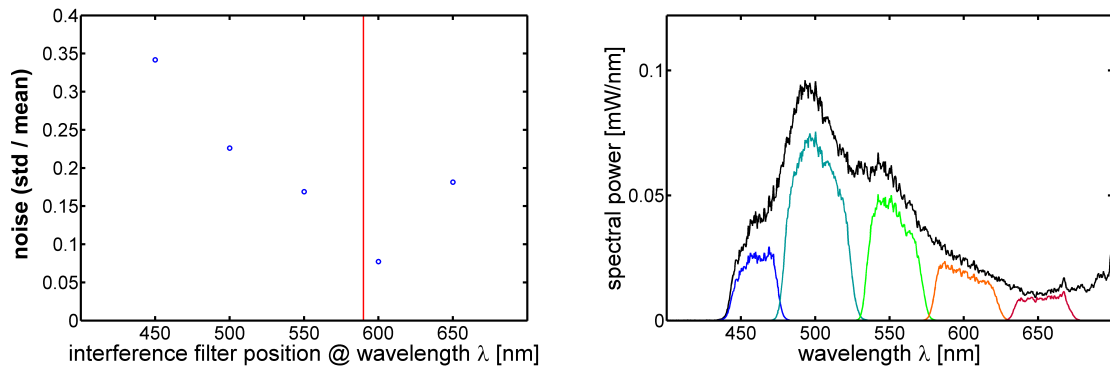


Figure 22: (a) wavelength dependency of the noise for the continuum output of 0.2m length of MF 'crystal fibre NL-1.5-590' (and linear least-squares-fit), (b) corresponding spectral sections and total spectrum for a pump wavelength of 710nm and input power of 500mW ((high) power transmission 0.17).

6 FLIM using the Tunable Continuum Source

This section provides a description of the application of the TCS to FLIM as well as spectral imaging. It is organised as follows. Section 6.1 deals with the experiment and the results of the application of the TCS to a wide-field optically-sectioned FLIM system based on Nipkow disk scanning. As Nipkow disk microscopy is a rapid wide-field technique, a fast time-gated intensifier can be used to carry out FLIM. Section 6.2 discusses the application of the TCS to confocal microscopy, and Although pixel by pixel scanning places limitations on the speed, it is a widespread tool which allows a high degree of optical sectioning while being comfortable to operate. FLIM is performed via time-correlated single-photon counting. In the latter experiments, the TCS rather acts as a means to transfer the infrared pump wavelengths to the blue spectral region. Although this is vitally important, the broad spectrum also provides multiple wavelengths for excitation of multiple labels and for complex fluorescence experiments – section 6.3 concerns spectrally and temporally resolved imaging. Section 6.4 concerns the application of an all-fibre source to wide-field FLIM. A low-cost table-top fully fibre-based system will be particularly suitable for real-world applications.

6.1 Wide-field Optically-Sectioned FLIM using a Nipkow disk

For some live cell imaging applications, fast single photon microscopy is more attractive than multiphoton microscopy providing that one can retain the advantages of optical sectioning and the ability to do FLIM that comes naturally with the ultrashort pulse excitation associated with multiphoton microscopy. This is because, it results in a lower instantaneous photon-flux per pixel, thereby reducing photobleaching and photodamage at the area of illumination compared to confocal microscopy.

This section is concerned with an optically sectioned live cell FLIM system based on the Nipkow disk microscope that incorporates a microlens array for higher throughput. This microscope requires spatially coherent laser excitation sources and this has previously constrained it to cw excitation at a limited number of fixed wavelengths (lines of the Argon and Krypton ion laser). The new tunable continuum source permits this approach to multidimensional microscopy to be implemented with excitation across the visible spectrum and to realise FLIM. As a rapid (wide-field) live cell imaging tool, it should be useful for cell-based screening for drug discovery. It will also be possible to simultaneously provide multiple wavelengths for excitation of multiple labels and for complex fluorescence experiments.

6.1.1 Experimental Setup

A schematic of the experimental set-up is shown in Fig. 23. It comprises a tunable continuum source (TCS), a Nipkow disk unit ('Perkin Elmer UltraView' formerly 'Yokogawa Electrical Corporation') attached to an inverted microscope frame ('Olympus IX71'), and the time-gated fluorescence lifetime measurement module ('Kentech Ltd.').

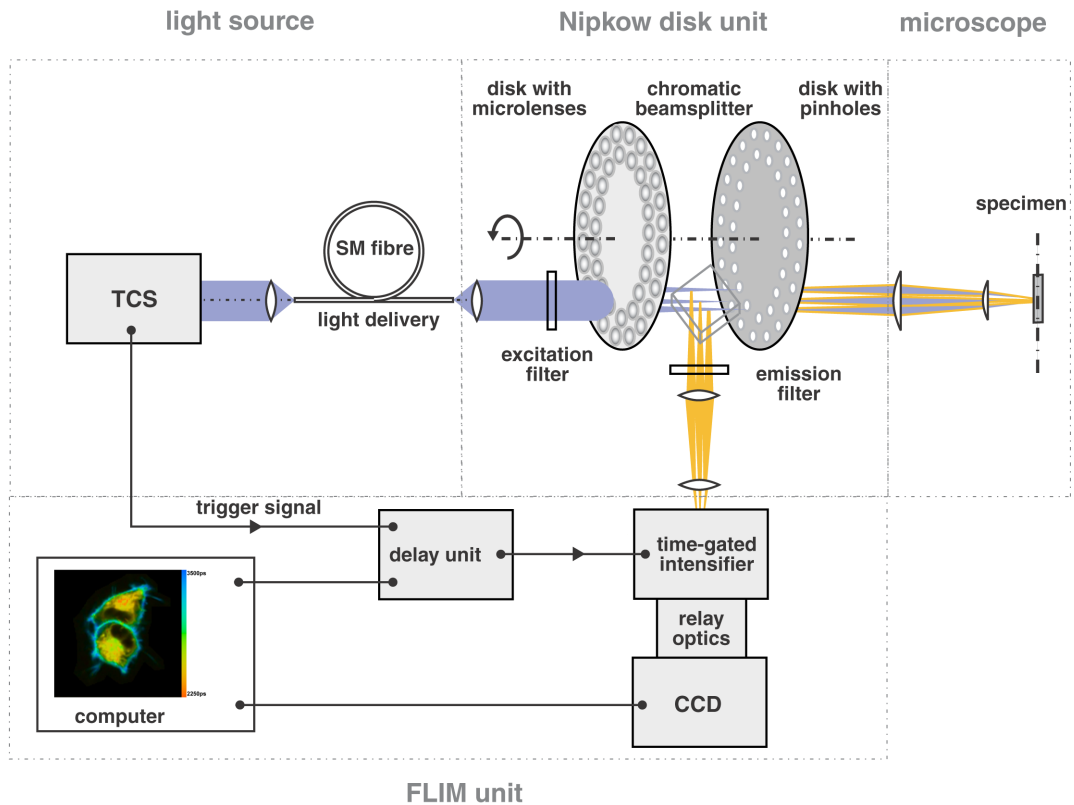


Figure 23: Schematic of the wide-field optically-sectioned FLIM using Nipkow disk scanning.

6.1.2 Spectrum of the Tunable Continuum Source

The set-up for the TCS is analogous to the one shown in Fig. 16: the output ($\lambda = 830nm$) of a Ti:sapphire laser is directed through an isolator and focussed by a $4.5mm$ focal length aspheric lens into a $0.7m$ length of MF ('crystal fibre NL-2.0-740'). The pump wavelength was chosen by means of Fig. 17. Thereby, the criteria were spectral flatness, laser properties (e.g., spectral mode-locking behaviour of the Ti:sapphire laser), and suitability for fluorescence microscopy (i.e., blue spectral region). A point

to note is that in the experiment the Ti:sapphire laser 'spectra physics Tsunami' was used instead of the 'spectra physics Mai-Tai'. According to the specification sheets of the two lasers, the laser output characteristics should be comparable. This can be qualitatively verified by comparing Fig. 24 with Fig. 17 – the both spectra (at $\lambda = 830nm$) exhibit identical features. Because of the change of laser type, a slight change in pulse duration is probably, however, this should not affect the spectrum that significant. In particular, detuning of the pump wavelength has a stronger impact on the continuum compared to the input pulse-width. This is due to a substantial variation of the dispersion profile [54]. The power at the fibre input is about $P = 550mW$. The continuum output was collimated using a x40 microscope objective. This spectrum was then modified by placing an interference filter in the beam so as to remove the transmitted infrared light before being launched into a single mode fibre for delivery to the Nipkow unit.

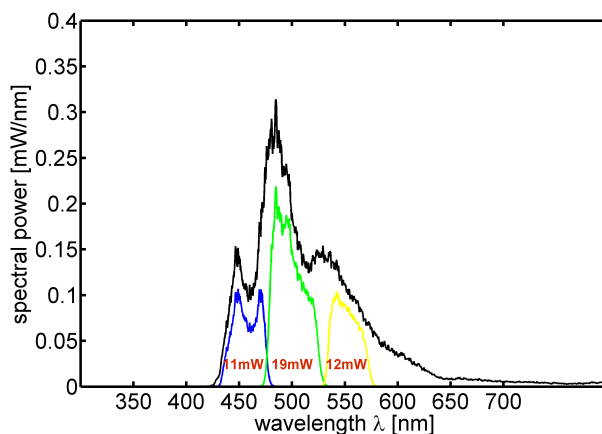


Figure 24: The short-wavelength side of the spectrum generated by means of pumping with the 'spectra physics tsunami' at a wavelength of $830nm$.

The excitation wavelength could be widely tuned depending on the particular fluorophore of interest, but was in practise limited by the chromatic beam-splitter and filters mounted inside the Nipkow disk unit. Yokogawa units are often equipped with multi-bandpass beam-splitters that have three passbands at $488nm$, $560nm$, and $610nm$, matched to the lines of Argon and Krypton ion lasers. In practice these wavelengths were convenient to use with the continuum source, and so samples could be excited at any of these wavelengths. However, since there are multiple transmission bands, the fluorescence is only reflected by the beam-splitter within $40nm$ of the excitation passband before reaching the next excitation passband. In principle, the

multi-bandpass chromatic beamsplitter could be replaced with a single cut-off mirror.

A typical spectrum prior to filtering, and the selected spectral bands with corresponding power values are shown in Fig. 24. It must be stressed that the shown profile is only the non-solitonic radiation of the overall spectrum (i.e., in the infrared there is the powerful solitonic part expected). Another point to note is that there exists no 'continuous' spectrum but a gap between the visible and infrared part of the total spectrum (on a linear intensity scale). This is in accord with theory. To fill the gap, I suggest to pump closer to the zero-dispersion wavelength with longer pulses, however, this in turn has a negative impact on the magnitude of the blue components.

In the experiments, the passband at a centre wavelength of $450nm$ was used. More generally, a spectral extension down to $350nm$ would be desirable for fluorescence imaging so as to cover the majority of absorption spectra on the short wavelength side. However, with the given microstructured fibre and pump laser available, it was not feasible to produce components below $420nm$ (on a linear intensity scale). Different types of fibres have been tried ('crystal fibre NL-1.5-590' with the tunable Ti:sapphire laser, 'blazephotonics SC-5.0-1040' with a Yb fibre-laser) but spectral components below this 'cut-off wavelength' could not be generated.

The power of about $11mW$ for the $450nm$ -passband must be seen as an initially optimized value because degradation during the experiments could be observed. In particular, the detuning of the coupling stage is likely to be the reason for this. In principle, the present coupling stage could be replaced by one with built-in feedback control (e.g., available from 'Thorlabs'). As a consequence, a more stable continuum should be achievable. This is of paramount importance since the time-scale of complex fluorescence experiments can not afford instabilities of the light source. Due to the damage threshold of the microstructured fibre tip at $\bar{P}_{in} \approx 600mW$ ($\Delta T_{in} = 100fs$ and $\nu_{laser} = 80MHz$), the power value of $11mW$ can not be simply increased by rising the magnitude of pump power. A larger area of the fibre core would be appropriate so as to reduce the damage threshold, and as a consequence, intensity could be increased. However, a modified core size will have a direct influence on dispersion via the waveguide contribution. Thus, a trade-off between dispersion and core-area needs to be found in order to increase the fraction of energy in the blue.

6.1.3 Specifications of the Nipkow Disk Unit

In the experiment, the Nipkow multi-spot scanner is the 'confocal scanning unit CSU 10' from 'Yokogawa'. Fig. 25 shows the schematic of the design. In this system a microlens disk (~ 20 thousand microlenses) is incorporated in addition to the regular Nipkow disk [77]. Owing to the light concentration via this array of microlenses, transmission through the two disks is improved up to about 40% [77, 111].

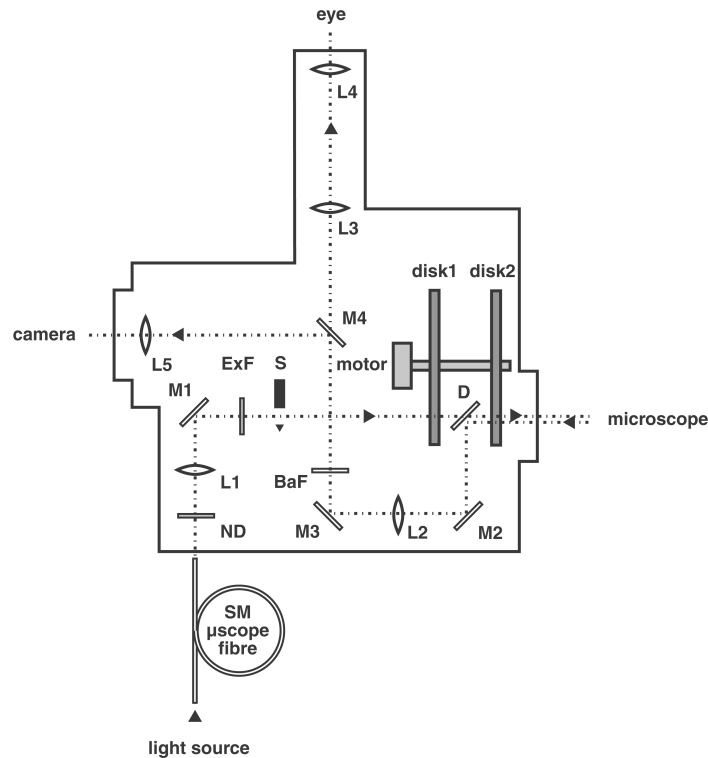


Figure 25: Light path in the CSU10 (after Ref. [111]).

Light from the tunable continuum source is introduced into the CSU10 through a single mode optical fibre (SM μ scope fibre) with a core-diameter of about $4\mu m$, collimated by a collimator lens (L1), pass a neutral density (ND) filter, an excitation filter (ExF) and then illuminate a microlens array (disk1). Whereby the single beam of light is expanded to fill a part of the area of the disk, and passes through the apertures of the microlenses, producing multiple beams. About 1000 laser beams focussed by the microlenses pass through a chromatic beam-splitter (D) (area: $7mm \times 10mm$) onto the corresponding pinholes ($50\mu m$ diameter). The passing light is focussed onto the specimen plane by the microscope objective in order to excite fluorophores. The fluorescent light emanating from each spot of the specimen returns along the same path

from where it came through the objective lens, sharpened again by passing through the pinholes, reflected by the chromatic beam-splitter, and passes barrier filters (BaF) to reduce the noise of excitation laser beam, finally focused (L3, L4) on to the image plane of eyepiece lens or camera by relay lens (L5) as a sectioned wide-field image [111]. Rotation speed of the scanner motor is about 30rps. The pinhole pattern produces 12 frames per rotation, giving up to 360 frames per second of wide-field optically sectioned images. Various chromatic beamsplitters can be inserted between the microlens and pinhole disks depending on the excitation wavelengths and the unit also incorporated additional excitation and emission filters. The output light field could be detected either with a CCD camera, or using a gated optical intensifier (GOI) for performing fluorescence lifetime imaging (FLIM).

6.1.4 Time-Gated FLIM Unit

A schematic of the FLIM unit applied to the Nipkow disk unit is shown in Fig. 23. Fluorescence light emanating from the sample is imaged onto a wide-field time-gated optical intensifier ('GOI'/'HRI' manufactured by 'Kentech Instruments Ltd.')

 [112], which is made up of an photocathode, which generates photoelectrons, and a phosphor screen sandwiching a double microchannel plate. To compensate for the reduction in spatial resolution, a double, rather than single, microchannel plate is used. All other light sources should be excluded from the photocathode by using a black tube.

The microchannel plate of the time-gated optical intensifier comprises an array of coated glass capillaries of a few micrometers diameter. It provides short gate times of ≤ 500 ps FWHM over an 18mm diameter cathode aperture. The wafer type design gives a large number of pixels across the full 18mm diameter cathodes. The resolution is typically 10 *lppmm*⁻¹ (*lppmm* = line pairs per millimetre, in other words, this unit tells how many elements there are per *mm* on the detector plane) dropping at the shortest gate durations. The capillaries are set at an angle (typically 15°) to the incident photoelectrons. A secondary electron cascade is produced upon collision of the electrons and the capillary. The divergence of the initiated electrons decreases as the electron energy increases. The signal gain can be varied by applying a voltage to the microchannel plate in the range 500 – 1600V. The time-gated optical intensifier has a modulation bandwidth of 1GHz and can provide impulse gating with sub nanosecond gate widths at repetition rates in excess of 100MHz. The intensifier gating and gain modulation is provided by switching the photocathode potential with respect to the microchannel plate input, which is at ground potential. The intensified image on

the phosphor screen is relayed to a CCD camera by two camera lenses front-to-front; an inexpensive and light efficient alternative to a field lens [84]. A CCD camera ('Hamamatsu ORCA-ER') is set up to view the output of the gated optical intensifier. The 'Kentech trigger delay unit' is used for trigger delay control. One may simply delay the low level input trigger signal feeding the front panel trigger input by connecting it via a 'Kentech precision programmable delay line' [113]. The delay line provides 20ns of adjustment in 25ps steps and may be used at trigger rates > 100MHz. As a consequence, the time-gate can be delayed with relation to the laser pulses at a certain repetition rate.

6.1.5 Acquired Lifetime Maps

Below FLIM maps of samples of stained mouse embryo sections (prepared from lymph nodes of different mouse lines) are shown. The integrated fluorescence intensity is shown on the left hand side. It can be interpreted as a photon number distribution. On the right, the lifetime maps are merged with the intensity images so as to form a weighted functional FLIM map. The sectioned images display improved image quality and contrast compared to their conventional counterparts.

In conclusion, this approach has the potential to acquire optically-sectioned FLIM images at higher frame rates than scanning confocal microscopy. The TCS addresses one of the key drawbacks of the Nipkow disk microscope, namely, the limited availability of spatially coherent pulsed excitation sources in the visible spectral range so as to carry out FLIM. It must be stressed that a FLIM experiment using the Nipkow disk and the novel TCS has been undertaken for the first time. Consequently, emphasis was placed on demonstration of such a system, finding of possible pitfalls and potential improvements. For instance, further development of the TCS in terms of stability and spectral coverage is definitely necessary. However, this requires additional equipment (e.g., different types of fibres and a new fibre coupling approach).

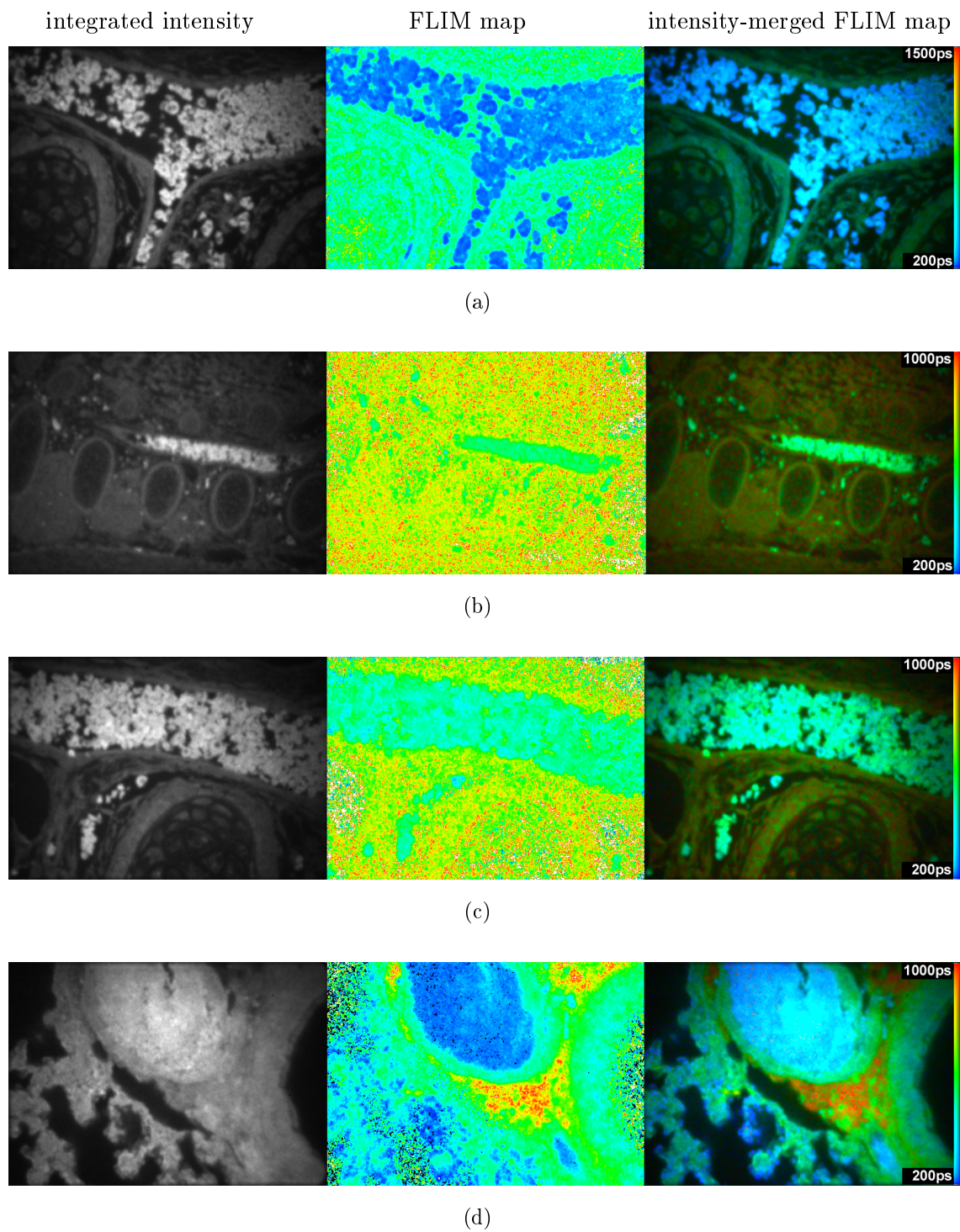


Figure 26: (a): Tissue stained with troma- (magnification (M) $\times 40$). (b),(c): Tissue stained with ttf- (M $\times 10$) and (M $\times 40$). (d): Lung-tissue ($30\mu\text{m}$) (M $\times 40$). Excitation wavelength at 450nm .

6.2 Time-Correlated Single Photon Counting

As time-correlated single photon counting (TCSPC) requires a confocal microscope, the application of the spatially coherent supercontinuum source is convenient as it provides a point-like source able to tune across the visible.

6.2.1 Experimental Setup

In the experiment the TCS consists of the set-up of the previous sections (Fig. 16). The pump laser wavelength is chosen to be 830nm (at a pulse duration of $\sim 100\text{fs}$ and an average power of $\sim 0.5\text{W}$). The low power transmission of the MF is $\sim 40\%$. The resultant supercontinuum section is identical to the one shown in Fig. 24.

An interference filter with a passband of 50nm centered at 450nm ('comar 450 IU 25 T-EMB') serves as a wavelength pre-selection. Its average transmission is about 65%. Instead of using an interference filter a prism-monochromator could have been used (appendix A). For sake of simplicity and because of the polarisation sensitivity of the (uncoated) prism monochromator, the use of the interference filter was favoured. Particularly, when not employing a PM microstructured fibre for supercontinuum generation and having an uncoated prism, an interference filter wheel may be the better option.

The power behind the filter is about 10mW . The pulsed beam passes a shutter (which serves as an overload protection for the photomultiplier tube [114]) and a neutral density filter wheel so as to attenuate the power in order to avoid photobleaching of the living cells. Finally, the beam was launched into the confocal microscope ('Leica TCS PS2' in combination with the inverted microscope frame 'Leica DMIRE 2'). The fluorescence emanating from the sample was detected with the photomultiplier tube 'Becker & Hickl PMH 100-1'. The photomultiplier tube is connected with the TCSPC computer-card ('Becker & Hickl') and another output feeds the overload protection system.

6.2.2 Specifications of the Counting Card

The method of TCSPC was described in the section 3.3.4. A schematic of the 'Becker & Hickl' counting card is shown in Fig. 27. At this point it is appropriate to describe the design in more detail.

An important feature of TCSPC is the use of the rising edge of the photoelectron pulse for timing the time-to-amplitude converter [68]. This allows phototubes with

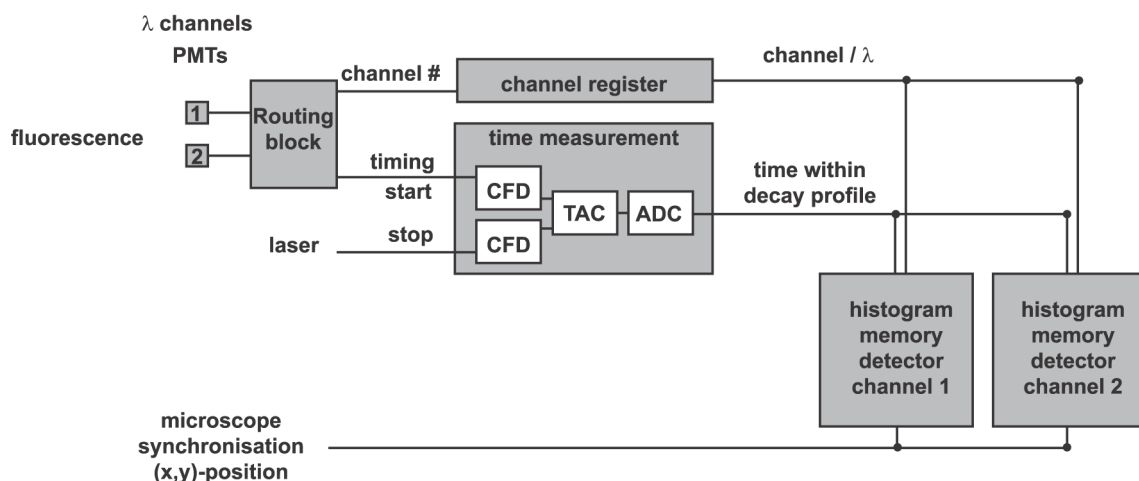


Figure 27: Dual wavelength channel TCSPC (reverse mode operation) after Ref. [94]. TAC: time-to-amplitude converter, PMT: photomultiplier tube, ADC: analog to digital converter, CFD: constant fraction discriminators

nanosecond pulse widths to provide subnanosecond resolution. Thus, among the most important parts of the TCSPC electronics are the constant fraction discriminators, which provide improved time resolution by removing the variability due to the amplitude of each voltage pulse [68].

In TCSPC the most critical component for timing is the photon detector [68]. The detector of choice is a multi-channel plate (MCP) in conjunction with a photomultiplier tube. It provides short electrical pulse widths and exhibits lower intensity after-pulses. The time resolution of the TCSPC technique is given by the transit time spread in the detector, which is 150 ps for fast conventional photomultiplier tubes ('Hamamatsu H5773P') and 25 to 30 ps for the combination of multi-channel plates and photomultiplier tubes ('Hamamatsu R3809U-50'). In conjunction with a minimal time channel width of the TCSPC modules much shorter lifetimes (a few ps) can be determined by deconvolution of the recorded decay data [94].

A source of error in TCSPC is the detection of several photons per laser period. This results in decay curve distortion or pile-up effect [68]. Therefore, the count rate should be much smaller than the laser pulse repetition rate so that the detection of several photons per laser period can be neglected. Although the pile-up effect is predictable, a recorded photon count rate of 5% of the laser repetition rate should not be exceeded [94].

In one part of the experiment two wavelength channels were used. This is simply realised by using a chromatic beamsplitter behind the output of the microscope and

two photomultiplier tubes. The schematic of Fig. 27 shows the following configuration of the 'Becker& Hickl' counting system. The routing technique makes use of the fact that the detection of several photons in different detector channels in the same laser period is unlikely. Therefore, the single-photon pulses from all detector channels can be combined into the common photon pulse line and sent through the normal time measurement procedure of the TCSPC module [114]. As a consequence, fluorescence photon distribution vs. time, spatial coordinates, and wavelength builds up. In particular, a two channel configuration may be useful for determining Förster resonance energy transfer.

6.2.3 Application

In the first part of the TCSPC experiment only one photomultiplier tube was used. The chromatic beamsplitter inside the confocal microscope is a longpass 480. Directly before the detector there is another HQ longpass 500 (emission filter).

One example of a FLIM image for COS cells (monkey kidney cells) expressing cyan fluorescent protein (CFP) is shown in Fig. 28. CFP has its main absorption peak at about 440nm and its principal emission peak at about 475nm . Thus, the spectrum of the TCS (Fig. 24) is convenient to use with the given chromophore. FLIM data processing was performed using SPCImage software ('Becker&Hickl GmbH'). In particular, single exponential decay profiles were fitted onto the acquired data. The resulting false-colour lifetime map is merged with the integrated fluorescence intensity image to aid visualization.

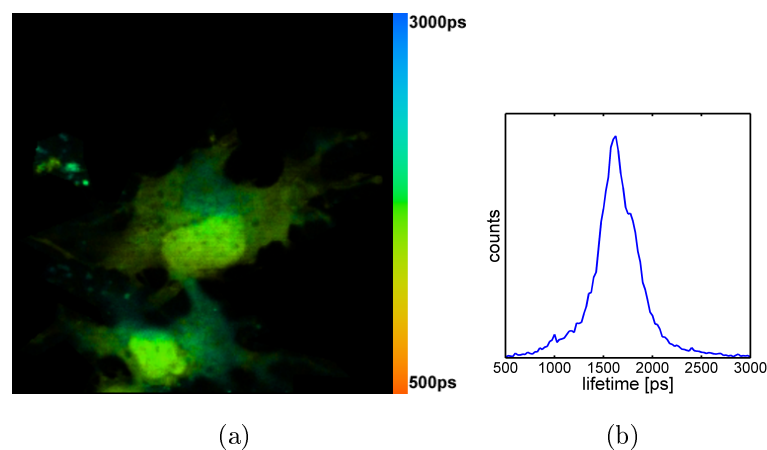


Figure 28: COS cell stained with CFP. (a): intensity-merged FLIM map (b): corresponding lifetime histogram.

The genetically expressed fluorescent probe CFP is a mutant spectral variant of the so-called green fluorescent protein (GFP) - extracted from the jellyfish *Aequorea victoria* - which altered cell biology research dramatically by opening the door to non-invasive fluorescence multi-colour investigations of subcellular protein localisation, intermolecular interactions, and trafficking using living cell cultures [115]. Used in combination with GFP, this fluorescent protein is useful in Förster resonance energy transfer (FRET) experiments and other investigations that rely on multicolor fluorescence imaging. Other fluorescent proteins such as YFP, EFP, DsRed and HcRed are promising candidates for investigations with longer wavelengths of the visible spectrum, moreover, they are convenient to use with the novel TCS. Particularly for these increasingly popular multi-labelling applications using fluorescent proteins, the TCS is especially suited.

For the dual channel FLIM experiment, a longpass ($560nm$) provides two wavelength channels serving the two photomultiplier tubes. This configuration is attached at the fluorescence output of the confocal microscope. Directly before the photomultiplier tubes there are additional filters (bandpass $500 - 530nm$ and a longpass $570nm$) for further spectral discrimination. Inside the confocal microscope, a longpass $480nm$ is used again as the chromatic excitation-emission-beamsplitter.

With this set-up HEK (human embryonic kidney) cells are studied. The HEK cells are stained with the membrane-sensitive dye di-4-ANEPPDHQ ('Molecular Probes'), which differentiates liquid-ordered phases from -disordered phases. The properties of the dye were studied in model membranes [116]. It could be shown that the fluorescence emission maximum of the dye is at a wavelength of $570nm$ in liquid-ordered phase compared with $630nm$ in the disordered phases. This is shown in Fig. 29. Consequently, with the filter combination above there is an imbalance in terms of number of photons in the two channels. It is important to note that this filter combination served for a different biological experiment.

Although right dual channel TCSPC FLIM would have been better, the reasonable amount of photons in one channel allows FLIM to be undertaken, in addition, it is a good way to illustrate what information is obtainable from standard TCSPC FLIM compared with spectral imaging. Fig. 30 shows that the fluorescence lifetime map exhibits a stark contrast. Here, only the second channel is shown since the lack of photons did not allow fitting for the first one.

In particular, the ability of the dye to detect both phases may be important in biophysical research studies concerned with lipid domains in cell membranes. Notably, the

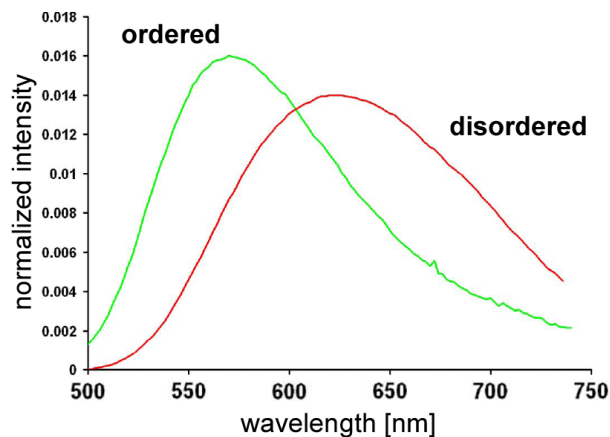


Figure 29: Emission spectra with 475nm excitation light of di-4-ANEPPDHQ in ordered and disordered phase in model membranes taken from Ref. [116].

concept of lipid domains, or rafts, as organising centres for localized signalling pathways in membranes has achieved significance in fundamental cell biology research. Membrane studies of coexisting lipid phases help provide a biophysical basis for these phenomena.

In addition, information from pure spectral intensity imaging was obtained by forming the ratio of the total emission of the two fluorescence channels (i.e., temporally integrated). The resultant image can be seen in Fig. 31(c). Here, the membrane of the cell is a region where the liquid-ordered phase-state is primarily favoured compared with the other state ($I_1(i, j) > I_2(i, j)$). It is insightful to compare the information from spectral intensity imaging (Fig.31(c)) with the single channel FLIM map (Fig. 28(a)). It can be clearly seen that the information of the different approaches correlates to each other. It must be stressed that spectral intensity imaging is faster than fluorescence lifetime imaging for most imaging modalities. In addition it is less expensive. Although spectral intensity imaging does not provide the same amount of information (e.g., about the fluorophore environment) compared to FLIM, it may be a practical alternative for some application (like the one presented here). Combined with the TCS, this approach permits the recording of a excitation-emission matrix, which in turn, offers the possibility to localise fluorophores within multiple stained biological tissue. It may also be a convenient and fast approach for the determination of FRET.

It is clear that for real dual channel spectral FLIM the right chromatic beamsplitter with a separation wavelength in between the two emission maxima would have been

better (compare Fig. 29). However, in this case, crosstalk ('bleed through') between the channels is still a problem since the emission spectra of the two phases are not distinct. For spectral imaging, this can be overcome via a linear unmixing algorithm. Using this method it would be possible to ascertain the specific emission of the different (states of) fluorophores to the total signal and to restore a clear signal for each colour channel, unaffected by emission from the other fluorophore [117].

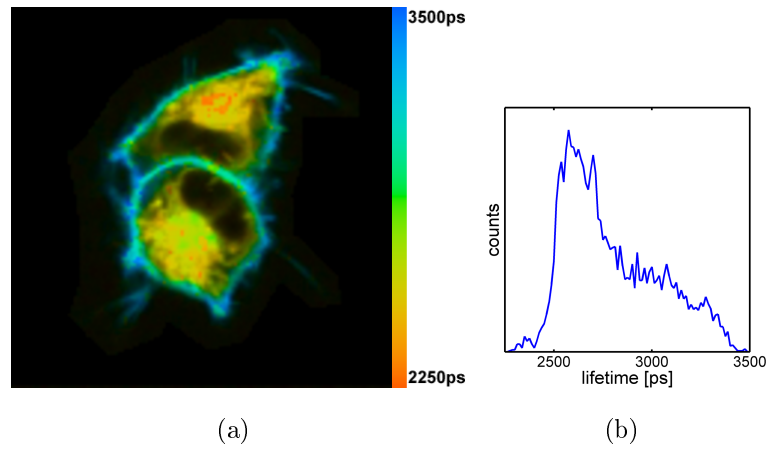


Figure 30: HEK (human embryonic kidney) cells stained with di-4-ANEPPDHQ (2nd channel) (a): intensity-merged FLIM map, (b): corresponding lifetime histogram.

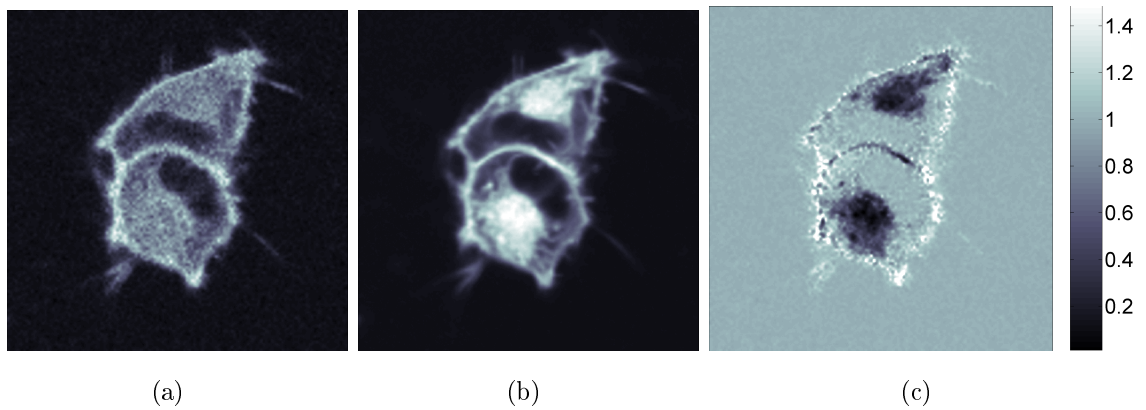


Figure 31: (a) and (b): (normalised) intensity images $I_1(m,n)$ and $I_2(m,n)$ of channel 1 and 2, respectively. Where (m,n) are the pixel-indices. (c): ratio $(max - I_2(m,n)) / (max - I_1(m,n))$, where max is the peak-intensity of both $I_1(m,n)$ and $I_2(m,n)$.

6.3 Spectrally and Temporally Resolved Imaging

Fluorescence lifetime imaging can be combined with spectroscopy to allow spectrally and temporally resolved imaging. As a consequence, more information can be gathered from fluorescence emission. Experimental ambiguity can also be removed since changes of fluorescence are often observable by spectral imaging as well as fluorescence lifetime imaging. In particular, multiple fluorophores may be identified using this method. This may be important when capturing the biochemical content of cells.

In the experiment, line-illumination and stage-scanning of the sample is employed. Each line is spectrally resolved using a spectrograph, in addition, it is also temporally resolved using a time-gated intensifier.

Pure spectral imaging combines conventional imaging with spectroscopy. Traditionally, spectral images were acquired using a CCD detector through a series of dielectric filters. To avoid drawbacks associated with the use of these elements, a spectrograph (equivalent to a dispersing element and CCD camera) is used in the experiment; it collects the entire emission spectrum in one run and single pass. The spectrograph is calibrated by replacing the specimen with a mirror, and then, reflecting a number of known excitation wavelengths into the spectrograph.

Supercontinuum generation in microstructured fibre is especially suited to meet spectral imaging. It provides a broad spectral coverage of wavelengths for sequential or simultaneous excitation of fluorophores. Particularly, the excitation wavelength can be tuned so that only one of the multiple fluorophores absorbs. Thus, detailed localisation of biochemical components within biological tissue is feasible. Furthermore, the spatially coherent broadband fibre-source effectively utilizes the slit aperture (section 3.2.5).

6.3.1 Experimental Setup

The broad continuum is generated by launching of femtosecond pulses ($80fs$) from the Ti:sapphire laser 'spectra physics Hurricane' (at $\lambda = 800nm$ and a repetition rate of 80MHz) into 0.3m length of highly nonlinear microstructured fibre 'crystal fibre NL-2.0-740'.

The collimated output of the supercontinuum is introduced into the excitation prism-monochromator (appendix A) in order to select portions of the continuum. One feature of this 'spectral discriminator' is that it allows to select spectrally distinct parts of the

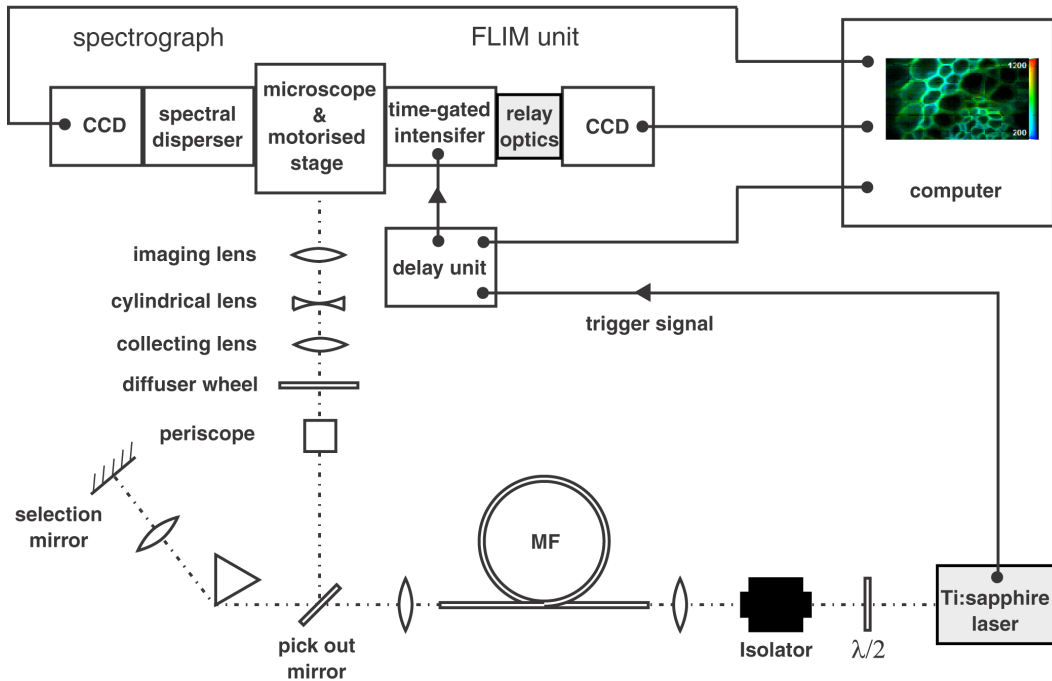


Figure 32: Schematic of the experimental setup for spectrally and temporally resolved imaging.

continuum simultaneously. Potentially, it can be conveniently controlled using spatial light modulator technology. However, in the experiment the wavelengths 480nm , 545nm , and 570nm were chosen via mechanical control (appendix A). The passband has a spectral width of $\sim 10\text{nm}$.

The recording of speckle is avoided by placing a spinning diffuser wheel into the beam-path. The deviated light is gathered by a collector lens and focussed to a line onto the specimen plane by the combination of a cylindrical lens, standard imaging lenses, and the objective ('Olympus x40, NA 0.75 dry').

The emitted fluorescence returns along the direction from where it came, and is reflected by the chromatic beam-splitter. Firstly, the fluorescent line is spectrally resolved by an imaging spectrograph, which has a spectral range of 373nm to 1133nm . Sampling takes place every 3nm , and the wavelength resolution is 9nm . Secondly, the fluorescence emission is temporally resolved by means of a time-gated intensifier. The acquisition is based on the 3-gate rapid lifetime determination method of section 3.3.3.

6.3.2 Application

The test sample is a $15\mu\text{m}$ transverse section of the rhizome of a Lily of the Valley (*convallaria*) that had the conjunctive tissue and phloem stained with Fast Green and the xylem stained with both Safranin O and Fast Green. These dyes are commonly used to stain biological specimens, in particular, for photomicrography. Their absorption spectra are shown in Fig. 33. The sample was provided by Johannes Lieder, Ludwigsburg, Germany.

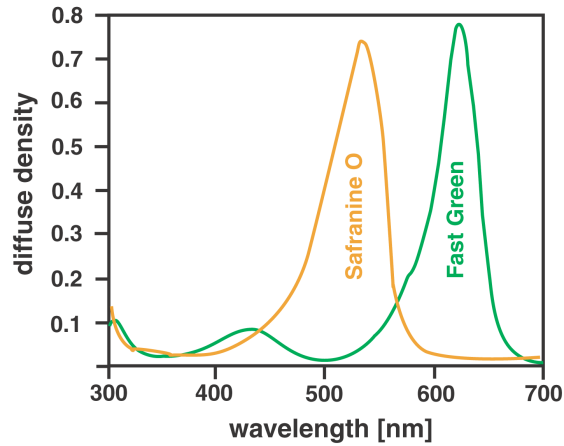


Figure 33: Visible absorption spectrum of the dyes Safranin O and Fast Green (taken from Ref. [118]).

The acquired images cover an area of $105\mu\text{m} \times 60\mu\text{m}$ with a resolution of $\sim 1\mu\text{m}$. The sectioning strength is about $7.5\mu\text{m}$. The acquisition time for each spectrally and temporally resolved line is 9 to 27s. This is mainly due to the integration time so as to obtain a reasonable amount of photons. The images shown cover 60 lines; thus, it takes 9 to 27min in order to capture a single image. Because of the acquisition on a minute-timescale, the stability of the fibre-coupling into a 2-micron core is a limiting factor. Particularly, it could be seen that it is vibration-sensitive.

The temporally resolved images (FLIM maps) of different emission windows for the three excitation wavelengths are shown in Table 1. It is clear that the absorption characteristics of the two dyes have a direct impact on the observable emission at different excitation wavelengths. Particularly, the limited spectral absorption range of Safranin O plays a role here. For the excitation wavelength of 488nm , it should be solely excited. The first row of Table 1 indicates the presence of Safranin O.

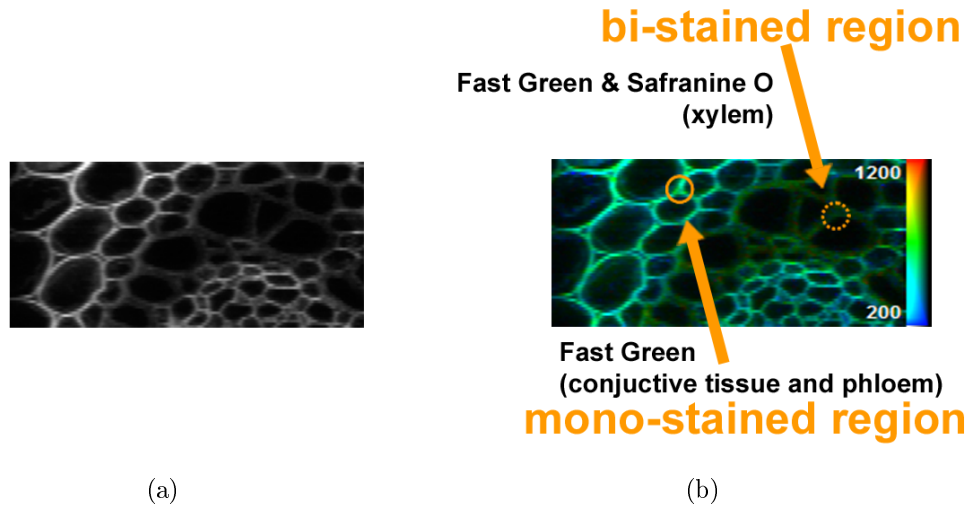


Figure 34: (a) intensity image (i.e., integrated fluorescence emission) (b) functional image (FLIM map of the sample *convallaria*) which allows localisation of the mono- and bi-stained region. The selections within these regions (shown via circles) are used for data analysis.

The localisation within a restricted area can be traced back to the fact that only the xylem is stained with Safranin O whereas Fast Green should be found all-over. The column on the right hand side shows the reciprocal of the heterogeneity ($1/h$) versus excitation wavelength (for the definition of h see section 3.3.2). The field of view is turned by 90 degrees. As just one of both dyes is preferentially excited, the reciprocal of the heterogeneity is closer to 1 on the whole sample. The heterogeneity parameter allows quantitative localisation of regions where both dyes are present (blue labeled). The vanishing heterogeneity with increasing excitation wavelength may also be considered as a proof for the limited excitability of Safranin O. In view of the sample heterogeneity, the fluorescence information of the first element of Table 1 (i.e., 480nm excitation, 490-620nm emission window) may be exclusively due to Safranin O.

To analyse the data, particularly, in terms of spectral properties, a mono- and bi-stained region was selected. Thereby, the information provided by Table 1 was used. The sections are shown in Fig. 34(b).

For the bi-stained region of *convallaria*, Fig. 35(b) illustrates the change in lifetime and peak-emission when varying the excitation wavelength. Again, this tendency can be explained with the absorption spectra of the two stains. For the excitation wavelength of 480nm the dye Safranin O (major absorption from 470 to 550nm) is expected to govern both lifetime and peak-emission wavelength, whereas for an excitation of 570nm the stain Fast Green (major absorption for wavelengths $> 560nm$) is supposed

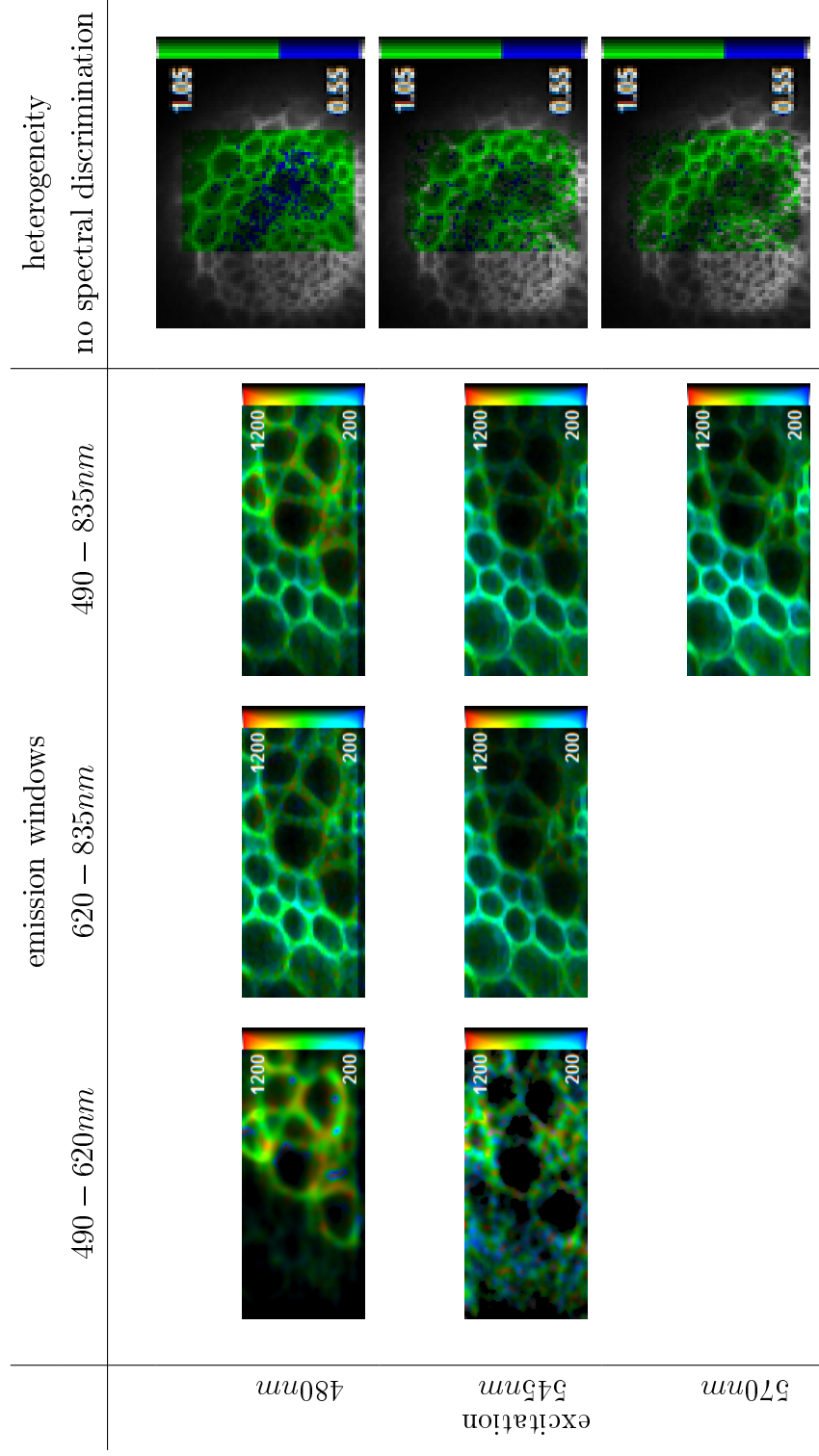


Table 1: Fluorescence lifetime maps of emission windows vs. excitation wavelengths, and heterogeneity vs. excitation wavelength (test sample 'Lily of the Valley').

to dominate these characteristics. The values at an excitation wavelength of 545nm are rather due to an intermediate state, where both dyes contribute to fluorescence emission (compare also heterogeneity column of Table 1). It is worth mentioning that both lifetime and peak-wavelength exhibit a significant shift.

In view of these results, it must be stressed that the tunability of the supercontinuum source across the visible is an important tool for spectral discrimination of dyes within multiple stained tissue. In particular, the choice of fluorophores for spectral imaging does not rely on the source. However, a precondition of spectral imaging is the spectral distinctness of absorption ranges of the fluorophores. Usually, it is quite easy to fulfil this requirement as there are plenty of fluorophores with well-known absorption spectra available.

Fig. 35(a) shows the averaged emission spectrum of the bi-stained region at an excitation wavelength of 488nm . Keeping the absorption of the dyes in mind, the spectral emission range may be divided into three windows (490 to 550nm , 550 to 620nm , and 620 to 835nm). It can be seen that the different spectral components possess different lifetimes. Without varying the excitation wavelength, spectrally and temporally resolved fluorescence emission may reveal the presence of different dyes. This is because, the different fluorescent components emit in different spectral regions, and in addition, the corresponding lifetimes should exhibit differences, too.

For the dye Fast Green, Fig. 36 illustrates the shift in emission spectrum and lifetimes owing to the situation in either the xylem (stained with Fast Green and Safranin O) or in the conjunctive tissue (only stained with Fast Green). The fluorescence emission of Fast Green in the conjunctive tissue (blue) shows the same lifetime irrespective of excitation wavelength ($\sim 560\text{ps}$). This is due to the fact that this region has been stained with Fast Green solely. When studying the (extracted) emission of Fast Green from the xylem (in the spectral emission window from 620 to 835nm), the decay shows a shift in lifetime and spectrum with respect to the emission from the conjunctive tissue, even though it is the same dye. This may be attributed to the impact of the xylem environment (Safranin O) on the emission of Fast Green.

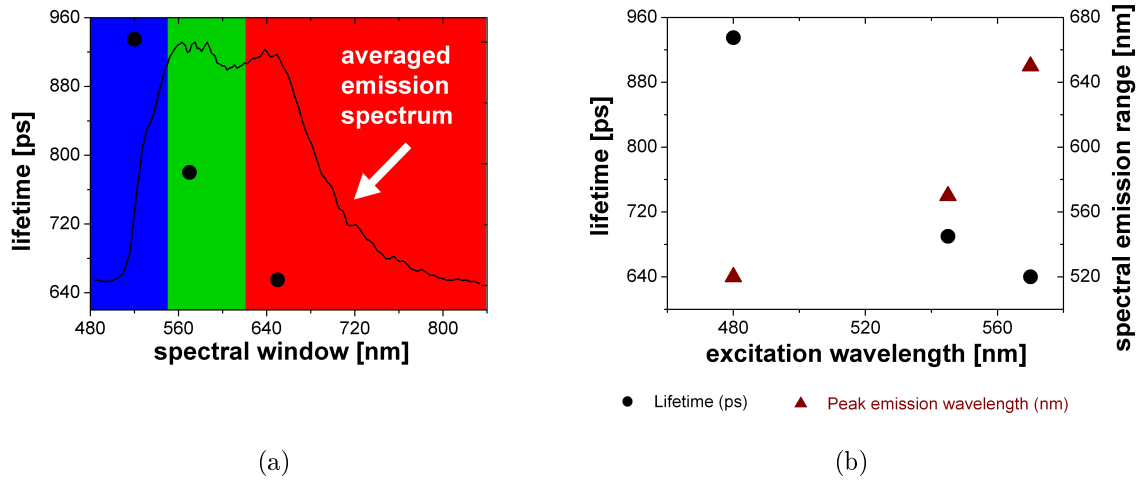


Figure 35: (a) averaged fluorescence emission spectrum of the bi-stained region at an excitation wavelength of 480nm . The emission is divided into spectral windows, and for each section, lifetime values are obtained. (b) lifetime (\bullet) and peak-emission wavelength (Δ) versus excitation wavelength corresponding to the different excitation wavelengths in the bi-stained region

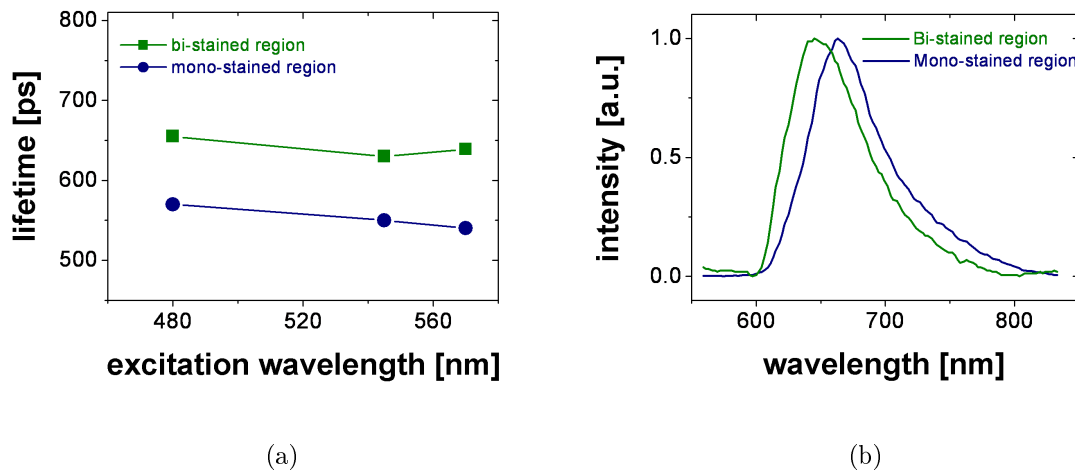


Figure 36: (a) Lifetime vs. excitation for Fast Green alone (blue) and in presence of Safranin O (green), (b) emission intensity vs. wavelength for Fast Green on its own (blue) and in presence of Safranin O (green), in both cases is the excitation wavelength 570nm and the spectral window $620\text{-}835\text{nm}$.

6.4 Wide-field FLIM

This section concerns the combination of fibre-laser pumped supercontinuum generation in microstructured fibre and a wide-field FLIM system. In the other sections dealing with the application of supercontinuum to FLIM, a tunable Ti:sapphire laser is used for pumping the microstructured fibre. At present, the Ti:sapphire laser has superior output characteristics compared with other commercially available types of lasers, however, supercontinuum generation via microstructured fibre does not require a tunable source for pumping. The wavelength of the pump-source only has to match the dispersion profile of the fibre. Thus, a less complex laser - exhibiting good characteristics - should be the starting point. Following this, the right MF - which meets the pump laser - needs to be chosen (or especially designed).

Consequently, the motivation for using a fibre laser and microstructured fibre was to demonstrate a potential table-top tunable light-source for fluorescence lifetime imaging. The cost of this technology is likely to drop significantly once fully fibre-based systems have been developed. Such systems will be particularly suitable for real-world applications.

6.4.1 Experimental Setup

The TCS is made up of a commercially available all-fibre platform comprising an amplified seed oscillator ('IPG YLP-8-1060-PS') and a MF ('blazephotonics SC-5.0-1040'). The seed fibre-laser employs an all-isotropic fibre-integrated loop, passive-modelocking configuration with a central wavelength at $\sim 1060nm$. The pulse repetition rate is 40MHz, the maximum average output power is about 9W, and the pulse duration is ca. 3.5ps. The laser-output spectrum is not well defined, and is dependent on power, e.g., $\Delta\lambda = 10nm$ at 2W, 35nm at 5W, and 70nm at 9W.

The output is directed through an isolator and focussed by a 4.5mm focal length aspheric lens into a $\sim 20m$ length of the MF with a ZDW at 1040nm. A half-wave plate was placed immediately before the focussing optic to rotate the input polarization so as to match the (low) birefringence of the fibre. The resulting continuum output from the fibre was collimated using a x40 microscope objective. A set-up of the TCS is analogous to one shown in Fig. 16.

The spectrum of the continuum extends down to 530nm on the short wavelength side and is shown in Fig. 37. It is spectrally selected by placing an interference filter with a central transmission wavelength at 550nm and a passband of $\sim 50nm$ ('comar 550 IU

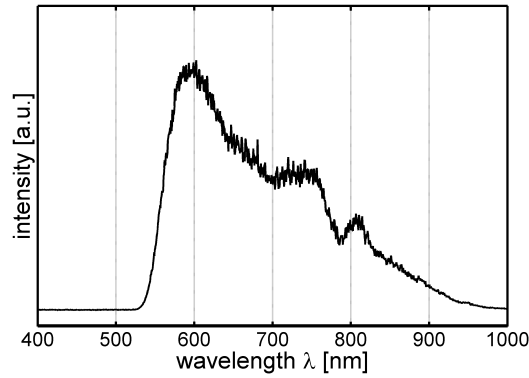


Figure 37: Short wavelength side of the continuum obtained with MF 'blazephotonics SC-5.0-1040' and the Yb fibre-laser. The incident average power was about $4W$ at $40MHz$, the low power transmission could be as high as 45%.

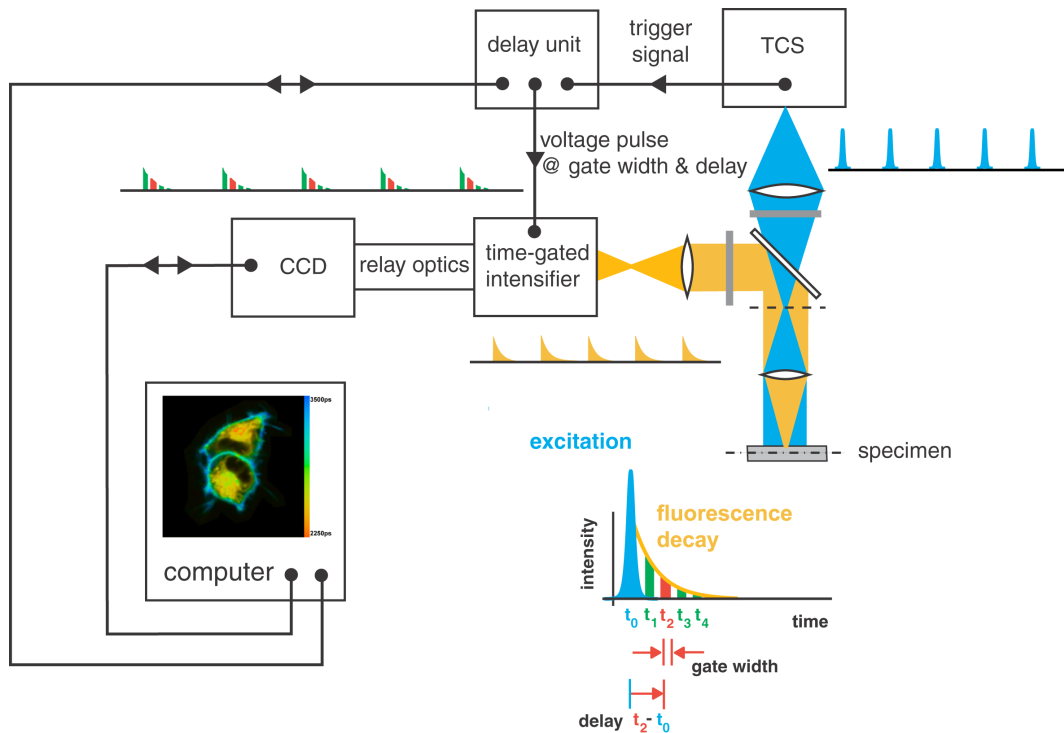


Figure 38: Schematic of the set-up for time-gated fluorescence lifetime measurements using a conventional wide-field fluorescence microscope.

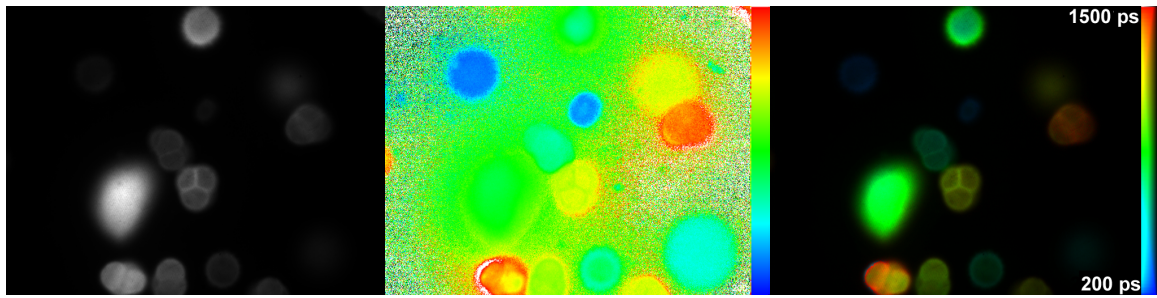
25 T-EJC') into the beam. The spectral power of this region was about $0.5mW/nm$.

The collimated light is steered by dielectric mirrors and a periscope into the microscope. Additionally, a rotating diffuser wheel is placed before the microscope input that causes the laser speckle at the sample to be time-averaged so as to give a spatially uniform illumination. The light deviated by the diffuser is gathered by a collector lens. A focussing lens in the microscope assures good illumination onto the specimen plane. Fig. 38 shows a schematic of the wide-field FLIM set-up.

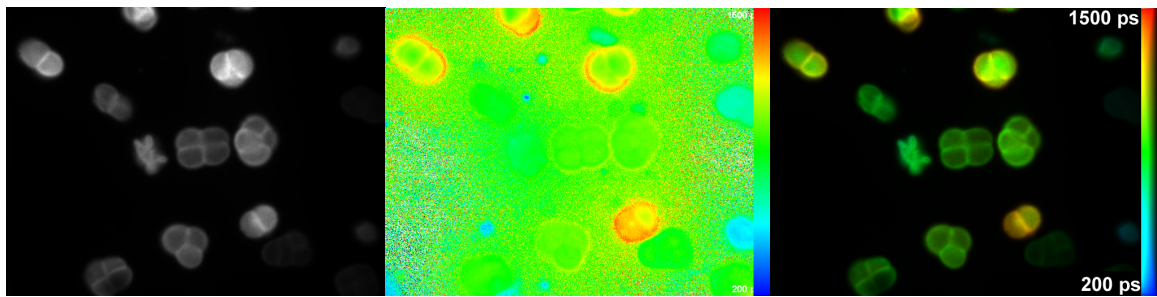
6.4.2 Application

Images taken with the (conventional) wide-field FLIM system are shown below. It is worth mentioning that the fluorescence lifetime maps exhibit a strong contrast. For instance, the first two rows of Fig. 39 show FLIM images of a test sample containing pollengrains. Here, the same fluorophore (Cy 3) exhibits different lifetimes in different environments. For the unmerged lifetime maps, the whitish areas interspersed by spots of apparent lifetimes can be explained with a lack of photons for these image pixels, and as a consequence, fitting becomes a problem or questionable. However, the intensity image is a photon number distribution, which can be used so as to form a weighted functional FLIM map. An additional point to note is that the pulse repetition rate of 40MHz allows the fluorescence to decay almost completely between the excitation pulses.

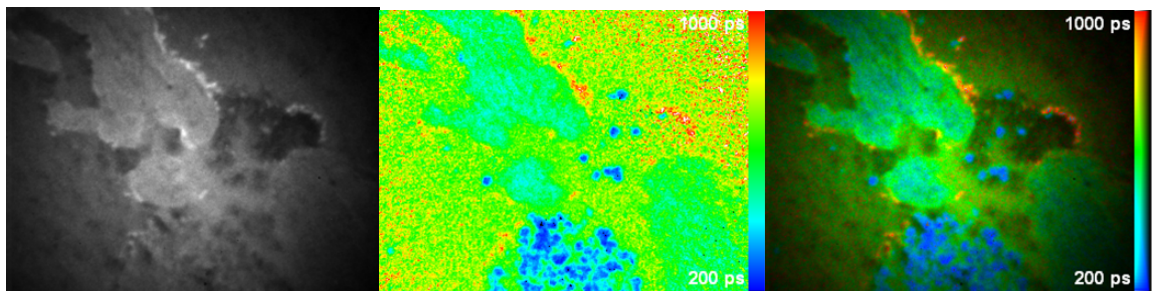
Although FLIM works well with the all-fibre continuum source and the power levels are significant higher compared to the spectra obtained by pumping the 'crystal fibre NL-2.0-740' with the Ti:sapphire laser, the spectral extension to short wavelengths is not satisfying. Particularly with regard to a flexible source for fluorescence imaging it is not very useful because the absorption spectra of the fluorophores need to be matched. Problems are also arising from the fibre-laser output characteristics: because the underlying principle of the mode-locking scheme is nonlinear-polarisation-rotation, the laser is sensitive to vibration, which translates to a rotation of the polarisation state of the output - this in turn causes significant power fluctuations due to polarisation optics (e.g., isolators).



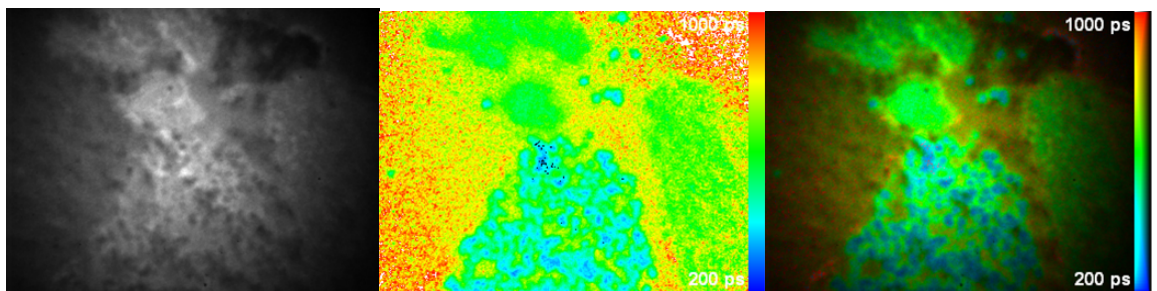
(a)



(b)



(c)



(d)

Figure 39: (a), (b): Pollengrains (stained with Cy 3), magnification x40, (the rows correspond to different fields of view) , (c), (d): Tissue stained with ttf- (different fields of view)

6.5 Compression

As stated in the section on wide-field FLIM (6.4), the combination of fibrelaser ('IPG YLP-8-1060-PS') and the MF ('blazephotonics SC-5.0-1040') produced a continuum which extends down to 530nm . This can be explained by the initial spectral location of the nonsoliton radiation due to phase-matching (at about 900nm for this fibre) and the following XPM-induced blue shift.

However, for fluorescence microscopy blue spectral components are vitally important. A closer examination of the laser output characteristics (Fig. 40: $\Delta\lambda = 10\text{ nm}$ ($\hat{=}$ $\Delta\omega_{\text{RMS}} = 14\text{ rad/ps}$ at $\lambda = 1.06\mu\text{m}$) and $\Delta T_{\text{FWHM}} = 3.1\text{ ps}$) reveals that compression is feasible, and thus, shorter pulses at higher peak-powers can be achieved (see uncertainty principle of section 2.1).

Supercontinuum generation with initial pulses on a picosecond time-scale is an intermediate regime located between the soliton fission mechanism and broadening of longer pulses due to stimulated Raman scattering and four-wave mixing [44]. Thus, pulse-compression could result in more impressive spectra because of pure soliton-fission as the underlying principle [135]. Within this regime, a favourable higher-order soliton number cannot be obtained via compression (because $N^2 \sim E\Delta T_0$, where the pulse-energy E is about the same during dispersion-induced compression), however, the shorter initial pulse-width translates to shorter pulse durations for the emerging fundamental solitons [49], and consequently, they are further Raman-shifted [52] for a given fibre length. This may have a direct impact on the XPM-induced blue shift.

In order to compress the picosecond pulses, the negative dispersion of a 4-prism sequence and retro-reflection was used (Fig. 41(a)). This configuration needs only about 25% prism-separation distance (L_2) [119] compared with a conventional pairs of prisms and retro-reflection [120–122]. The resultant compression vs. length of the negative dispersive medium (i.e., separation distance L_2) can be seen in Fig. 41(c). The experiment was simulated using a Fast-Fourier-transform method, thereby, an initial Gaussian pulse with SPM-induced Gaussian-shaped phase ($\phi_{\text{max}} = 11.3\pi$) was assumed (the corresponding spectrum is shown in Fig. 40(a)). To match the experiment with theory, the last free parameter, namely, the 2nd-order dispersive length L_D had to be set to 140m (i.e., scaling of the theoretical curve along the x-coordinate).

With the knowledge of L_D the dispersion of the prism-compressor at $\lambda = 1.06\mu\text{m}$ can be estimated as $|\beta^{(2)}| = T_0^2/L_D = (3.1\text{ps}/1.6651)^2/140\text{m} = 0.02476\text{ps}^2/\text{m}$.

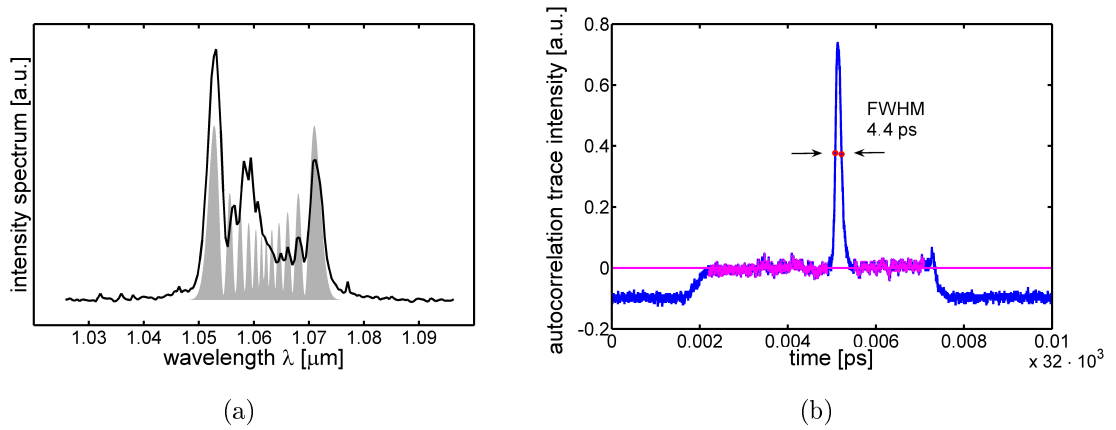


Figure 40: (a): Spectrum of the output of the IPG laser at a power of 2W behind an isolator (black line), and simulation of SPM-induced broadening of an initially unchirped Gaussian pulse by adjusting the maximal nonlinear phase-shift parameter, $\phi_{\max} = 11.3\pi$ [12] (grey area). (b): corresponding autocorrelation trace of the laser pulse, assuming a Gaussian pulse, a FWHM pulse duration of 3.1 ps is found (which is related to the RMS width as $\Delta T_{\text{FWHM}} = 2\sqrt{\ln 2}\sqrt{2} \Delta T_{\text{RMS}}$). The peak-to-background ratio of the trace is 8:1, which is in accord with theory

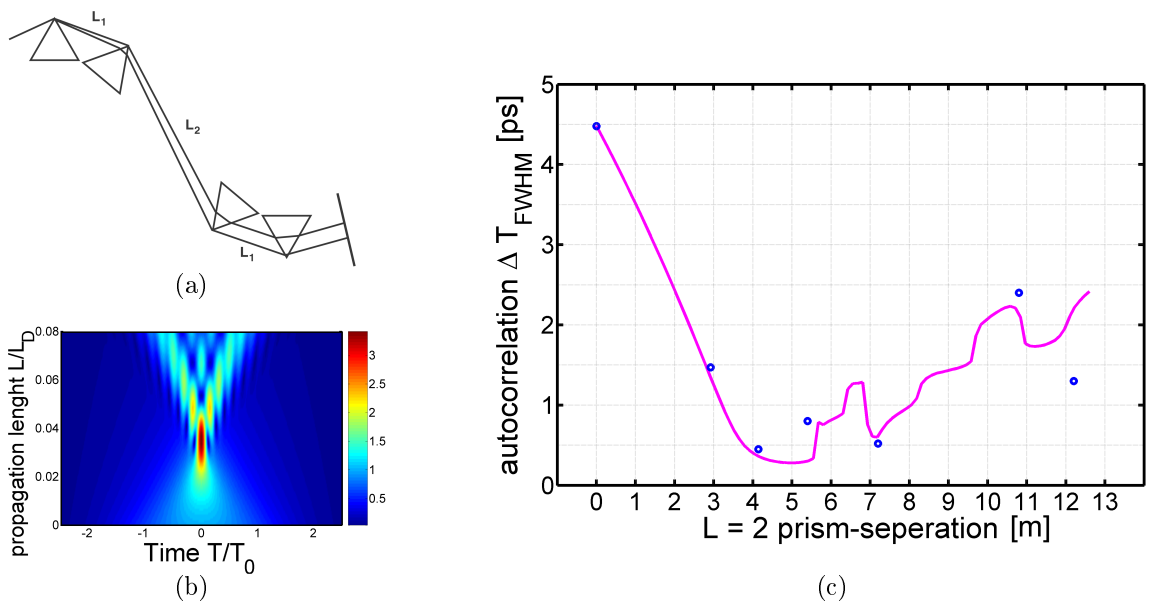


Figure 41: (a): Schematic of the 4-prism compressor (after Ref. [119]). (b): Simulation showing the temporal amplitude profile as a function of prism-separation (c): FWHM width of the autocorrelation trace vs. prism-separation, where the blue points are the experimental values obtained by autocorrelation, and the magenta coloured line is the behaviour expected by assuming an Gaussian-shaped pulse with initial (SPM-induced) Gaussian-shaped phase and propagation in a 2nd-order dispersive medium.

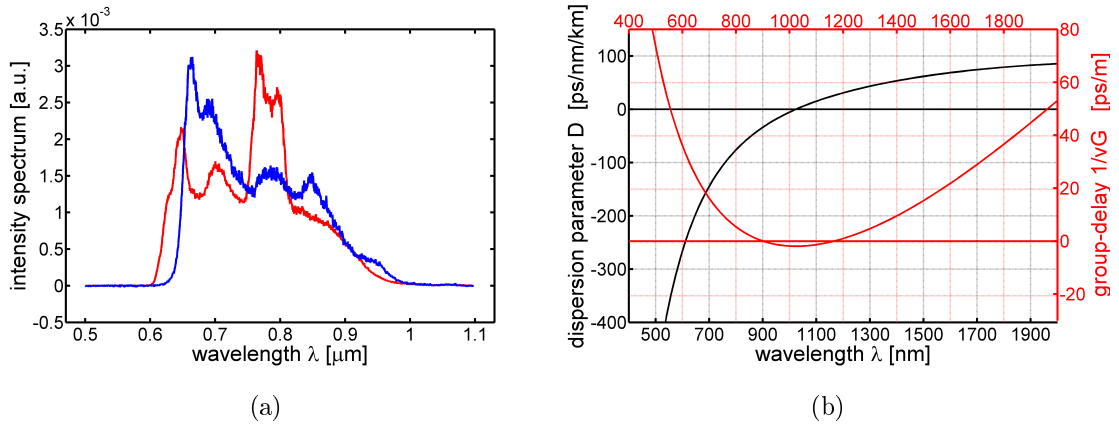


Figure 42: (a): compression-induced change on the short-wavelengths side of the SC spectrum. The red and blue curve correspond to the compressed and uncompressed pulse-trains, respectively. For both cases, the input-power was about 1.2 W and the output-power about 200 mW. (b): Dispersion parameter D vs. wavelength (black line) and group-delay $1/v_G$ with respect to the group-delay at $\lambda = 900\text{nm}$ (red line) vs. wavelength for the microstructured fibre 'blazephotonics SC-5.0-1040'

The ripples of the theoretical curve (Fig. 41(c)) can be explained with the evolution of the temporal amplitude profile (Fig.41(b)). An additional point to note is that the numerical method was checked by analytical expression for the evolution of a linearly chirped Gaussian pulse in presence of 2nd-order dispersion.

Unfortunately, the spectrum of the supercontinuum (Fig. 42(a)) did not broaden significantly for the shortest pulse duration (i.e., highest peak-power). The power behind the isolator is again 2W. In both cases the power launched into the MF is $P = 1.2W$ taking into account the efficiency of the compressor, which is about 0.6 due to the reflectivities of three silver-coated mirrors (used to fold the beam between the prisms) and the pick-out mirror. The low-power coupling efficiency into the microstructured fibre was about 30% for the un-compressed pulses and only about 10% for the compressed pulses. It is clear that a reduced nonlinearity infers from a decreased input-power, and as a consequence, this cancels the effect I wanted to demonstrate. Abberations introduced by the prisms are likely the reasons for this. By means of a spatial light modulator, astigmatism and defocussing could be identified. On the other hand, even if the perfect compressor was available, the group-delay curve for this MF indicates that XPM-induced blue-shifts are limited by the low group-delay dispersion at the region of the nonsoliton radiation (Fig. 42(b)). However, the generation of blue components requires XPM-induced blue-shifts of a few hundreds of nanometers.

7 Conclusion

7.1 Summary

A convenient, continuously tunable ultrafast source for fluorescence imaging applications has been demonstrated.

Since the used source is derived from a visible supercontinuum generated by launching femtosecond pulses into a microstructured fibre, this diploma thesis contains also studies concerning nonlinear fibre optics. The output of the continuum source has been characterised and the underlying mechanism has been studied. The latter is vitally important as it allows to answer fundamental questions arising in practise, for instance, the extension of the continuum to the blue. In particular, XPM-induced blue-shifts could be identified to play an important role with regard to the extension of the supercontinuum to the short-wavelength side. As dispersion is of paramount significance for a detailed characterisation, the dispersion of microstructured fibre has been measured. For this purpose, a spectral interferometric method employing a supercontinuum source has been realised. Building on the known dispersion, simulations have been carried out.

The convenient, continuously (electronically) tunable ultrafast source has been applied to confocal, Nipkow disk and wide-field fluorescence intensity and lifetime microscopy. In addition, it has been demonstrated in hyperspectral (i.e., temporally and spectrally resolved) imaging using line-scanning.

First results towards a wide-field optically sectioned FLIM system using a Nipkow disk were presented. Frequency-doubled Ti:sapphire could be used, but the enhanced tuning range and straightforward control of the excitation wavelength are advantages of the novel tunable continuum source. In addition, if based on a low cost and compact high average power fibre laser so as to pump the microstructured fibre this approach will be one of the most practical ones for fast fluorescence microscopy. Such systems will be particularly suitable for real-world applications. Consequently, another section deals with a future possibility of a low cost TCS based on compact, fibre amplifier technology. Because of the infancy of such systems (particularly, in terms of spectral coverage) there are still a few problems to be solved. However, it is an initial step towards a low-cost table-top fibre-laser system in biomedical optics.

The properties of the TCS can be also perfectly utilized by widespread confocal imaging. Generally speaking, the spatial coherence and the tunability across a broad

spectral region make the TCS the ideal source for fluorescence imaging systems involving apertures. FLIM can be applied to this imaging technique via time-correlated single photon counting. The application was particularly exciting. A membrane-staining dye – capable to differentiate liquid-ordered phases from -disordered phases coexisting in membranes – was studied in terms of fluorescence lifetime as well as spectral properties. In particular, this dye may be of broad significance in biophysical studies of lipid domains in model membranes and cells.

Another experiment dealt with spectrally and temporally resolved imaging based on the novel TCS. The broad spectral coverage of the continuum is particularly suitable for excitation dependent fluorescence emission studies allowing the acquisition of full fluorescence excitation-emission matrix data. This method allowed a detailed characterisation of multiple labelled tissue. It could be seen that spectrally as well as temporally resolved imaging reveals shift of fluorescence emission because of changes in fluorophore environment. Particularly, this type of spectroscopic imaging provides a method to remove ambiguity in fluorescence processes such as Förster resonance energy transfer (FRET). However, there are a few fundamental questions to answer when dealing with temporally and spectrally resolving imaging. For instance, how is lifetime correlated with spectral information and vice versa? Is there additional information provided for determination of FRET?

7.2 Outlook

Neither the examples chosen nor the experimental investigation made to date can be said to represent an exhaustive coverage of the possibilities for the application of continuum generation to the spectroscopic as well as imaging part of biomedical optics. In particular, this has two major reasons, namely, the wide scope of biomedical optics and the infancy of the TCS.

While the generation of radiation in the green and red spectral range by means of the continuum source is feasible, blue components (at a reasonable amount of spectral power on a linear intensity scale in a spatial single mode) are not so easy to realise. However, short wavelengths are important for the excitation of basic fluorophores

Is it possible to transcend this frontier? Nonsolitonic radiation experiences cross-phase modulation due to solitons which have been fallen behind in the supercontinuum generation process. This induces blue-shifts on the dispersive waves. Thus, an outset for consideration may be the location of the phase-matched dispersive waves. The

approximated solution for the location of the phase-matched components, Eq. (7), suggests that there exist two options.

Firstly, the fibre dispersion profile could be designed so as to provide huge shifts into the visible via high third-order dispersion. However, one has to admit that with the available types of optical glasses, the dispersion coefficients cannot be varied over several orders of magnitude compared to the ones from present microstructured fibres.

Secondly, the pump (i.e., soliton) frequency could be spectrally located as close as possible to the region of interest (i.e., spectral translation of the soliton centre, zero-dispersion point, and phase-matched nonsoliton radiation). However, this requires anomalous fibre dispersion towards the blue, too. To my knowledge, there are no microstructured fibres with ZDWs $< 550nm$ commercially available. If pumping of the MF in the visible is to be pursued, a pulsed source has to be chosen, too. A pump source could be a frequency-doubled mode-locked Erbium laser [123]. Such a high-peak power fibre source could supersede bulk solid-state lasers (Ti:sapphire) in a variety of applications, while benefiting from the all-fibre format and low cost [124, 125].

For instance, an all PM-fibre passively mode-locked oscillator using a semiconductor saturable absorber mirror could be the starting point for optimisation of supercontinuum generation. The right microstructured fibre which meets the frequency-fixed output of such sophisticated (frequency-doubled) oscillators may provide improved supercontinuum spectra. Because the whole system can potentially be fully fiber integrated, compact low-cost practical supercontinuum sources for use outside of the laboratory are feasible. Directly connected to a microscope frame, this system could provide an stable alignment-free FLIM light source.

A Yb fiber laser could also be frequency-doubled [126], but there are no MFs with a ZDW at the frequency-doubled output commercially available. Pump radiation in the range from 560 to 770nm could be also provided by a frequency-doubled Raman laser pumped with a Yb laser [127]. Another option is sum frequency generation using Er and Yb fibre amplifiers [128].

To produce blue components, another approach could be the generation of high spectral power nonsoliton radiation using a mode-locked Yb fibre-laser, followed by compression and frequency-doubling [129]. To realise an high average power fibre-source for this purpose, a parabolic amplifier as well as a CPA system based on reciprocal fibre-grating dispersive-delay line could be added to the fibre oscillator [125].

In addition, according to the calculated phasematching curves blue could be also gen-

erated by pumping far away from the zero-dispersion point in the visible (and there should not exist a second zero-dispersion point in the infrared). However, this approach requires high energy pulses so as to achieve huge spectral broadening, and thus, the generation of the phase-matched components in the initial stage of the continuum process. This is associated with the use of high energy pulses. In turn, this may be limited by the damage threshold of the fibre tip. In other words, a trade-off needs to be found concerning this issue.

In view of the limitation for a direct generation of blue spectral components using microstructured fibres, a focus of development could be also a high-power spectrally-limited continuum in the red/ infrared spectral region. Such a spectrum is very suitable for optically-sectioned multiphoton microscopy [5, 130]. In particular, fibre-technology can provide wavelengths above $1\mu m$, this is just beyond the range a Ti:sapphire laser can conveniently reach. This region is especially important for imaging of redder dyes and fluorescent proteins. A potential real world application is medical surgery, for this purpose, multiphoton endoscopes are being devised. There are multiphoton analogues to Nipkow disk scanning in which arrays of ultrashort pulse laser beams are focussed onto the sample and rapidly scanned to give a multiphoton excited fluorescence image that may be recorded using a wide-field detector [131]. This multifoci, multiphoton microscopy has also been applied to wide-field FLIM [132, 133].

How to obtain a suitable spectrum/ pulse for multi-photon microscopy? One approach could be a supercontinuum with a reasonable number of temporally-localised fundamental solitons covering the spectral regions of interest in the infrared. Frequency-resolved optical gating measurements may be useful for more detailed investigations [44, 135]. Instead of using supercontinuum generation, the interplay of SPM and normal dispersion could be used so as to produce a flat plateau on a linear intensity scale (bandwidth $\sim 200nm$) [12, 136]. Particularly, high-quality pulses can be expected by implementing positive dispersion fibres with gain.

A different approach regarding the generation of a limited high-power continuum is ultra-broad bandwidth parametric amplification around degeneracy [137]. This method also allows the production of few-cycle optical pulses, which in turn, can be used for high harmonic generation. This source for spatially coherent ultraviolet radiation could potentially have output powers in the mW range [138]. Consequently, high resolution spectroscopy and microscopy is possible [139].

The broad spectrum of the continuum source can be utilized in almost all spectroscopic

and imaging architectures based on fluorescence.

One of the most interesting property of the TCS is the capability to simultaneously (or sequentially) excite multiple fluorescent probes in living cells, which is an increasingly popular technique for monitoring the assembly of macromolecular complexes, protein-protein interactions, and the targeting of proteins to specific sites in the cell.

For example, Förster resonance energy transfer (FRET) could be ‘simply’ determined by choosing a set of excitation wavelengths which meet the spectral characteristics of the fluorophores. Förster distances are typically in the range of 15 – 60 Å, which is below the optical resolution of the light microscope [65, 140–147].

Another potential application is multi-colour fluorescence-in-situ-hybridisation (FISH) in combination with spectral precision distance microscopy (SPDM), which allows image analysis in the range of a ”resolution equivalent” of a few (<10) nanometers.

The TCS may be particular interesting for other spectral imaging modalities such as dual-excitation ratiometric imaging, which is a major approach to study life cell physiology.

A high-power supercontinuum source can be also used for techniques applied to analyze protein movement, e.g. fluorescence recovery after photobleaching (FRAP), photoactivation and photoconversion methods [148–150].

The TCS may be also useful for pump-probe fluorescence experiments [151–155]. The light source could be realised by an environmentally coupled dual-fibre laser [125].

Fluorescence cross-correlation spectroscopy using two or multiple excitation wavelengths may be another interesting application.

In addition to spectroscopic techniques, the TCS can be used in several other imaging methods, for instance, total internal reflection fluorescence (TIRF) microscopy [159], which produces fluorescence images with an extremely high signal-to-noise ratio, or a technique based on stimulated-emission depletion (STED), which allows to ‘break’ the diffraction barrier [160–162].

An all-fibre source could be also the step towards an all-fibre confocal microscope, which in turn could be used for endoscopic confocal imaging [156]. Hollow-core photonic crystal fibres exhibiting extremely low nonlinearity are also suitable for remote high energy ultrashort pulses delivery in two-photon microscopy, Ref. [157]. In addition, microstructured fibres are also more efficient fluorescence light collectors compared to conventional fibres in use [158].

References

- [1] K. Jacobson, "Fluorescence Microscopy", encyclopedia of life science (Nature Publishing Group, 2001).
- [2] V. J. Allen (editor), "Protein Localisation by Fluorescence Microscopy" (Oxford University Press, 2000).
- [3] E. Stelzer, "Confocal Microscopy", encyclopedia of life science (Nature Publishing Group, 2001).
- [4] J. B. Pawley (editor), "Handbook of Biological Confocal Microscopy", 2nd ed. (Plenum Press, 1995).
- [5] W. Denk, J. Strickler, W. Webb, "Two-photon laser scanning fluorescence microscopy", *Science* 248, 73-76 (1990).
- [6] J. Squier, M. Müller, "High resolution nonlinear microscopy: A review of sources and methods for achieving optimal imaging", *Rev. Sci. Instr.* 72, 2855-2867 (2001).
- [7] J. Hermann, U. Griebner, N. Zhavoronkov, A. Husakou, D. Nickel, J.C. Knight, W. J. Wadsworth, P. St. J. Russell, G. Korn, "Experimental Evidence for Supercontinuum Generation by Fission of Higher-Order Solitons in Photonic Fibers", *Phys. Rev. Lett.* 88, 1739011-1739014 (2002).
- [8] T. Schreiber, J. Limpert, H. Zellmer, A. Tünnermann, K. P. Hansen, "High average power supercontinuum generation in photonic crystal fibers", *Opt. Commun.* 228, 71-78 (2003).
- [9] A. Zheltikov, "Supercontinuum generation", *Appl. Phys. B* 77, 143-147 (2003).
- [10] C. Dunsby, P. M. P. Lanigan, J. McGinty, D. S. Elson, J. Requejo-Isidro, I. Munro, N. Galletly, F. McCann, B. Treanor, B. Önfelt, D. M. Davis, M. A. A. Neil, P. M. W. French, "An electronically tunable ultrafast laser source applied to fluorescence imaging and fluorescence lifetime imaging microscopy", *J. Phys. D-Appl. Phys.* 37, 3296-3303 (2004).
- [11] C. W. Wong, "Mathematische Physik", (Spektrum Akademischer Verlag, 1994).
- [12] G. P. Agrawal, "Nonlinear Fiber Optics", 3rd ed. (Academic Press, 2001).
- [13] P. N. Butcher, D. Cotter, "The Elements of Nonlinear Optics" (Cambridge University Press, 1990).
- [14] R. W. Boyd, "Nonlinear Optics", 2nd ed. (Academic Press, 2003).
- [15] J. D. Jackson, "Classical Electrodynamics", 3rd ed. (Wiley, 1999).
- [16] A. W. Snyder, J. D. Love, "Optical Waveguide Theory", 1st ed. (Chapman & Hall, 1983).
- [17] F. Lederer, *Vorlesung Theoretische Optik*, Friedrich-Schiller-Universität Jena (2003).
- [18] S. G. Johnson, J. D. Joannopoulos, "Block-iterative frequency-domain methods for Maxwell's equations in a planewave basis", *Opt. Express* 8, 173-190 (2001).
- [19] T. P. White, B. T. Kuhlmey, R. C. McPhedran, D. Maystre, G. Renversez, C. Martijn de Sterke, L. C. Botten, "Multipole method for microstructured optical fibers. I. Formulation", *J. Opt. Soc. Am. B* 19, 2322-2330 (2002).
- [20] Boris T. Kuhlmey, Thomas P. White, Gilles Renversez, Daniel Maystre, Lindsay C. Botten, C. Martijn de Sterke, Ross C. McPhedran, "Multipole method for microstructured optical fibers. II. Implementation and results", *J. Opt. Soc. Am. B* 19, 2331-2340 (2002).

- [21] M. J. Gander, R. McBride, J. D. C. Jones, D. Mogilevtsev, T. A. Birks, J. C. Knight, P. St. J. Russell, "Experimental measurement of group velocity dispersion in photonic crystal fibre", *Electron. Lett.* **35**, 63-64 (1999).
- [22] T. Fuji, M. Arakawa, T. Hattori, H. Nakatsukaa, "A white-light Michelson interferometer in the visible and near infrared regions", *Rev. Sci. Instrum.* **69**, 2854-2858 (1998).
- [23] S. Diddams, J.C. Diels, "Dispersion measurements with white-light interferometry", *J. Opt. Soc. Am. B* **13**, 1120-1129 (1996).
- [24] M. Tateda, N. Shibata, S. Seikai, "Interferometric Method for Chromatic Dispersion Measurement in a Single-Mode Optical Fiber", *IEEE J. Quantum Electron.* **17**, 404-407 (1981).
- [25] D. Ouzounov, D. Homoelle, W. Zipfel, W. Webb, A. Gaeta, J. West, J. Fajardo, K. Koch, "Dispersion measurement of microstructured fibers using femtosecond pulses", *Opt. Commun.* **192**, 219-223 (2001).
- [26] G. Genty, H. Ludvigsen, M. Kaivola, K.P. Hansen, "Measurement of anomalous dispersion in microstructured fibers using spectral modulation", *Opt. Express* **12**, 929-934, (2004).
- [27] Q. Ye, C. Xu, X. Liu, W. H. Knox, M. F. Yan, R. S. Windeler, B. Eggleton, "Dispersion measurement of tapered air-silica microstructure fiber by white-light interferometry", *Appl. Opt.* **41**, 4467-4470 (2002).
- [28] C. K. Nielsen, T. V. Andersen, "Easy implementable setup for measurement of the dispersion of a PBG fiber", private communication, research report at the University of Aarhus.
- [29] L. Lepetit, G. Cheriaux, M. Joffre, "Linear techniques of phase measurement by femtosecond spectral interferometry for applications in spectroscopy", *J. Opt. Soc. Am. B*, 2467-2474 (1995).
- [30] A. Hasegawa, F. D. Trappert, "Transmission of stationary nonlinear optical pulses in dispersive dielectric optical fibres", *Appl. Phys. Lett.* **23**, 142-144 (1973).
- [31] L. F. Mollenauer, R. H. Stolen, J. P. Gordon, "Experimental observation of picosecond pulse narrowing and solitons in optical fibers", *Phys. Rev. Lett.* **45**, 1095-1098 (1980).
- [32] P. M. W. French, "The generation of ultrashort laser pulses", *Rep. Prog. Phys.* **58** 169-267 (1995).
- [33] Y. S. Kivshar, G. Agrawal, "Optical Solitons: From Fibers to Photonic Crystals" (Academic Press, 2003).
- [34] W. H. Reeves, D. V. Skryabin, F. Biancalana, J. C. Knight, P. St. J. Russell, F. G. Omenetto, A. Efimov, A. J. Taylor, "Transformation and control of ultra-short pulses in dispersion-engineered photonic crystal fibres", *Nature* **424**, 511-515 (2003).
- [35] J. K. Ranka, R. S. Windeler, A. J. Stentz, "Visible continuum generation in airsilica microstructure optical fibers with anomalous dispersion at 800 nm", *Opt. Lett.* **25**, 25-27 (2000).
- [36] P. Russell, "Photonic Crystal Fibers", *Science* **299**, 358-362 (2003).
- [37] W.H. Reeves, J.C. Knight, P.St.J. Russell, "Demonstration of ultra-flattened dispersion in photonic crystal fibers", *Opt. Express* **10**, 609-613 (2002).
- [38] J. C. Knight, T. A. Birks, P. St. J. Russell, D. M. Atkin, "All-silica single-mode optical fiber with photonic crystal cladding", *Opt. Lett.* **21**, 1547-1549 (1996).
- [39] N. A. Mortensen, J. R. Folkenberg, M. D. Nielsen, K. P. Hansen, "Modal cutoff and the V parameter in photonic crystal fibers", *Opt. Lett.* **28**, 1879-1881 (2003).

- [40] N. A. Mortensen, M. D. Nielsen, J. R. Folkenberg, A. Petersson, H. R. Simonsen, "Improved large-mode-area endlessly single-mode photonic crystal fibers", *Opt. Lett.* 28, Opt. Lett. 393-395 (2003).
- [41] T. A. Birks, W. J. Wadsworth, P. St. J. Russell, "Endlessly single-mode photonic crystal fiber", *Opt. Lett.* 25, 1415 (2000).
- [42] V. A. Markel, T. F. George (editors), "Optics of Nanostructured Materials" (John Wiley & Sons, 2001).
- [43] A. V. Husakou, J. Hermann, "Supercontinuum Generation of Higher-order Solitons by Fission in Photonic Crystal Fibers", *Phys. Rev. Lett.* 87, 2039011-2039014 (2001).
- [44] S. Coen, A. H. L. Chau, R. Leonhardt, J. D. Harvey, J. C. Knight, W. J. Wadsworth, P. St. J. Russell, "Supercontinuum generation by stimulated Raman scattering and parametric four-wave mixing in photonic crystal fibers", *J. Opt. Soc. Am. B* 19, 753-764 (2002).
- [45] A. Ortigosa-Blanch, J. C. Knight, P. St. J. Russell, "Pulse-breaking and supercontinuum generation with 200-fs pump pulses in photonic crystal fibers", *J. Opt. Soc. Am. B* 19, 2567-2572 (2002).
- [46] A. L. Gaeta, "Nonlinear propagation and continuum generation in microstructured optical fibers", *Opt. Lett.* 27, 924-926 (2002).
- [47] I. Cristiani, R. Tediosi, L. Tartara, V. Degiorgio, "Dispersive wave generation by solitons in microstructured optical fibers", *Opt. Expr.* 12, 124-135 (2004).
- [48] N. Akhmediev, M. Karlsson, "Cherenkov radiation emitted by solitons in optical fibers", *Phys. Rev. A* 51, 2602-2607 (1995).
- [49] G. Genty, M. Lehtonen, H. Ludvigsen, J. Broeng, M. Kaivola, "Spectral broadening of femtosecond pulses into continuum radiation in microstructured fibers", *Opt. Expr.* 10, 1083-1098 (2002).
- [50] Y. Kodama, A. Hasegawa, "Nonlinear Pulse Propagation in a Monomode Dielectric Guide", *IEEE J. Quantum Electron.* 23, 510-524 (1987).
- [51] F. M. Mitschke, L. F. Mollenauer, "Discovery of the soliton self-frequency shift", *Opt. Lett.* 11, 659-661 (1986).
- [52] J. P. Gordon, "Theory of the soliton self-frequency shift", *Opt. Lett.* 11, 662-664 (1986).
- [53] D. V. Skryabin, F. Luan, J. C. Knight, P. St. J. Russell, "Soliton Self-Frequency Shift Cancellation in Photonic Crystal Fibers", *Science* 301, 1705-1708 (2003).
- [54] G. Genty, M. Lehtonen, H. Ludvigsen, "Enhanced bandwidth of supercontinuum generated microstructured fibers", *Opt. Expr.* 12, 3471-3480 (2004).
- [55] G. Genty, M. Lehtonen, H. Ludvigsen, "Effect of cross-phase modulation on supercontinuum generated in microstructured fibers with sub-30 fs pulses", *Opt. Expr.* 12, 4614-4624 (2004).
- [56] G. Genty, M. Lehtonen, H. Ludvigsen, "Route to broadband blue-light generation in microstructured fibers", *Opt. Lett.* 30, 756-758 (2005).
- [57] A. V. Husakou, J. Hermann, "Supercontinuum generation in photonic crystal fibers made from highly nonlinear glasses", *Appl. Phys. B* 77, 227-234 (2003).
- [58] L. Tartara, I. Christiani, V. Degiorgio, "Blue light and infrared continuum generation by soliton fission in a microstructured fiber", *Appl. Phys. B* 77, 307-311 (2003).

- [59] J. M. Dudley, X. Gu, L. Xu, M. Kimmel, E. Zeek, P. O'Shea, R. Trebino, S. Coen, R. S. Windeler, "Cross-correlation frequency resolved optical gating analysis of broadband continuum generation in photonic crystal fiber: simulations and experiments", *Opt. Expr.* 10, 1215-1221 (2002).
- [60] M. Börner, R. Müller, R. Schiek, G. Trommer, "Elemente der integrierten Optik" (B. G. Teubner, 1990).
- [61] P. M. W. French, Optics and Photonics MSc Biomedical Optics Course, Imperial College London (2005).
- [62] D. Elson, J. Requejo-Isidro, I. Munro, F. Reavell, J. Siegel, K. Suhling, P. Tadrous, R. Benninger, P. Lanigan, J. McGinty, C. Talbot, B. Treanor, S. Webb, A. Sandison, A. Wallace, D. Davis, J. Lever, M. Neil, D. Phillips, G. Stamp, and P. French, "Time-domain fluorescence lifetime imaging applied to biological tissue", *Photochem. Photobiol. Sci.* 3, 795 (2004).
- [63] P. Bastiaens and A. Squire, "Fluorescence lifetime imaging microscopy: spatial resolution of biochemical processes in the cell", *Trends in Cell Biology* 9, 48-51 (1999).
- [64] R. Cubeddu, D. Comelli, C. D'Andrea, P. Taroni, and G. Valentini, "Time-resolved fluorescence imaging in biology and medicine", *J. Phys. D: Appl. Phys.* 35, R61-R76, (2002).
- [65] F. Wouters, P. Verveer, and P. Bastiaens, "Imaging biochemistry inside cells", *Trends in Cell Biology* 11, 203-211 (2001).
- [66] P. Tadrous, "Methods for imaging the structure and function of living tissues and cells: 2. Fluorescence lifetime imaging", *J. Pathol.* 191, 229-234 (2000).
- [67] A. Rück, F. Dolp, C. Hülshoff, C. Hauser, C. Scalfi-Happ, "Fluorescence lifetime imaging in PDT. An overview", *Medical Laser Application* 20, 125129 (2005).
- [68] J. R. Lakowicz, "Principles of Fluorescence Spectroscopy" (Kluwer Academic/Plenum Publishers, 1999).
- [69] M. W. Davidson, M. Abramowitz, "Optical Microscopy", www.olympus.com .
- [70] G. McConnell, "Confocal laser scanning fluorescence microscopy with a visible continuum source", *Optics Express* 12, 2844-2850 (2004).
- [71] K. Shi, P. Li, S. Yin, Z. Liu, "Chromatic confocal microscopy using supercontinuum light", *Optics Express* 12, 2096-2101 (2004).
- [72] David Grant's MSc thesis, Imperial College London (2004).
- [73] D. S. Elson, I. Munro, J. Requejo-Isidro, J. McGinty, C. Dunsby, N. Galletly, G. W. Stamp, M. A. A. Neil, M. J. Lever, P. A. Kellett, A. Dymoke-Bradshaw, J. Hares, P. M. W. French, "Real-time time-domain fluorescence lifetime imaging including single-shot acquisition with a segmented optical image intensifier", *New Journal of Physics* 6, art. no. 180 (2004).
- [74] J. Requejo-Isidro, J. McGinty, I. Munro, D. Elson, N. Galletly, M. Lever, M. Neil, G. Stamp, P. French, P. Kellett, J. Hares, A. Dymoke-Bradshaw, "High-speed wide-field time-gated endoscopic fluorescence-lifetime imaging", *Opt. Lett.* 29, 2249-2251 (2004).
- [75] A. V. Agronskaia, L. Tertoolen, H. C. Gerritsen, "High frame fluorescence lifetime imaging", *J. Phys. D-Appl. Phys.* 36, 1655-1662 (2003).
- [76] M. Petran, M. Hadravsky, M. D. Egger, R. Galambos, "Tandem scanning reflected light microscope", *J. Opt. Soc. Am. A* 58, 661-664 (1968).

- [77] T. Tanaami, S. Otsuki, N. Tomosada, Y. Kosugi, M. Shimizu, H. Ishida, "High-speed 1-frame/ms scanning confocal microscope with a microlens and Nipkow disks", *Appl. Opt.* 41, 4704-4708 (2002).
- [78] S.-I. Kawamura, H. Negishi, S. Otsuki, N. Tomosada, "confocal laser microscope scanner and CCD camera", Yokogawa technical report English edition, No. 33 (2002).
- [79] R. Heintzmann's talk at B. Amos' workshop on optical techniques for cell physiology and developmental biology, Plymouth (2005).
- [80] S. Schwartz, *LaserFocusWorld* May 2005, "Spectral imaging evolves to meet biomedical needs", <http://lfw.pennnet.com/> (2005).
- [81] M. A. A Neil, R. Juskaitis, T. Wilson, "Method of obtaining optical sectioning by using structured light in a conventional microscope", *Opt. Lett.* 22, 1905-1907 (1997).
- [82] J. Siegel, D. S. Elson, S. E. D. Webb, D. Parsons-Karavassilis, S. Leveque-Fort, M. J. Cole, M. J. Lever, P. M. W. French, M. A. A Neil, R. Juskaitis, L. O. Sucharov, T. Wilson, "Whole-field five-dimensional fluorescence microscopy combining lifetime and spectral resolution with optical sectioning", *Opt. Lett.* 26, 1338-1340 (2001).
- [83] S. E. D. Webb, Y. Gu, S. Leveque-Fort, J. Siegel, M. J. Cole, K. Dowling, R. Jones, P. M. W. French, "A wide-field time-domain fluorescence lifetime imaging microscope with optical sectioning", *Rev. Sci. Instr.* 73, 1898-1907 (2002).
- [84] Stephen Webb's PhD thesis, "Development and Application of Widefield Fluorescence Lifetime Imaging", Imperial College London (2003).
- [85] A. A. Istratova, O. F. Vyvenko, "Exponential analysis in physical phenomena", *Rev. Sci. Instr.* 70, 1233-1257 (1999).
- [86] J. Siegel, D. S. Elson, S. E. D. Webb, K. C. Benny Lee, A. Vlandas, G. L. Gambaruto, S. Leveque-Fort, M. J. Lever, P. J. Tadrous, G. W. H. Stamp, A. L. Wallace, A. Sandison, T. F. Watson, F. Alvarez, P. M. W. French, "Studying biological tissue with fluorescence lifetime imaging: microscopy, endoscopy, and complex decay profiles", *Appl. Opt.* 42, 2995-3004 (2003).
- [87] R. Ballew, J. Demas, "An Error Analysis of the Rapid Lifetime Determination Method for the Evaluation of Single Exponential Decays", *Anal. Chem.* 61, 30-33 (1989).
- [88] R. Ballew, J. Demas, "Error analysis of the rapid lifetime determination method for single exponential decays with non-zero baseline", *Analytica Chimica Acta* 245, 121-127 (1991).
- [89] C. Moore, Sing Po Chan, J. Demas, B. DeGraff, "Comparison of Methods for Rapid Evaluation of Lifetimes of Exponential Decays", *Appl. Spectrosc.* 58, 603-607 (2004).
- [90] Becker&Hickl GmbH, "Detectors for High-Speed Photon Counting", www.becker-hickl.com .
- [91] Becker&Hickl GmbH, "Lifetime Imaging Techniques for Optical Microscopy", www.becker-hickl.com .
- [92] Becker&Hickl GmbH, "What is Time Correlated Single Photon Counting?", www.becker-hickl.com .
- [93] Becker&Hickl GmbH, "Time Correlated Single Photon Counting Systems", www.becker-hickl.com .

- [94] W. Becker, A. Bergmann, M.A. Hink, K. König, K. Benndorf, C. Biskup, "Fluorescence Lifetime Imaging by Time-Correlated Single-Photon Counting", *Microscopy Research and Technique* 63, 5866 (2004).
- [95] W. Koechner, "Solid-State Laser Engineering", 5th ed. (Springer, 1999).
- [96] V. I. Kruglov, A. C. Peacock, J. D. Harvey, "Self-similar propagation of parabolic pulses in normal-dispersion fiber amplifiers", *J. Opt. Soc. Am. B* 19, 461-469 (2002).
- [97] M. E. Fermann, V. I. Kruglov, B. C. Thomsen, J. M. Dudley, J. D. Harvey, "Self-Similar Propagation and Amplification of Parabolic Pulses in Optical Fibers", *Phys. Rev. Lett.* 84, 6010-6013 (2000).
- [98] K. Tamura, M. Nakazawa, "Pulse compression by nonlinear pulse evolution with reduced optical wave breaking in erbium-doped fiber amplifiers", *Opt. Lett.* 21, 68-70 (1996).
- [99] D. Anderson, M. Desaix, M. Karlsson, M. Lisak, M. L. Quiroga-Teixeiro, "Wave-breaking-free pulses in nonlinear-optical fibers", *J. Opt. Soc. Am. B* 10, 1185-1190 (1993).
- [100] J. Limpert's Dissertation, "High power ultrafast fiber laser systems", Friedrich-Schiller-Universität Jena (2003).
- [101] T. Clausnitzer, J. Limpert, K. Zöllner, H. Zellmer, H.-J. Fuchs, E.-B. Kley, A. Tünnermann, M. Jupé, D. Ristau, "Highly Efficient Transmission Gratings in Fused Silica for Chirped-Pulse Amplification Systems", *Appl. Opt.* 42, 6934-6938 (2003).
- [102] K. Saitoh, M. Koshiba, "Empirical relations for simple design of photonic crystal fibers", *Opt. Express* 13, 267-274 (2005).
- [103] M. Koshiba and K. Saitoh, "Applicability of classical optical fiber theories to holey fibers", *Opt. Lett.* 29, 1739-1741 (2004).
- [104] J. Riishede, N. A. Mortensen, J. Lægsgaard, "A 'poor mans approach' to modelling microstructured optical fibres", *J. Opt. A: Pure Appl. Opt.* 5, 534538 (2003).
- [105] datasheet titled "Nonlinear Photonic Crystal Fiber - NL-2.0-740", www.crystal-fibre.com .
- [106] datasheet titled "Nonlinear Photonic Crystal Fibers for 800nm Pumping", www.crystal-fibre.com .
- [107] K. P. Hansen, R. E. Kristiansen, application note "Supercontinuum Generation in Photonic Crystal Fibers", www.crystal-fibre.com .
- [108] G. P. Agrawal, P. L. Baldeck, R. R. Alfano, "Temporal and spectral effects of cross-phase modulation on copropagating ultrashort pulses in optical fibers", *Phys. Rev. A* 40, 5063-5071 (1989).
- [109] N. R. Newbury, B. R. Washburn, K. L. Corwin, R. S. Windeler , "Noise amplification during supercontinuum generation in microstructure fiber", *Opt. Lett.* 28, 944-946 (2003).
- [110] note "Compact ultra-bright supercontinuum light source", www.crystal-fibre.com .
- [111] instruction manual "Confocal Scanner Unit Model CSU10", 1st ed., Yokogawa Electric Corporation (1999).
- [112] Kentech Instruments Ltd., "Operations Manual for High Rate Imager" (1998).
- [113] Kentech Instruments Ltd., "Instruction Manual for Precision Programmable Delay Generator" (1997).
- [114] W. Becker, A. Bergmann, C. Biskup, L. Kelbauskas, T. Zimmer, N. Klöcker, K. Benndorf, "High resolution TCSPC lifetime imaging", *Proc. SPIE* 4963 (2003).

- [115] M. Chalfie, Y Tu, G. Euskirchen, W. W. Ward, D. C. Prasher, *Science* 263, 802-805 (1994).
- [116] L. Jin, A. C. Millard, J. P. Wuskell, H. A. Clark, L. M. Loew, "Cholesterol Enriched Lipid Domains can be Visualized by di-4-ANEPPDHQ with Linear and Non-Linear Optics", *Biophysical Journal-Biophysical Letters*, May, L01-L03 (2005).
- [117] "Fluorescence - Part 1", *Imaging & microscopy* 7, 50-53 (GIT Verlag, 2005).
- [118] "Filters for Black & White Photomicrography", www.olympusmicro.com .
- [119] B. Proctor, F. Wise, "Quartz prism sequence for reduction of cubic phase in a mode-locked $Ti:Al_2O_3$ ", *Opt. Lett.* 17, 1295-1297 (1992).
- [120] R. L. Fork, O. E. Martinez, J. P. Gordon, "Negative dispersion using pairs of prisms", *Opt. Lett.* 9, 150-152 (1984).
- [121] O. E. Martinez, J. P. Gordon, R. J. Fork, "Negative group-velocity dispersion using refraction", *J. Opt. Soc. Am. A* 1, 1003-1006 (1984).
- [122] J. P. Gordon, R. L. Fork, "Optical resonator with negative dispersion", *Opt. Lett.* 9, 153-155 (1984).
- [123] C. J. S. Matos, R. E. Kennedy, S. V. Popov, J. R. Taylor, "20-kW peak power all-fiber 1.57- μ m source based on compression in air-core photonic bandgap fiber, its frequency doubling, and broadband generation from 430 to 1450 nm", *Opt. Lett.* 30, 436-438 (2005).
- [124] U. Keller, "Recent developments in compact ultrafast lasers", *Nature* 424, 831-838 (2003).
- [125] M. E. Fermann, A. Galvanauskas, G. Sucha, D. Harter, "Fiber-lasers for ultrafast optics", *Appl. Phys. B* 65, 259-275 (1997).
- [126] A. G. Getman, S. V. Popov, J. R. Taylor, "7 W average power high-beam-quality green generation in MgO-doped stoichiometric periodically poled lithium tantalate", *Appl. Phys. Lett.* 85, 3026-3028 (2004).
- [127] D. Georgiev, V. P. Gapontev, A. G. Dronov, M. Y. Vyatkin, A. B. Rulkov, S. V. Popov, J. R. Taylor, "Watts-level frequency doubling of a narrow line linearly polarised Raman fiber laser to 589nm", *Opt. Expr.* 13, 6772-6776 (2005).
- [128] P. A. Champert, S. V. Popov, A. V. Avdokhin, J. R. Taylor, "Sum frequency generation of synchronously-seeded high-power Yb and Er fiber amplifiers in periodically poled KTP", *Appl. Phys. Lett.* 81, 3732-3734 (2002).
- [129] www.toptica.com .
- [130] W. R. Zipfel, R. M. Williams, W. W. Webb, "Nonlinear magic: multiphoton microscopy in the bioscience", *Nature Biotech.* 21, 1369-1377 (2003).
- [131] J. Bewersdorf, R. Pick, S. W. Hell, "Multifocal multiphoton microscopy", *Opt. Lett.* 23, 655-657 (1998).
- [132] M. Straub, S. W. Hell, "Fluorescence lifetime three-dimensional microscopy with picosecond precision using a multifocal multiphoton microscope", *Appl. Phys. Lett.* 73, 1769-1771 (1998).
- [133] S. Leveque-Fort, M. P. Fontaine-Aupart, G. Roger and P. Georges, "Fluorescence-lifetime imaging with a multifocal two-photon microscope", *Opt. Lett.* 29, 2884-2886 (2004).
- [134] R. Trebino, K. W. DeLong, D. N. Fittinghoff, J. N. Sweetser, M. A. Krumbügel, B. A. Richman, D. J. Kane, "Measuring ultrashort laser pulses in the time-frequency domain using frequency-resolved optical gating", *Rev. Sci. Instr.* 68, 3277-3295 (1997).

- [135] J. M. Dudley, L. Provino, N. Grossard, H. Maillotte, R. S. Windeler, B. J. Eggleton, S. Coen, "Supercontinuum generation in airsilica microstructured fibers with nanosecond and femtosecond pulse pumping", *J. Opt. Soc. Am. B* 19, 765-771 (2002).
- [136] G. P. Agrawal, "Applications of Nonlinear Fiber Optics", (Academic Press, 2001).
- [137] J. Limpert, C. Aguerarary, S. Montant, I. Manek-Hönniger, S. Petit, D. Descamps, E. Cormier, F. Salin, "Ultra-broad bandwidth parametric amplification at degeneracy", *Opt. Expr.* 13, 7386-7392 (2005).
- [138] C. Gohle, T. Udem, M. Hermann, J. Rauschenberg, R. Holzwarth, H. A. Schuessler, F. Krausz, T. W. Hänsch, "A frequency comb in the extreme ultraviolet", *Nature* 436, 234-237 (2005).
- [139] M. Wieland, C. Spielmann, U. Kleinberg, T. Westerwalbesloh, U. Heinzmann, T. Wilhein, "Toward time-resolved soft X-ray microscopy using pulsed fs-high-harmonic radiation, *Ultra-microscopy* 102, 93-100 (2005).
- [140] P. I. H. Bastiaens, T. M. Jovin, "Microspectroscopic imaging tracks the intracellular processing of a signal transduction protein: Fluorescent-labeled protein kinase C β I", *Proc. Natl. Acad. Sci. USA* 93, 84078412, (1996).
- [141] B. J. Bacskai, J. Skoch, G. A. Hickey, R. Allen, B. T. Hyman, "Fluorescence resonance energy transfer determinations using multiphoton fluorescence lifetime imaging microscopy to characterize amyloid-beta plaques", *J. Biomed. Opt.* 8, 368375 (2003).
- [142] M. Elangovan, R. N. Day, A. Periasamy, "Blackwell Science Ltd Nanosecond fluorescence resonance energy transfer-fluorescence lifetime imaging microscopy to localize the protein interactions in a single living cell", *J. Microscopy* 205, 3-14 (2002).
- [143] A. G. Harpur, F. S. Wouters, P. I.H. Bastiaens, "Imaging FRET between spectrally similar GFP molecules in single cells", *Nature Biotech.* 19, 167-169 (2001).
- [144] Wolfgang Becker, Klaus Benndorf, Axel Bergmann, Christoph Biskup, Karsten König, Uday Tirupapur, Thomas Zimmer, "FRET Measurements by TCSPC Laser Scanning Microscopy", *European Conferences on Biomedical Optics, ECBO 2001 Munic* (2001).
- [145] C. Biskup, T. Zimmer, K. Benndorf, "FRET between cardiac Na⁺ subunits measured with a confocal microscope and a streak camera", *Nature Biotech.* 22, 220-224 (2004).
- [146] E. A. Jares-Erijman, T. M. Jovin, "FRET Imaging", *Nature Biotech.* 21, 1387-1395 (2003).
- [147] T. Zal, N. R. J. Gascoigne, "Photobleaching-Corrected FRET Efficiency Imaging of Live Cells", *Biophys. J.* 86, 39233939 (2004).
- [148] J. Lippincott-Schwartz, E. Snapp, A. Kenworthy, *Nat. Rev. Mol. Cell Bio.* 2, 444-456 (2001).
- [149] E. A. J. Reits, J. J. Neefjes, *Nat. Cell Bio.* 3, E145-E147 (2001).
- [150] A. Miyawaki, *Nature Biotech.* 22, 1374-1376 (2004).
- [151] F. E. Lytle, R. M. Parish, and W. T. Barnes, "An introduction to time-resolved pump/probe spectroscopy", *Appl. Spectrosc.* 39, 444451 (1985).
- [152] P. A. Elzinga, R. J. Kneisler, F. E. Lytle, G. B. King, N. M. Laurendeau, "Pump/probe method for fast analysis of visible spectral signatures utilizing asynchronous optical sampling", *Appl. Opt.* 26, 4303-4309 (1987).
- [153] C. Y. Dong, P. T. C. So, T. French, E. Gratton, "Fluorescence lifetime imaging by asynchronous pump-probe microscopy", *Biophys. J.* 69, 22342242 (1995).

- [154] C. Y. Dong, C. Buehler, P. T. C. So, T. French, E. Gratton, "Implementation of intensity-modulated laser diodes in time-resolved, pump-probe fluorescence microscopy", *Appl. Opt.* 40, 1109-1115 (2001).
- [155] C. Buehler, C. Y. Dong, P. T. C. So, T. French, E. Gratton, "Time-resolved polarization Imaging By Pump-Probe (Stimulated Emission) Fluorescence Microscopy", *Biophys. J.* 79, 536-549 (2000).
- [156] C. P. Lin, R. H. Webb, "Fiber-coupled multiplexed confocal microscope", *Opt. Lett.* 25, 954-956 (2000).
- [157] SP Tai, MC Chan, TH Tsai, SH Guol, LJ Chen, CK Sun, "Two-photon fluorescence microscope with a hollow-core photonic crystal fiber", *Opt. Expr.* 12, 6122-6128 (2004).
- [158] J. Ma, W. J. Bock, "Modeling of photonic crystal fiber with air holes sealed at the fiber end and its application to fluorescent light collection efficiency enhancement", *Opt. Expr.* 13, 2385-2393 (2005).
- [159] H. Schneckenburger, K. Stock, W. S. L. Strauss, J. Eickholz, R. Sailer, "Time-gated total internal reflection fluorescence spectroscopy (TG-TIRFS): application to the membrane marker laurdan", *Journal of Microscopy* 211, 3036 (2003).
- [160] S. W. Hell, J. Wichmann, "Breaking the diffraction resolution limit by stimulated emission: stimulated-emission-depletion fluorescence microscopy", *Opt. Lett.* 19, 780-782 (1994).
- [161] S. W. Hell, "Toward fluorescence nanoscopy", *Nat. Biotech.* 21, 1347-1355 (2003).
- [162] M. Dyba, S. Jakobs, S. W. Hell, "Immunofluorescence stimulated emission depletion microscopy", *Nat. Biotech.* 21, 1303-1304 (2003).
- [163] E. Hecht, "Optics", 2nd ed. (Addison-Wesley, 1987).
- [164] technical information of SCHOTT, "Optics for devices, TIE-29: Refractive Index and Dispersion", www.schott.com .
- [165] optical glass data sheets, version 04/10/2004, www.schott.com .
- [166] www.fastlite.com .

A Selection of Wavelengths from the Continuum Source

Fluorescence emission is usually recorded by choosing an appropriate excitation wavelength which is entirely situated in the absorption spectrum of the fluorophore, i.e., spectral overlap with the emission spectrum (which may not be spectrally distinct) should be avoided.

Monochromators are used to disperse polychromatic light into the various wavelengths. For instance, the spectral resolution of a prism-monochromator is given by $(\lambda/\delta\lambda) = b|dn/d\lambda|$, where b is the effective prism-basis length. Upon fanning-out, selection of a limited spectral region takes place. The performance specifications of a monochromator include the dispersion, the efficiency, the polarisation dependency, and the stray-light levels. Resolution is usually of secondary importance since typical features of fluorescence absorption spectrums are rarely less than $5nm$.

A.1 Prism-Monochromator

The collimated output light from the MF using an achromatic objective lens may be directed into a spectral discriminator. Fig. 43 shows a schematic of the experimental set-up used in the experiment. Following angular fanning-out at an equilateral prism (SF18) having three equal 60° angles, the achromatic lens ($f = 180mm$, 'Melles Griot 01LAO139'), situated one focal length from the apex of the prism, focusses the various spectral components onto a mirror. A triangular-shaped aperture, which is located directly in front of the mirror and mounted on a (motorized) translation stage, provides the spectral selection. Horizontal translation of this aperture adjusts the central wavelength, and vertical translation adjusts the spectral width. Upon retro-reflection through the lens-prism arrangement, the light is collimated and picked off by a knife-edge mirror. For this purpose, the lens is lowered with respect to the optical axis.

The combination of aperture, mirror and translation stage could be replaced by a spatial light modulator. In particular, this allows simultaneous fluorescence excitation with spectrally distinct sections of a continuum.

For a prism with an apex angle α , the angle of minimum deviation δ_{min} is of particular interest for practical reasons [163]. In this case, the ray traverses the prism symmetrically, a maximum clear aperture is achieved and reflective loss in the TM (p) polarisation is reduced, owing to the close proximity to Brewster's angle of the

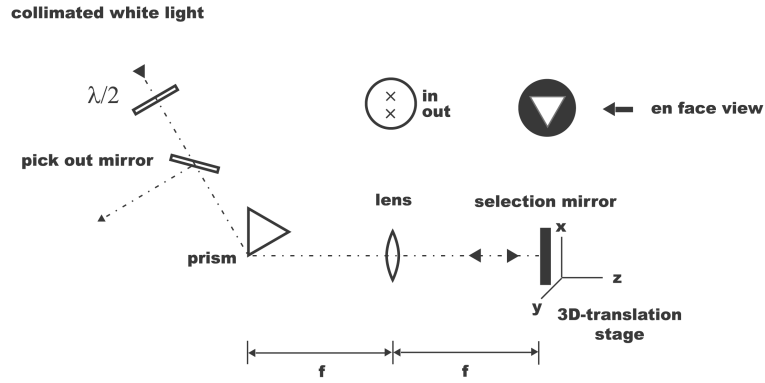


Figure 43: Monochromator

incident light. Using the Fresnel equations and the Sellmeier equation for the prism-glass [164,165], it can be shown that for an uncoated prism the transmission efficiency for the TE (s) and TM (p) polarisation states is about 40% and $> 95\%$ (at visible radiation), respectively. Thus, an anti-reflective coating (e.g., $1/4$ -wave layer of MgF_2) will enhance transmission significantly. In general, the use of a PM microstructured fibre for continuum generation could avoid problems which are attributed to polarisation dependency of monochromators.

An alternative to prism-monochromators could be acousto optical tunable filters [166].

A.2 Interference Filters

Interference filters are a simple means of spectral selection, too. They can conveniently be arranged in a wheel. Fig. 44 shows the spectral characteristics of the filters which were used in the experiments. These filters were also employed for calibration of the supercontinua and in the spectral noise measurements.

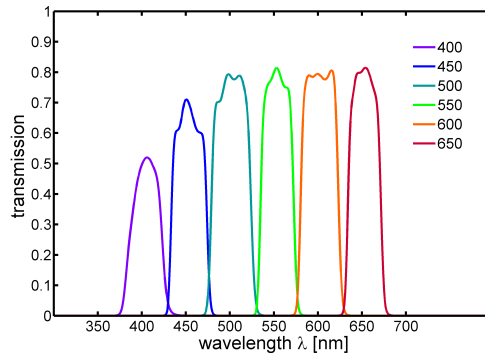


Figure 44: Transmission vs. wavelength for the set of bandpass interference filters ('Comar').

Erklärung:

Ich erkläre, dass ich die vorliegende Arbeit selbstständig verfasst und keine anderen als die angegebenen Quellen und Hilfsmittel benutzt habe.

Jena, der..... Damian N. Schimpf.....

Seitens des Verfassers bestehen keine Einwände, die vorliegende Diplomarbeit für die Nutzung in der Thüringer Universitäts- und Landesbibliothek zur Verfügung zu stellen.

Jena, der..... Damian N. Schimpf.....